

REPORT DOCUMENTATION PAGE

Public reporting burden for this collection of information is estimated to average 1 hour per response, including the time for reviewing instructions, searching existing data sources, gathering the data needed, and completing and reviewing this collection of information. Send comments regarding this burden estimate or any other aspect of this collection of information, including suggestions for reducing this burden, to Washington Headquarters Services, Directorate for Information Operations and Reports (0704-014302). Respondents should be aware that notwithstanding any other provision of law, no person shall be subject to any penalty for failing to comply with a collection of information if it does not have a valid OMB control number. PLEASE DO NOT RETURN YOUR FORM TO THE ABOVE ADDRESS.

AFRL-SR-BL-TR-02-

0054

1. REPORT DATE (DD-MM-YYYY) 12/21/01		2. REPORT TYPE Final Progress Report		4/1/99 - 11/30/01	
4. TITLE AND SUBTITLE Aeroelastic Leveraging and Control through Adaptive Structures				5a. CONTRACT NUMBER	
				5b. GRANT NUMBER F49620-99-1- 0253	
				5c. PROGRAM ELEMENT NUMBER	
6. AUTHOR(S) Robert L. Clark				5d. PROJECT NUMBER	
				5e. TASK NUMBER	
				5f. WORK UNIT NUMBER	
7. PERFORMING ORGANIZATION NAME(S) AND ADDRESS(ES) Duke University, Box 90300 Durham, NC 27708-0300				8. PERFORMING ORGANIZATION REPORT NUMBER	
9. SPONSORING / MONITORING AGENCY NAME(S) AND ADDRESS(ES) AFOSR/NA 801 N. Randolph Street Room 732 Arlington, VA 22203-1977				10. SPONSOR/MONITOR'S ACRONYM(S)	
				11. SPONSOR/MONITOR'S REPORT NUMBER(S)	
12. DISTRIBUTION / AVAILABILITY STATEMENT Approved for public release; distribution is unlimited					
13. SUPPLEMENTARY NOTES AIR FORCE OFFICE OF SCIENTIFIC RESEARCH (AFOSR) NOTICE OF TRANSMITTAL DTIC. THIS TECHNICAL REPORT HAS BEEN REVIEWED AND IS APPROVED FOR PUBLIC RELEASE LAW AFR 100-12. DISTRIBUTION IS UNLIMITED.					
14. ABSTRACT The primary objective of the proposed program is to develop and design a distributed actuation methodology for wing warping in UCAVs aimed at (1) control of higher-order flutter modes, (2) increased maneuverability, (3) reduced radar signature. Specific milestones achieved during the funded phase of the program include: <ul style="list-style-type: none"> ➤ Completed design and testing of high aspect ratio wing model in Duke University Wind Tunnel to correlate computer model used to design wing - LCO/Flutter. ➤ Completed design and bench testing of V-Stack actuator for integration into airfoil. ➤ Completed design specifications for a typical section wind tunnel model to evaluate performance of V-stack actuator with a single control surface. ➤ Performed initial design of continuously deformable control surface and evaluated performance for flutter suppression. ➤ Developed reduced-order models to evaluate enhanced roll performance of a warped, adaptive, aeroelastic wing. 					
15. SUBJECT TERMS					
16. SECURITY CLASSIFICATION OF:			17. LIMITATION OF ABSTRACT	18. NUMBER OF PAGES 138	19a. NAME OF RESPONSIBLE PERSON Dean T. Mook
a. REPORT unclassified	b. ABSTRACT unclassified	c. THIS PAGE unclassified			19b. TELEPHONE NUMBER (include area code) (703) 696-7259

JAN 15 2001

FINAL PROGRESS REPORT

Aeroelastic Leveraging and Control through Adaptive Structures

AFOSR Grant Number F49620-99-1-~~0~~0253

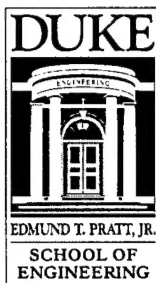
Robert L. Clark, PI

Duke University

Department of Mechanical Engineering and Materials Science

Box 90300

Durham, NC 27708-0300



20020221 074

Objective

■ The primary objective of the proposed program is to develop and design a distributed actuation methodology for wing warping in UCAVs aimed at (1) control of higher-order flutter modes, (2) increased maneuverability, (3) reduced radar signature.

Status of Effort

Specific milestones achieved during the funded phase of the program include:

- Completed design and testing of high aspect ratio wing model in Duke University Wind Tunnel to correlate computer model used to design wing – LCO/Flutter.
- Completed design and bench testing of V-Stack actuator for integration into airfoil.
- Completed design specifications for a typical section wind tunnel model to evaluate performance of V-stack actuator with a single control surface.
- Performed initial design of continuously deformable control surface and evaluated performance for flutter suppression.
- Developed reduced-order models to evaluate enhanced roll performance of a warped, adaptive, aeroelastic wing.

Accomplishments/New Findings

Experimental and Theoretical Investigation of Flutter and Limit Cycle Oscillations of (Very) High Aspect Ratio Wings [1-3]

Such wings are of great interest for certain classes of Uninhabited Air Vehicles (UAVs). They have unique aeroelastic characteristics and also pose a special challenge to active or adaptive control of their aeroelastic response and stability. An experimental and theoretical study of both flutter (the linear stability boundary) and limit cycle oscillations (LCO) was conducted to provide a verified baseline dynamic plant model that can be used as a testbed for active and adaptive control.

Among the major findings were the following. (1) For a sufficiently high aspect ratio wing a higher order bending mode may be most critical for flutter and LCO. This confirms what design engineers have observed regarding the flutter mode for operational UAVs (unpublished data) using linear aeroelastic theory. (2) Moreover our results show that nonlinear effects may be significant for determining both the onset of flutter and the LCO that may occur. Two nonlinear effects were modeled theoretically and experimentally, (a) the nonlinear coupling among structural bending in both the lift and drag directions and the torsional twist of the wing and (b) the aerodynamic stall of the wing at high angles of attack. It was shown that large disturbances may lead to flutter at flight velocities or dynamic pressures below those predicted by traditional linear flutter theory. (3) Good agreement between theory and wind tunnel experiments was shown for both flutter and LCO lending confidence to our mathematical modeling methods.

The results of this investigation provide a firm foundation for the modeling of high aspect ratio UAV plant dynamics for the conceptual design of advanced adaptive control systems.

Development of an Adaptive Aeroelastic Wing with Leading and Trailing Edge Control Surfaces [4-6]

In a series of three papers, this concept was (a) developed and mathematically modeled, then experimentally verified for both (b) steady state and (c) transient rolling motion of a wing. While the aeroelastic R&T community has known for several years that an adaptive combination of control surfaces can lead to improved rolling performance by taking advantage of the aeroelastic response of a wing, this investigation has led to new insights into the optimum strategy for doing so. In brief it has been shown that the leading and trailing edge controls should be used to counteract the loss of aerodynamic effectiveness (e.g. lift or roll rate) until the reversal dynamic pressure* is reached and then for higher dynamic pressures the controls should be reversed to create the maximum steady state aerodynamic performance. This theoretical result has been confirmed in wind tunnel tests and further mathematical modeling and wind tunnel investigations to assess transient performance has shown the concept to be viable for those conditions as well.

The results of this investigation provide the foundation for new design concepts for enhanced performance of combat aerospacecraft.

Development of Compact Solid-State Actuator [7]

Aeroelastic control of wings by means of a distributed, trailing-edge control surface is of interest with regards to maneuvers, gust alleviation, and flutter suppression. The use of high energy density, piezoelectric materials as motors provides an appealing solution to this problem. A comparative analysis of the state of the art actuators was conducted, and a new piezoelectric actuator was designed which meets the requirements for both stroke and force of trailing edge flap actuation. It is compact, simple, sturdy, and leverages stroke geometrically with minimum force penalties while displaying linearity over a wide range of stroke. The "V-Stack Piezoelectric Actuator," consists of a base, a lever, two piezoelectric stacks, and a pre-tensioning element. The work is performed alternately by the two stacks, placed on both sides of the lever. Pre-tensioning can be readily applied using a torque wrench, obviating the need for elastic elements and this is for the benefit of the stiffness of the actuator. The characteristics of the actuator are easily modified by changing the base or the stacks. A prototype was constructed and tested experimentally to validate the theoretical model, and the device is capable of generate 100 pounds of force at the tip with a bandwidth extending to approximately 500 Hz.

Personnel Supported

Robert L. Clark, (PI)

Earl H. Dowell (Co-PI)

Kenneth Hall (Co-PI)

Demian Tang (Research Scientist)

Mayur Patil (Research Scientist)

John Rule (Research Scientist)

Emil Ardilean (Graduate Student)

Publications

1. Tang, Deman, and E. Dowell, 2001. "Experimental and Theoretical Study on Flutter and Limit Cycle Oscillations of High-Aspect Ratio Wings," *AIAA Journal*, **39**(8), 1430-1441.
2. Rule, J., D. E. Cox, and R. L. Clark, 2000. "Aerodynamic Model Reduction Through Balanced Realization," accepted for publication in the *AIAA Journal*.
3. Rule, J. A., R. E. Richard, and R. L. Clark, 2001. "Design of an Aeroelastic Delta Wing Model for Active Flutter Control," accepted to *AIAA Journal of Guidance, Control, and Dynamics*.
4. Dowell, E. H., D. B. Bliss, and R. L. Clark, 2001. "An Adaptive Aeroelastic Wing with Leading and Trailing Edge Control Surfaces," submitted to *AIAA Journal*.
5. Tang, Deman, A. Li, and E. H. Dowell, 2001. "Experimental and Theoretical Study on Rolling Effectiveness of Multiple Control Surfaces," submitted to *AIAA Journal*.
6. Tang, D. A. Li, and E. H. Dowell, 2001. "Transient Response Study of Rolling Effectiveness of Multiple Control Surfaces," to be submitted to *AIAA Journal*.
7. Ardelean, A., R. L. Clark, 2001. "V-Stack Piezoelectric Actuator," to be submitted to *Journal of Intelligent Material Systems and Structures*.

Interactions/Transitions

1. Clark, R. L., J. A. Rule, and R. E. Richard, 2000. "Application of Reduced-Order Models to the Design of Adaptive Aeroelastic Structures," (**Invited Paper**) Presented at the 139th Meeting of the Acoustical Society of America, 107(5), Atlanta, GA, May 31, 2824.
2. Ardelean, Emil, and R. L. Clark, "V-Stack piezoelectric actuator," *Smart Structures and Materials 2001: Active Materials: Behavior and Mechanics*, *Proc. SPIE 4333*, pp. 323-333, 2001.
3. Rule, J. A., Richard, R. E., and Clark, R. L., 1999. "Design of an Aeroelastic Delta Wing Model for Active Flutter Control," *Proceedings of Active 99*, Fort Lauderdale, FL, December 2-4.

Inventions/Patents

Provisional Patent Application: V-Stack Piezoelectric Actuator

Accepted for
Publication in the
AIAA Journal

Revised Manuscript

EXPERIMENTAL AND THEORETICAL STUDY ON FLUTTER AND LIMIT CYCLE OSCILLATIONS OF HIGH-ASPECT RATIO WINGS

Demian Tang¹ and Earl H. Dowell²

Duke University, Durham, North Carolina 27708-0300

ABSTRACT

An experimental high-aspect ratio wing aeroelastic model with a slender body at the tip has been constructed and the response due to flutter and limit cycle oscillations (LCO) has been measured in a wind tunnel test. A theoretical model has been developed and calculations made to correlate with the experimental data. Structural equations of motion based on nonlinear beam theory are combined with the ONERA aerodynamic stall model to study the effects of geometric structural nonlinearity and steady angle of attack on flutter and LCO of high-aspect ratio wings. Static deformations in the vertical and torsional directions caused by a steady angle of attack and gravity are measured, and results from theory and experiment are compared. A dynamic perturbation analysis about a nonlinear static equilibrium is used to determine the small perturbation flutter boundary which is compared to the experimentally determined flutter velocity and oscillation frequency. Time simulation is used to compute the LCO response. The results between the theory and experiment are in good agreement

¹Research Associate Professor, Department of Mechanical Engineering and Materials Science. Member

for static aeroelastic response, the onset of flutter, dynamic LCO amplitude and frequency.

Nomenclature

c, \bar{c}	wing chord and dimensionless chord, c/L
c_{SB}	chord of slender body
C_l	section lift coefficient
C_d	section drag coefficient
C_m	section torsional moment coefficient
C_ξ	structural damping
dD, dL	section drag and lift forces
dM_0	section pitch moment about 1/4 chord
dF_v, dF_w	section chordwise and vertical component forces
dM_x	section pitch moment about elastic axis
e	section mass center from elastic axis
E	modulus of elasticity
g	gravitational constant
G	shear modulus
I_1, I_2	vertical, chordwise area moments
J	torsional stiffness constant
K_m	wing mass radius of gyration
L	wing span
m	mass per unit length of the wing
M	tip mass of the wing
N	total number of modes

NN	number of aerodynamic elements
t	time
U	free stream velocity
v	chordwise or edgewise bending deflection
w	vertical or flapwise bending deflection
V_j, W_j	generalized co-ordinates for bending
x	position co-ordinate along wing span
y_{ac}	distance of aerodynamic center of airfoil section from elastic axis
α_l	wing section angle of attack
θ_0	steady angle of attack at root section
ρ	air density
ϕ	twist about deformed elastic axis
$\omega_{\phi j}$	j th torsional natural frequency of wing
ω_{vj}	j th chordwise natural frequency of wing
ω_{wj}	j th vertical natural frequency of wing
Δ_l	dimensionless width of l th spanwise aerodynamic element
Φ_j	generalized co-ordinates for torsion
$(\)'$	$d(\)/dx$
$(\)\dot{\ }$	$d(\)/dt$

INTRODUCTION

Aeroelastic stability and response of an aircraft with a high-aspect-ratio wing have been studied for many years from subsonic to supersonic flow. Most investigators have used linear beam theory to simplify the wing structural model. As shown in Ref.[1-3], however, a geometric structural nonlinearity may arise from the coupling between elastic flap or vertical bending, chordwise or edgewise bending and torsion for very high aspect ratio wings typical of Uninhabited Air Vehicles (UAV). In [2,3] the effect of the large static pre-flutter deformation on the flutter boundary and LCO response has been studied. The results provide additional insight with respect to the contribution of structural nonlinear coupling to the aeroelastic stability and response of high-aspect-ratio wings. By flap or vertical bending is meant bending perpendicular to the wing chord and by chordwise or edgewise bending is meant bending in the direction parallel to the wing chord.

An experimental high-aspect ratio wing aeroelastic model with a tip mass has been constructed and a wind tunnel test conducted to measure the static aeroelastic response, flutter and limit cycle oscillations. The goal is to assess experimentally the theoretical results of earlier studies, [2,3]. The theoretical structural equations of motion are based on nonlinear beam theory [1] and the original ONERA aerodynamic stall model [4]. Large static pre-flutter deformations in the vertical or torsional direction are created by the gravity loading on the wing and a tip slender body, and a steady angle of attack which creates a static aerodynamic load on the wing.

A dynamic perturbation equation about a nonlinear static equilibrium is derived which is used to determine the flutter boundary. A direct time marching solution is also used to calculate the large amplitude response behavior of this nonlinear system both above and

below the nominal, perturbation flutter boundary i.e. the flutter boundary determined from the dynamical equations linearized about a nonlinear static equilibrium state.

Prior to the wind tunnel test, a static and vibration test of the experimental model has been made and the results compared to the theoretical predictions. Also we use the present theoretical method to correlate with an earlier experiment conducted by Dowell, Traybar and Hodges [5]. A discussion of these latter results and correlation with the measured data are given in the Appendix.

This paper is a complement to the studies reported earlier by Patil, Hodges and Cesnik [2,6,7], by Tang and Dowell [3] and by Dowell, Traybar and Hodges [5].

EXPERIMENTAL WING MODEL AND MEASUREMENTS

The experimental model includes two parts: a high-aspect ratio wing with a slender body at the tip and a root support mechanism. The wing is rectangular, untwisted and flexible in the flap, lag and torsional directions. The wing is constructed from a precision ground flat steel spar with mass uniformly distributed along the wing span. The spar is 18 inches in length, 0.5 inches in width and 0.05 inches in thickness. It is inserted tightly into the wing root mechanism. In order to reduce torsional stiffness, the spar has multiple thin flanges along the span. The flange width is 0.05 inch and it is 0.125 inches in deep. There are 2×33 flanges uniformly and symmetrically distributed along the wing span and center line of the spar. There are 18 pieces of NACA 0012 airfoil plate uniformly distributed along the span. The pieces of the airfoil plate are made of aluminum alloy with 0.1 inch thickness.

A precision aerodynamic contour of the wing model is obtained. Each airfoil plate has a slot 0.5 inches in width and 0.05 inches in thickness at the symmetry line. The spar is inserted through these airfoil plate slots and they are permanently bonded together. Each space between two airfoil plates is filled with a light wood (bass) covering the entire chord and span which provides the aerodynamic contour of the wing. This wood provides a slight additional mass and a small addition to the bending and torsion stiffness.

A slender body is attached to the elastic axis of the wing tip. The slender body is an aluminum bar, 3/8 inch in diameter and 4 inches in length. A paraboloidal forebody and an aftbody with 0.45 inch length are fixed to two ends of the bar. The forebody and aftbody are made of brass. The geometry of the paraboloidal forebody is described as follows

$$R/R_0 = \bar{y}^2, \quad \bar{y} = 0 \longrightarrow 1$$

The slender body is symmetrical and is designed to provide enough torsional inertia to reduce the natural torsional frequency sufficiently to induce flutter in the velocity range of the wind tunnel.

A physical representation of wing model is shown in Figure 1.

The root support mechanism is a socket that allows a change of the steady angle of attack at the root. The root socket is mounted to the mid point of side-wall of the wind tunnel as shown in Figure 2 which is a photograph of the aeroelastic wing model in the wind tunnel.

Axial strain gages for bending modes and a 45⁰ oriented strain gage for torsional modes were glued to the root spar to measure the bending-torsional deflections of the wing. Signals from the strain gages were conditioned and amplified before their measurement through a

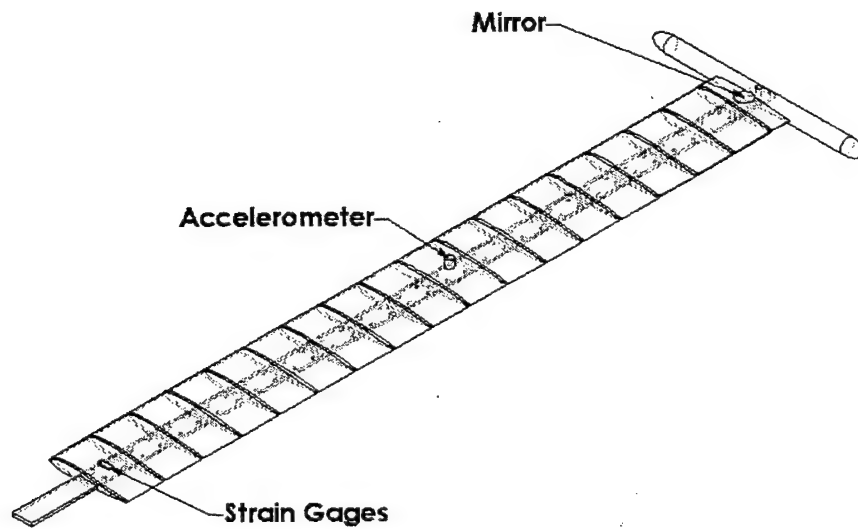


Figure 1: Physical representation of wing model.

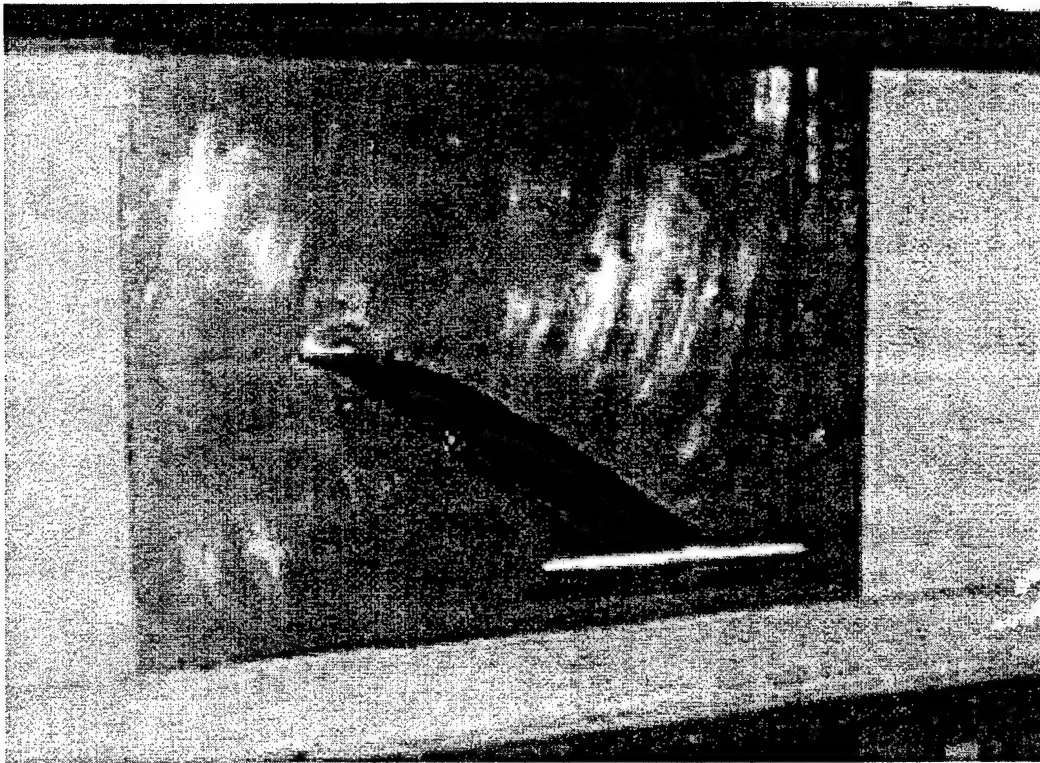


Figure 2: Photograph of the experimental model in the wind tunnel.

gage conditioner and a low-pass filter. A micro-accelerometer is mounted at the mid-span of the wing. The output signals from these transducers are directly recorded on a computer with data-acquisition and analysis software, Lab-VIEW 5.1.

A Helium-Neon Laser with 0.8mw randomly polarized and wavelength 633 (nm) is mounted on the top of the tunnel. The top of the tunnel is made of a glass plate with a thickness of 0.5 inch. A mirror, 0.5 inch in diameter, is fixed on the tip of the wing. A "mirror" deflection technique is used to determine the geometric twist angle and the vertical or flapwise bending slope at the wing tip.

All static, flutter and LCO response tests were performed in the Duke University low speed wind tunnel. The wind tunnel is a closed circuit tunnel with a test section of $2.3 \times 1.75 \text{ ft}^2$ and a length of 5 ft. The maximum air speed attainable is 293 ft/sec.

The basic parameters of the experimental wing model were obtained from standard static and vibration tests and are listed in the Table 1.

NONLINEAR AND PERTURBATION FLUTTER EQUATIONS

Structural Model:

According to the Hodges-Dowell equations [1], for an uniform, untwisted elastic wing, neglecting cross-section warping, the equations of motion may be written as

$$\begin{aligned}
 EI_2 v'''' + (EI_2 - EI_1)(\phi(w)''') + m\ddot{v} + C_\xi \dot{v} + (M\ddot{v} + I_v \ddot{v}')\delta(x - L) \\
 = \frac{dF_v}{dx} + \Delta F_v - (Mg\delta(x - L) + mg)\sin\theta_0
 \end{aligned} \tag{1}$$

$$\begin{aligned}
& EI_1(w)'''' + (EI_2 - EI_1)(\phi v'')'' + m\ddot{w} - me\ddot{\phi} + C_\xi \dot{w} + (M\ddot{w} + I_w \ddot{w}')\delta(x - L) \\
& = \frac{dF_w}{dx} + \Delta F_w - (Mg\delta(x - L) + mg)\cos\theta_0
\end{aligned} \tag{2}$$

$$\begin{aligned}
& -GJ\phi'' + (EI_2 - EI_1)w''v'' + I_\phi \ddot{\phi}\delta(x - L) + mK_m^2 \ddot{\phi} + C_\xi \dot{\phi} - me\ddot{w} \\
& = \frac{dM_x}{dx} + \Delta M_x
\end{aligned} \tag{3}$$

A few general comments about Equations [1-3] may be in order. First of all by multiplying each of these equations by δv , δw and $\delta \phi$ respectively and integrating over the length of the beam, a variational statement may be derived. Conversely as shown in Ref.[1], these equations may be derived from Hamilton's principle.

Note that in Eq.[1]-[3] only the most important nonlinear terms are retained from the Hodges-Dowell equations and the third and higher order geometrically nonlinear terms are neglected here. Also note that the geometric twist angle $\hat{\phi} = \phi + \int_0^x v'w''dx$ is considered in the aerodynamic terms. M is the tip mass and I_v, I_w and I_ϕ are the tip inertial terms, and θ_0 is the pitch angle or steady angle of attack at the root of this wing model. e is the distance between mass center and wing elastic axis center.

The aerodynamic forces include two parts. One contribution is from the wing surface, $\frac{dF_w}{dx}$, $\frac{dF_v}{dx}$ and $\frac{dM_x}{dx}$, and the other is from the slender body at the wing tip, $\Delta F_w, \Delta F_v$ and ΔM_x .

Part one (ONERA aerodynamic airfoil model):

The v and w components of the aerodynamic force, and the aerodynamic moment about

the elastic axis can be expressed as follows.

$$dF_w = dL - (\phi_\lambda - \theta_0)dD \quad (4)$$

$$dF_v = -dD - (\phi_\lambda - \theta_0)dL$$

$$dM_x = dM_0 - y_{ac}dF_w$$

where

$$dL = \frac{1}{2}\rho c U^2 C_l dx$$

$$dD = \frac{1}{2}\rho c U^2 C_d dx$$

$$dM_0 = \frac{1}{2}\rho c^2 U^2 C_m dx$$

$$\phi_\lambda \approx \dot{w}/(U + \dot{v} + \dot{w}\theta_0)$$

$$\alpha = \hat{\phi} + \theta_0 - \phi_\lambda$$

The section aerodynamic coefficients C_l , C_d and C_m are obtained from the original ON-ERA stall aerodynamic model, see Ref.[4,8]. These airfoil relationships are combined with a strip theory assumption to determine the wing aerodynamic forces. Patil et al [7] have shown the strip theory assumption is a good one for such high aspect ratio wings.

Part two (slender body theory):

We follow Bisplinghoff, Ashley and Halfman [9], pg. 418 et seq and use their equation numbers. Using essentially the nomenclature of [9], we define $h = w_{x=L}$, $\alpha = \phi_{x=L}$, $L = \Delta F_w$, $M_x = \Delta M_x$ but use the symbol y to denote chordwise position. Then the vertical displacement at the wing tip is

$$Z_a = -h - \alpha[y - y_B] \quad \text{Eq.(7-136)}$$

where $y_B \equiv y_{ea}$, is the distance from leading edge to the elastic axis of the slender body.

Here h , + up, and α , + nose up. Now the downwash or convected vertical velocity is

$$W_a = \frac{\partial Z_a}{\partial t} + U \frac{\partial Z_a}{\partial y} = \frac{DZ_a}{Dt} \quad (7-137)$$

where $D \equiv \frac{\partial}{\partial t} + U \frac{\partial}{\partial y}$

Thus from [9],

$$\frac{dL}{dy} = -\rho \frac{DS}{Dt} - \rho S \frac{D^2 Z_a}{Dt^2} = -\rho \frac{D}{Dt} [S \frac{DZ_a}{Dt}] \quad (7-140)$$

where $S \equiv$ body cross-sectional area and $S = \pi R^2$, for a circular cross-section of radius, $R(y)$.

$$\text{Note} \quad \frac{DS}{Dt} = U \frac{dS}{dy} \quad (7-142)$$

Then Eq.(7-140) becomes

$$\frac{dL}{dy} = -\rho U \frac{dS}{dy} \frac{DZ_a}{Dt} - \rho S \frac{D^2 Z_a}{Dt^2} \quad (7-143)$$

Now, $L \equiv \int_0^{c_{SB}} \frac{dL}{dy} dy$ and $M_x \equiv \int_0^{c_{SB}} \frac{dL}{dy} [y - y_B] dy$

where $c_{SB} \equiv$ chord of slender body.

Using Eq. (7-136),

$$\begin{aligned} \frac{DZ_a}{Dt} &= -\dot{h} - \dot{\alpha}[y - y_B] - U\alpha \\ \frac{D^2 Z_a}{Dt^2} &= -\ddot{h} - \ddot{\alpha}[y - y_B] - 2U\dot{\alpha} \end{aligned}$$

thus

$$\Delta F_w = L \equiv \int_0^{c_{SB}} \frac{dL}{dy} dy = \rho[\ddot{h} + U\dot{\alpha}] \int_0^{c_{SB}} S dy + \rho\ddot{\alpha} \int_0^{c_{SB}} S[y - y_B] dy \quad (4-1)$$

and

$$\begin{aligned} \Delta M_x = M_x \equiv & - \int_0^{c_{SB}} \frac{dL}{dy} [y - y_B] dy = \rho U[\dot{h} + U\alpha] \int_0^{c_{SB}} S dy \\ & - \rho\ddot{h} \int_0^{c_{SB}} S[y - y_B] dy - \rho\ddot{\alpha} \int_0^{c_{SB}} S[y - y_B]^2 dy \end{aligned} \quad (4-2)$$

Note that $\int_0^{c_{SB}} \frac{dS}{dy} dy = - \int_0^{c_{SB}} S dy$ if $S=0$ at $y = 0, c_{SB}$, i.e. for a pointed body.

Also, recall the sign convention is y - positive aft, L - positive up and M_x - positive nose up.

If we assume the slender body drag can be neglected, then

$$\Delta F_v = -(\phi_\lambda - \phi - \theta_0)\Delta F_w \quad (4-3)$$

Modal Equations:

Expansions in general mode shape functions are used to obtain ordinary differential equations in terms of generalized co-ordinates from Eq.(1)-(3). They are expressed in series form as follows.

$$\begin{aligned} \bar{v} &= \sum_{j=1}^N V_j(t) \psi_j(\bar{x}) \\ \bar{w} &= \sum_{j=1}^N W_j(t) \psi_j(\bar{x}) \\ \phi &= \sum_{j=1}^N \Phi_j(t) \Theta_j(\bar{x}) \end{aligned} \quad (5)$$

where the over-bar indicates non-dimensionalization with respect to the wing span, L , and ψ_j, Θ_j are the j^{th} normal modes of the associated linear structural model.

Let $\{q\}$ be a state vector which is defined as

$$\{q\} = \{\dot{V}_j, V_j, \dot{W}_j, W_j, \dot{\Phi}_j, \Phi_j, C_{ll}, C_{ml}, C_{dl}\}$$

where the structural mode number is $j = 1, 2, \dots, N$, and the aerodynamic section number along the span of the wing is $l = 1, 2, \dots, NN$. Using the Galerkin method, one obtains a set of state-space matrix equations from equations (1)-(5),

$$[\mathcal{A}] \{\dot{q}\} + [\mathcal{B}] \{q\} = \{F_0\} + \{F_N\} \quad (6)$$

Note the coefficient matrices, $[\mathcal{A}]$, $[\mathcal{B}]$ are dependent on the flow and structural parameters. The force vectors F_0 and F_N are static force obtained from the effects of gravity and the nonlinear forces obtained from the structural nonlinearity and stall aerodynamics, respectively.

Equation (6) is the set of nonlinear equations of motion. A strictly linear flutter boundary is determined using equation (6) by setting $F_N \equiv 0$ and $F_0 = 0$. There is no effect on the strictly linear flutter boundary of a pre-flutter static deflection or initial conditions. For $F_N \neq 0$ and a large static pre-flutter deformation, a dynamic perturbation approach is used to determine the small perturbation flutter boundary of this nonlinear system about a nonlinear and non-trivial static equilibrium condition. That is, one assumes that

$$q = \bar{q} + \hat{q} \quad (7)$$

where \bar{q} is the static equilibrium state variables and the corresponding quantities with a symbol of $(\hat{\cdot})$ are the small (linear) dynamic perturbations about the static equilibrium state.

Substituting equation (7) into Eq.(6), a set of static equilibrium equations and dynamic perturbation equations is obtained. The static equilibrium equations comprise a set of non-linear algebraic equations for the unknown state vector $\{\bar{q}\}$

The dynamic perturbation equations about a static equilibrium state are

$$[\bar{\mathcal{A}}] \{\dot{\hat{q}}\} + [\bar{\mathcal{B}}] \{\hat{q}\} = \{0\} \quad (8)$$

Note the coefficient matrices, $[\bar{\mathcal{A}}]$, $[\bar{\mathcal{B}}]$ are dependent on the flow velocity and the static equilibrium state, e.g. U , \bar{q} etc.

To determine the dynamic nonlinear response of this aeroelastic system, we can use equation (6) and a time marching approach.

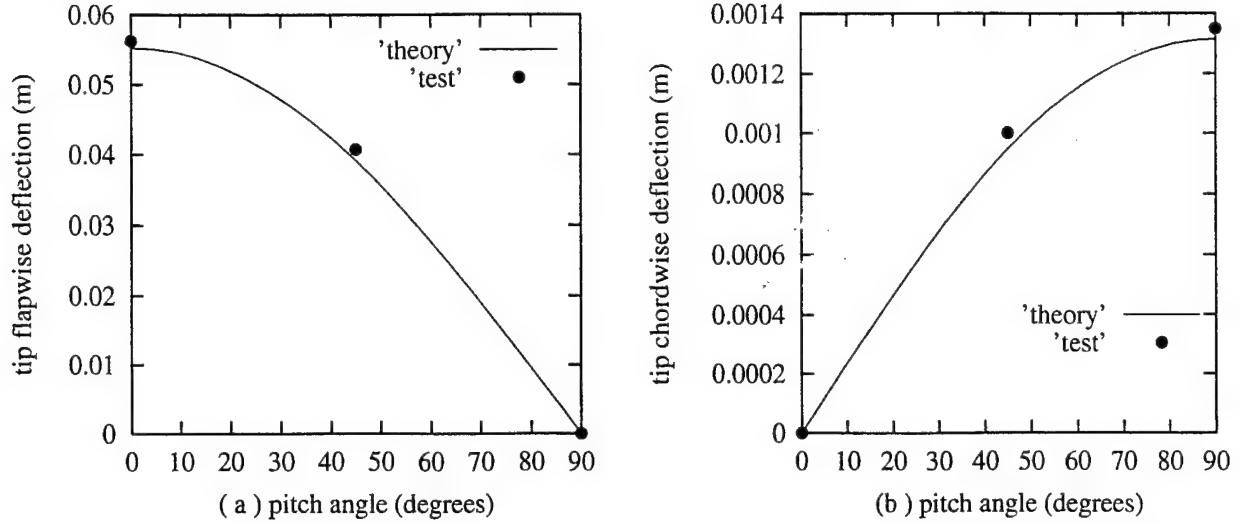
A note on the sign convention may be helpful here. Vertical bending deflection, w , and the direction of gravity are taken as positive up. Chordwise bending deflection, v , is taken as positive aft. And the torsional deflection and angle of attack are taken positive nose up. Note that since gravity is positive up, we are flying the wing upside down and, for example, a negative angle of attack is required to provide a lift downward to balance the wing weight.

CORRELATION BETWEEN THEORY AND EXPERIMENT

1. Static Deflections and Natural Frequencies Under Gravity Loading

The root mechanism of the experimental wing model is mounted to a very heavy support frame which is attached to the ground. The root support mechanism allows the model to have a prescribed angle of attack or pitch from $\theta_0 = 0^\circ \rightarrow 90^\circ$. For assessing the static flap and chordwise bending deflections and twist at tip vs θ_0 under gravity loading only, three special pitch angles are considered i.e $\theta_0 = 0^\circ, 45^\circ$ and 90° . The data are determined by directly measuring the difference between the undeformed and deformed tip position. The theoretical results are obtained from equation (1)-(3) and setting the aerodynamic terms to zero. We use a time marching approach to solve equation (1)-(3) and to determine the steady solution, i.e. the static deflections. The wing structural modes retained in the analysis were one chordwise mode, four flap modes and one torsional mode. Preliminary calculations with various modal combinations verified that good convergence is achieved with these modes in the analysis. The results are shown in Figure 3(a)-(c) for the tip flap (a), and chordwise (b) bending deflections and tip twist (c) vs pitch angle. The solid line indicates the theoretical results and the symbols, \bullet , are from experiment. The agreement for the flap and chordwise deflections is excellent and for the twist is reasonably good.

The natural frequencies are determined by measuring the transfer function of input force and output root strain or acceleration. A force transducer B&K 8200 fixed near the wing root is excited by a mini-shaker B & K 4810 and a power amplifier B & K 2706. A four-channel signal analyzer (SD 380) provides a sweeping sinusoidal signal. The output signals from



strain gages (flap bending and torsion) and a micro-accelerometer (chordwise) are inputs to the SD380 for transfer function analysis.

The theoretical results are obtained in terms from an eigenanalysis of the dynamic perturbation equation (8) and setting the aerodynamic terms to zero. The static equilibrium positions are determined by using the time marching approach Eq.(1)-(3). The results are shown in Figure 4(a)-(c) for the fundamental natural frequency vs pitch angle of attack. Figure 4(a) is for flap, and (b) for chordwise bending deflections and (c) for torsion. Of course these motions are coupled in general. The solid line indicates the theoretical results and the symbols, \bullet , are from experiment. The agreement for the chordwise frequency is excellent and for the flap and twist is reasonably good. The flap frequency has a slight change from $\theta_0 = 0^\circ \rightarrow 90^\circ$ experimentally. The chordwise frequency decreases as θ_0 decreases from 90° to 0° , while the torsion frequency increases.

A correlation study was also conducted using earlier experimental data reported by Dowell, Traybar and Hodges [5]. The results are included here in the Appendix.

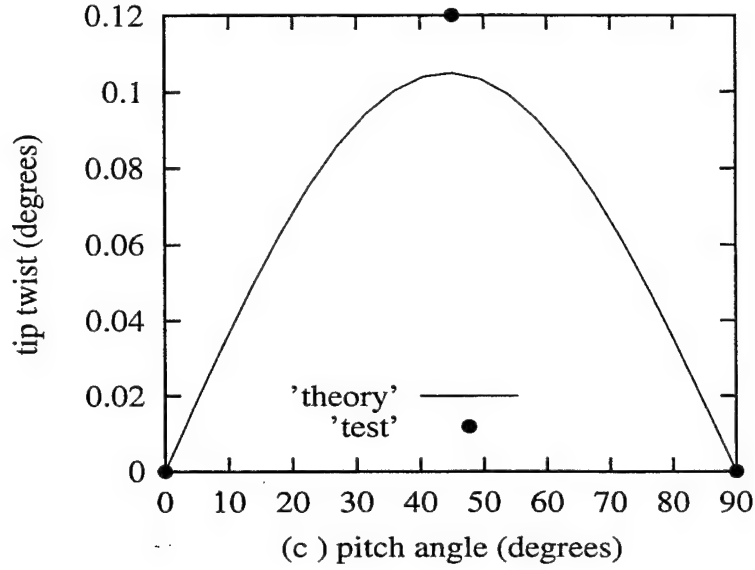


Figure 3: Static flap (a), and chordwise (b) bending deflections and tip twist (c) at tip vs pitch angle. Gravity loading only.

In general good theoretical/experimental agreement is found. Indeed it is somewhat better than that found in [5].

2. Static Aeroelastic Deflections of the Wing

We use a "mirror" deflection technique to measure the tip static aeroelastic deflections of the wing. A point determined by a reflected light source is marked on a readout grid paper placed on the top of the wind tunnel when the wing is undeflected. The readout grid paper is calibrated in the tip flap and twist deflections before the test. The reflected light source point with wing deflection as marked on the readout paper is then determined as the flow velocity is varied.

The theoretical results are obtained from equation (6) using the time marching approach.

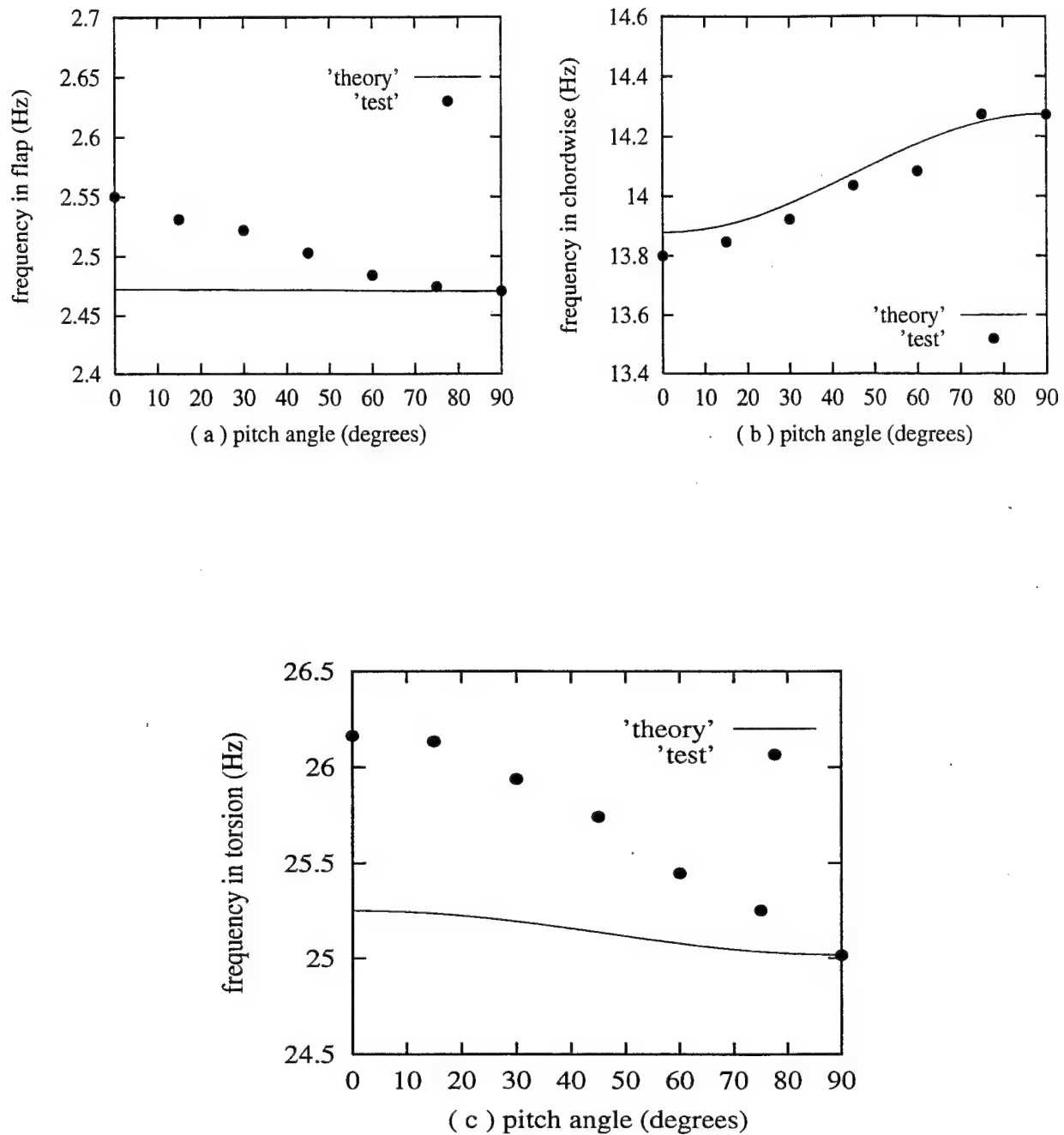


Figure 4: Fundamental natural frequency vs pitch angle, (a) flap, and (b) chordwise bending and (c) torsion.

The flow velocity is below the flutter velocity for these measurements and calculations. The wing is divided into ten (10) spanwise aerodynamic sections, i.e. $NN = 10$. The stall aerodynamic data for an NACA 0012 airfoil are used in this paper, see Ref.[7].

The theoretical and experimental results are shown in Figure 5(a) and (b) for a steady angle of attack, $\theta_0 = 1^\circ$. Figure 5(a) is for the tip flapwise deflection and (b) for the tip twist. The solid line indicates the theoretical results and the bar indicates the measured data. The experimental data appear have some scatter due to the turbulent aerodynamic noise, although the noise is small. A very high measurement sensitivity is obtained from the mirror technique. We use a bar in the figure to indicate the magnitude of the response uncertainty. As shown Figure 5, both the tip and twist deflection increase with increasing flow velocity, but the tip deflection is always negative until the flow velocity reaches 34.5 m/s. At that velocity the aerodynamic forces provide sufficient lift to overcome the effect of gravity. At $U=34.5$ m/s, the system enters into the flutter instability range. The consequent LCO has a certain non-zero mean or temporal average and this is shown by a dashed line in Fig.5. Also with LCO, aerodynamic stall occurs and the lift coefficient C_l suddenly decreases. The measured data in Fig.5 are acquired before the onset of flutter and LCO. The experimental LCO data will be discussed in the next section. The experimental data fall near the theoretical curves in Fig.5. In general, the agreement is good except for some points at $U=10,15$ m/s. In the higher flow velocity range, the data fluctuation increases due to greater aerodynamic turbulence.

Figure 6 shows the static aeroelastic deflections at the tip for $\theta_0 = 2.2^\circ$. The balance between aerodynamic forces and the effect of gravity now occurs at $U=25$ m/s. Compared to

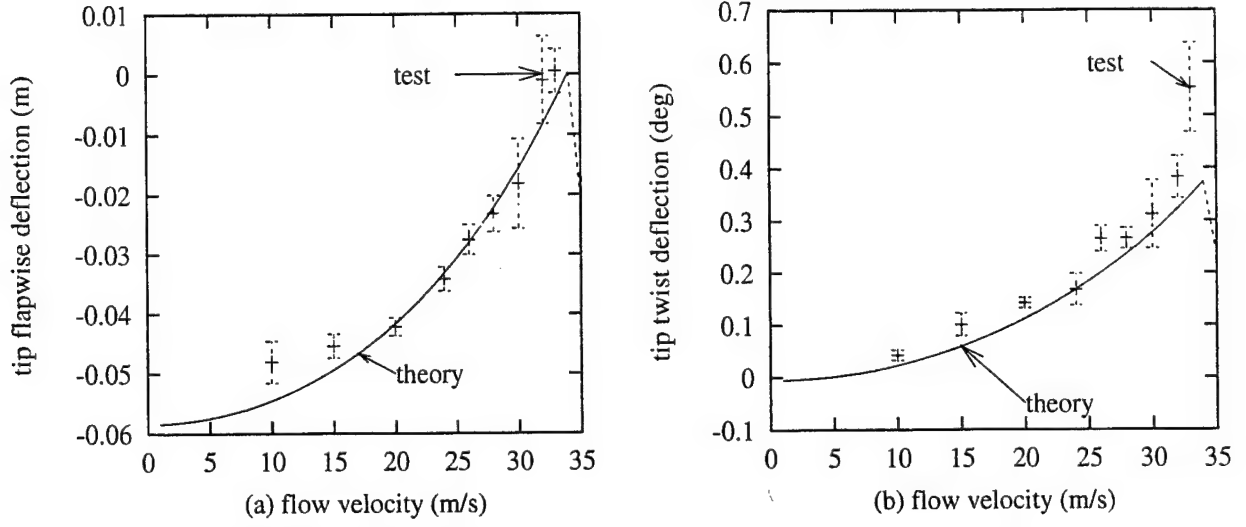


Figure 5: Static aeroelastic deflections of the wing vs flow velocity for pitch angle of attack $\theta_0 = 1^\circ$ (a) flap, (b) twist.

the results for $\theta_0 = 1^\circ$, Figure 5, a similar result is obtained, but the magnitude of the static aeroelastic deflections is larger than those for the $\theta_0 = 1^\circ$ and a better agreement between experiment and theory is found.

3. Flutter and LCO response

Very clear flutter and LCO response are observed in the present wind tunnel test. Flutter and LCO response are determined for seven different steady angles of attack, i.e. $\theta_0 = 0.25^\circ$, 0.5° , 0.7° , 1.0° , 1.2° , 1.5° and 1.7° . For the safety of this wing model, we did not determine flutter or LCO in the range of $\theta_0 \leq 0^\circ$ or $\theta_0 \geq 2^\circ$.

The theoretical results are obtained from the dynamic perturbation equation (8) and also using a time marching approach for the full nonlinear equations (6). For no static wing deformation, the strictly linear flutter speed and frequency are found to be 34.4 m/s

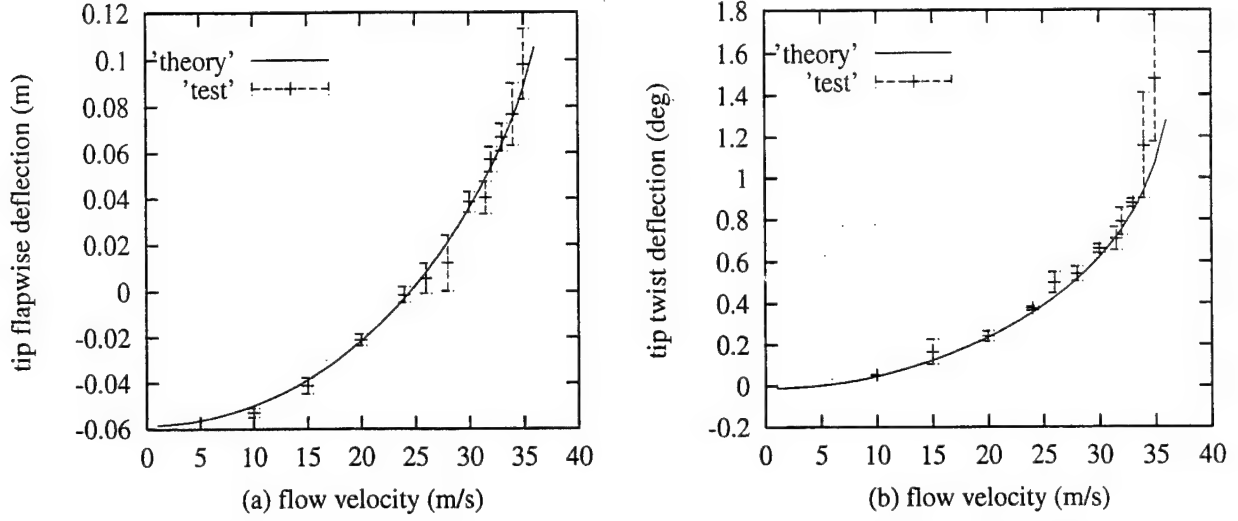


Figure 6: Static aeroelastic deflections of the wing vs flow velocity for pitch angle of attack $\theta_0 = 2.2^\circ$ (a) flap, (b) twist.

and 22.57 Hz respectively. In this case, we considered the effects of the tip slender body aerodynamics on flutter. The results are $U_f = 34.2$ m/s and $\omega_f = 22.44$ Hz without tip slender body aerodynamics included. The effect of the tip body aerodynamics is thus seen to be small.

Figure 7(a),(b) show a graphical representation of the perturbation equations eigenanalysis in the form of real eigenvalues $Re(\lambda_i)$ (damping) vs the flow velocity and also a root-locus plot (frequency vs. damping) as indicated by the symbol \circ . There is a intersection of $Re(\lambda_i)$ with the velocity axis at $U_f = 34.5$ m/s and the corresponding flutter oscillatory frequency is $\omega_f = 22.59$ Hz for $\theta_0 = 1^\circ$. For no static wing deformation, the strictly linear flutter results are also shown in the figure as indicated by the symbol \bullet . The two results are almost the same. The reason can be explained by figure 5(a). Here, the static tip deflection approaches zero when the system is near the flutter velocity. The effects of the geometric structural nonlinearity thus become small near the flutter condition.

Similar to the above results, Figure 8(a),(b) show the eigenanalysis for $\theta_0 = 1.7^\circ$. The flutter velocity is $U_f = 35.2$ m/s and the corresponding flutter oscillatory frequency is $\omega_f = 22.8$ Hz. The flutter velocity and frequency increase 2.3% and 1% as compared to the strictly linear results. In this case we find the tip deflection is 0.05 (m) when $U = 35.2$ m/s. The effects of the structural nonlinearity are to increase the stability. From Figure 4(c), it is seen that the natural torsional frequency of the wing model increases as the tip deflection increases.

The effects of the structural nonlinearity depend upon the bending stiffness ratio of EI_2/EI_1 . In Ref.[3], it is shown that the angle of twist and the ratio of the flapwise deflection to wing span vary as the square root of EI_1/EI_2 for the LCO amplitude and/or the initial disturbance required to initiate LCO. For the present wing model EI_2/EI_1 is only 44.05 which is much lower than the wing model used in Ref.[2,3] ($EI_2/EI_1 = 200$). Thus the nonlinear effects should be weaker, i.e. the LCO amplitude or the initial disturbance required to initiate LCO is larger for larger EI_1/EI_2 or smaller EI_2/EI_1 .

Figure 9 shows the dynamic perturbation flutter velocity (a) and frequency (b) vs the pitch angle of attack from both theory and experiment. The solid line is for the dynamic perturbation solution and the symbol, \bullet , is for the experimental data (onset velocity of flutter or LCO). For comparison, the linear flutter solution is also plotted in this figure as shown by the broken line. The linear flutter solution is near the minimum flutter velocity and is located at a pitch angle between $\theta_0 = 1^\circ$ and 1.2° . The maximum error between theory and experiment is only about 3%. The experimental flutter frequency is lower than those for the theory. The maximum error is about 5.4%.

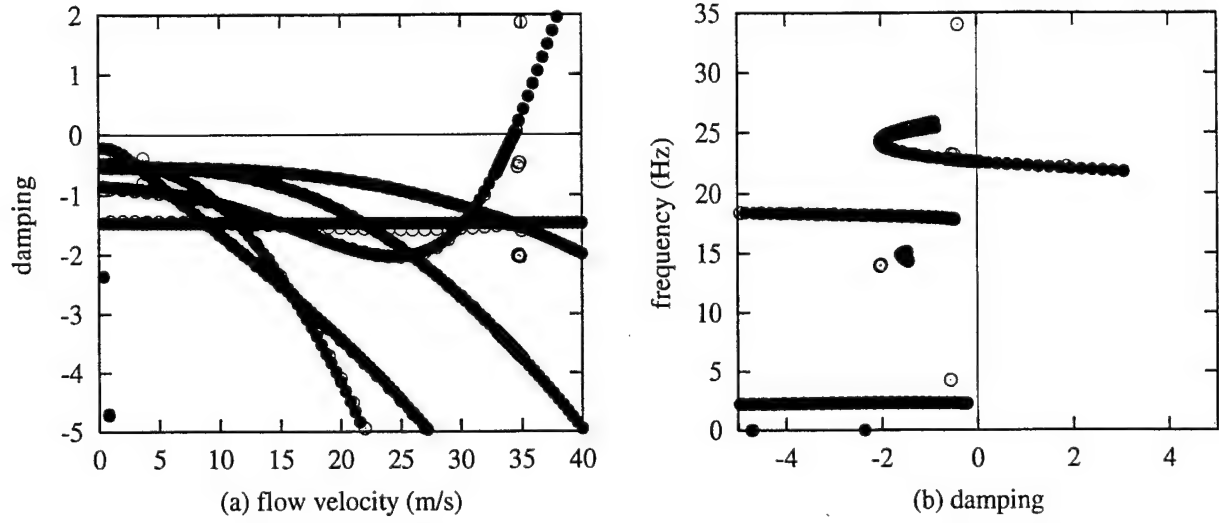


Figure 7: Perturbation eigenvalue solution of the nonlinear aeroelastic system for $\theta_0 = 1^\circ$,
(a) for real part and (b) for root-locus.

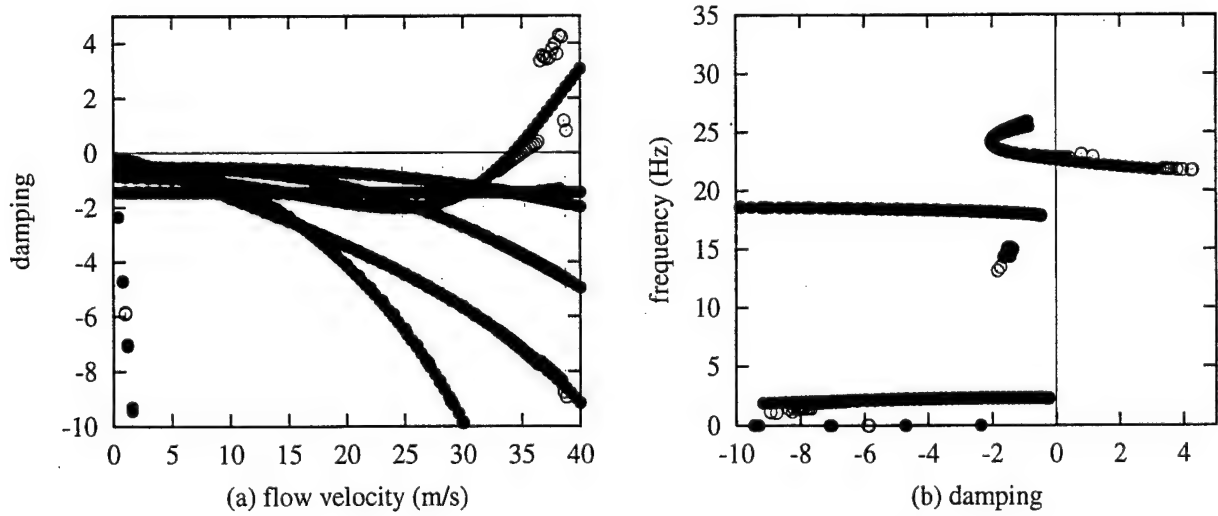


Figure 8: Perturbation eigenvalue solution of the nonlinear aeroelastic system for $\theta_0 = 1.7^\circ$,
(a) for real part and (b) for root-locus.

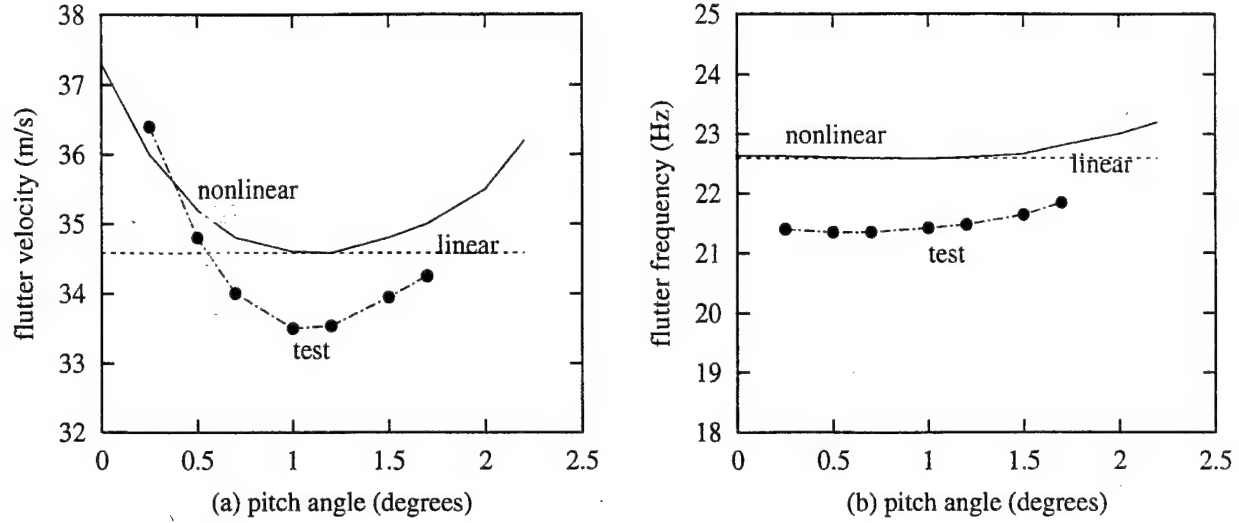


Figure 9: Perturbation eigenvalue solution of the nonlinear aeroelastic system vs pitch angle, (a) flutter velocity and (b) flutter frequency.

Figure 10 shows the theoretical LCO time history of the mid-span flapwise deflection (a) and the tip twist deflection (b) for $U=35$ m/s and $\theta_0 = 1^\circ$. From Figure 10, we find the stall aerodynamic nonlinearity leads to a limit cycle oscillation.

Figure 11 shows a comparison between theoretical and experimental time histories and the corresponding FFT analysis for flapwise deflection at the mid-span point for $U=35$ m/s and $\theta_0 = 1^\circ$. (a) is the theoretical time history from $t=29$ to 30 second, (b) is the measured time history and (c) is the FFT analysis. The motion includes two dominant frequency components. One is 22.59 Hz from the theory and 21.4 Hz from test which corresponds to the flutter frequency. The other is 45 Hz from theory and 42 Hz from test which is close to the second harmonic of the flutter frequency. The response is dominated by the flutter frequency. The agreement between theory and experiment is reasonably good.

As shown in Figure 7(b), it is found the flutter mode is dominated by the coupling

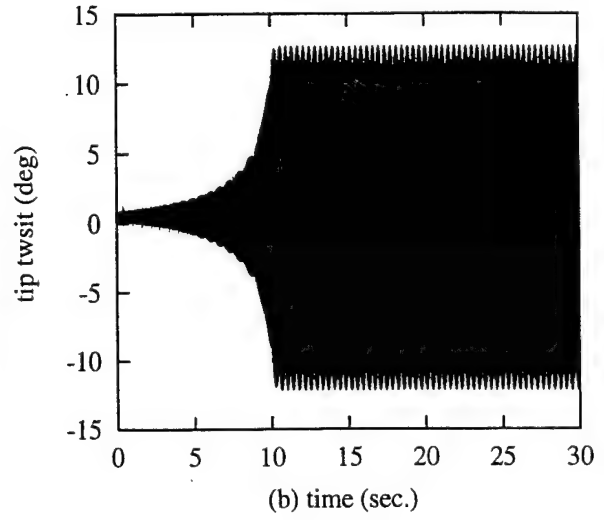
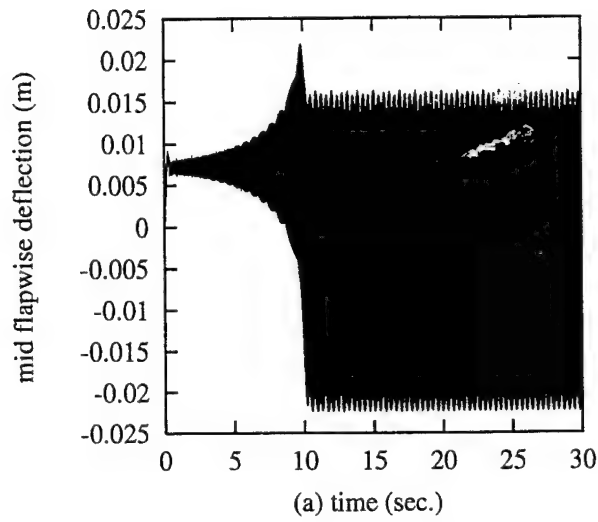
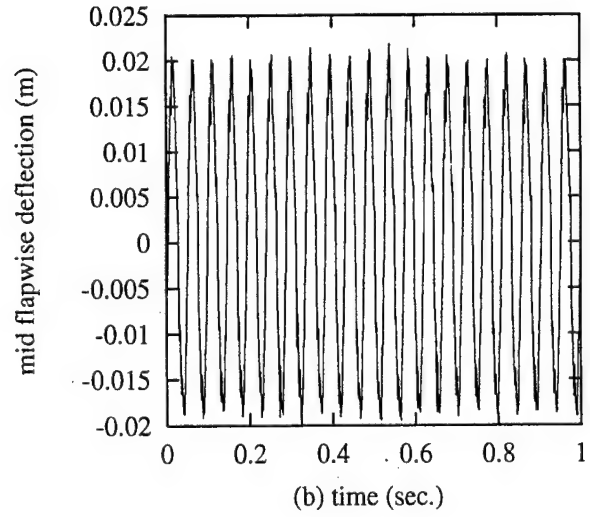
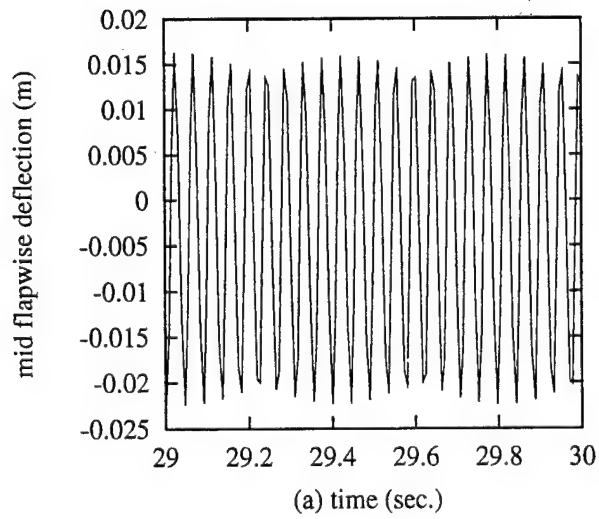


Figure 10: Time history for $U=35$ m/s and $\theta_0 = 1^\circ$, (a) mid-span flapwise deflection (b) tip twist.



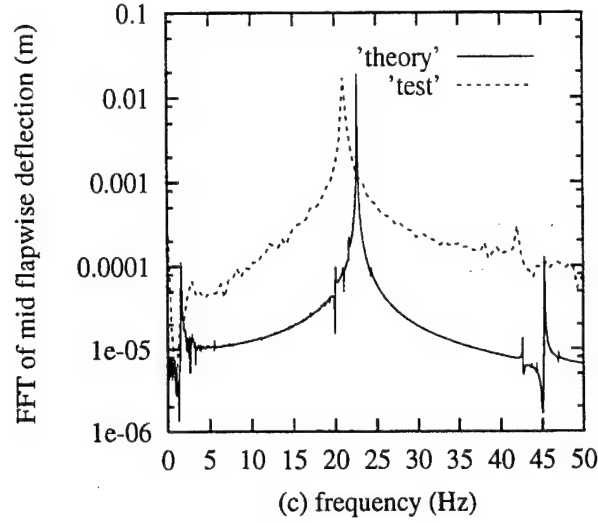


Figure 11: Time history for $U=35$ m/s and $\theta_0 = 1^\circ$, mid-span flapwise deflection, (a) theory, (b) measured data and (c) FFT analysis.

between the first torsion mode and second flap mode. The LCO vibration mode shape is similar to the flutter mode. Figure 12 shows the theoretical LCO mode shape for $U=35$ m/s and $\theta_0 = 1^\circ$. This LCO mode shape is also observed in the wind tunnel test and has been recorded on video tape. The experimental data point at the mid-span is also plotted on this figure.

When the flow velocity is high, the theoretical LCO response appears as a beat oscillation, but this was not observed in the test. As an example, Figure 13(a) shows the theoretical time history and 13(b) shows the corresponding FFT analysis for $U=38$ m/s and $\theta_0 = 1^\circ$. The very close frequencies are 20.96 Hz and 22.63 Hz which are both important for the response. However, 22.63 HZ seems more significant.

Other interesting results are the phase plane plots of the motion at the wing tip. We use the "mirror" deflection technique to measure the twist deflection and flapwise bending slope

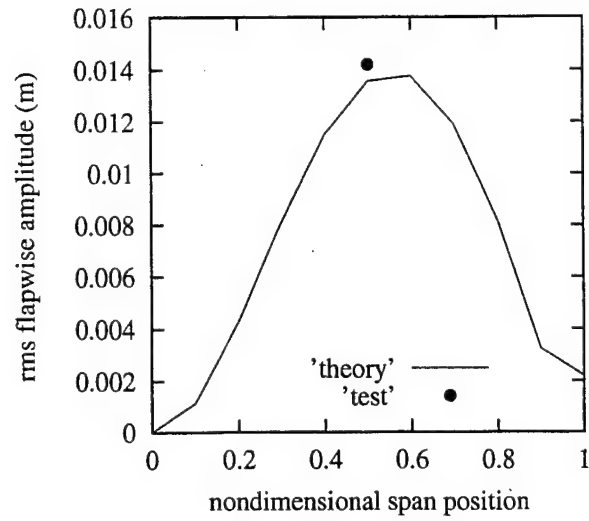


Figure 12: LCO vibration mode shape for $U=35$ m/s and $\theta_0 = 1^\circ$.

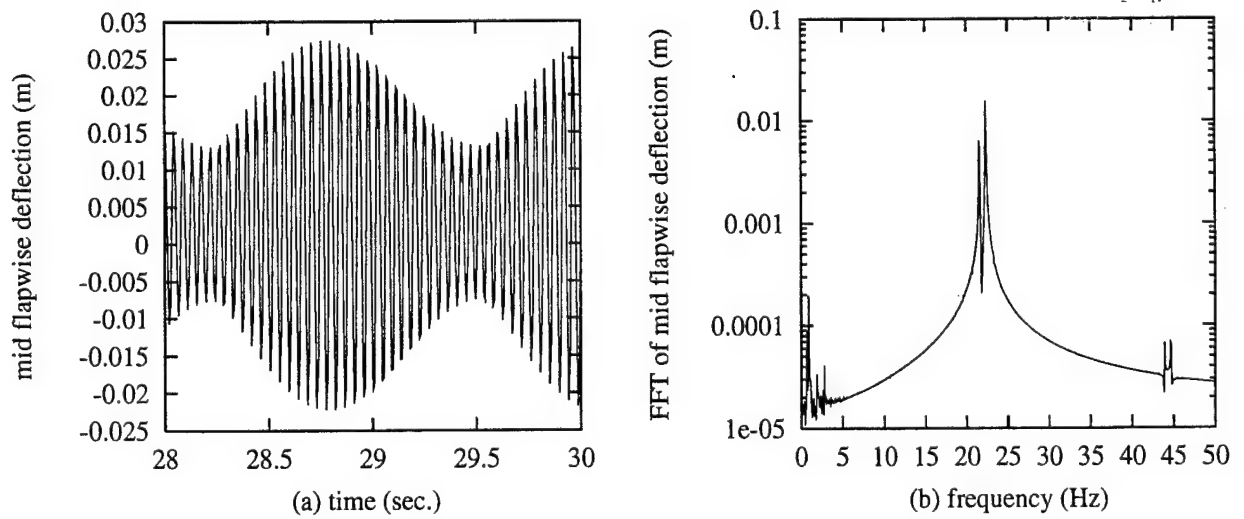


Figure 13: Time history (a) and FFT analysis (b) for $U=38$ m/s and $\theta_0 = 1^\circ$.

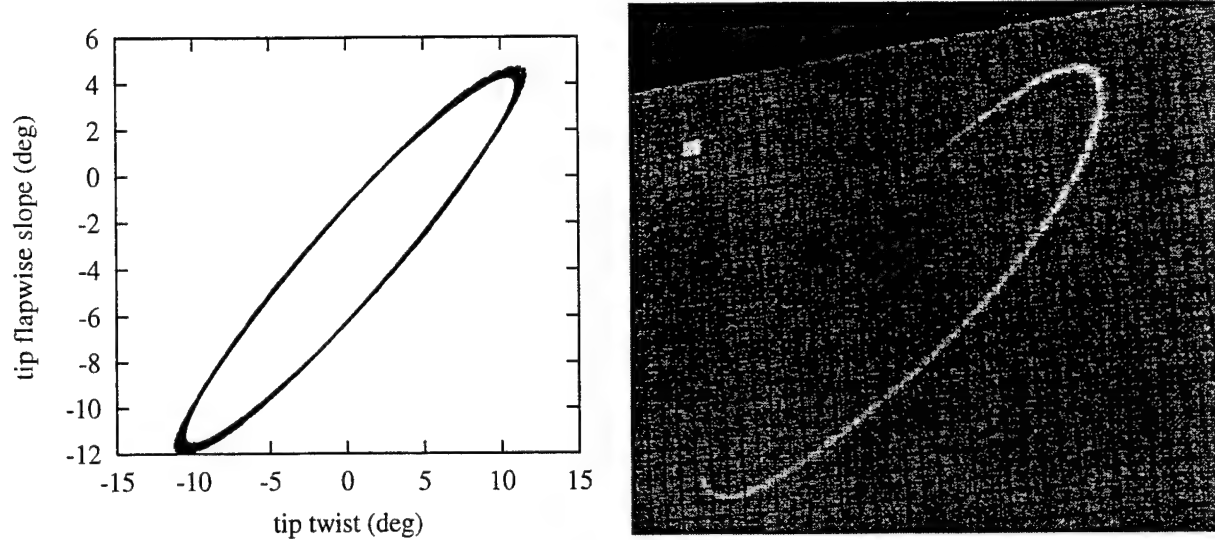


Figure 14: Phase plane plot of tip flapwise bending slope vs twist for $U=35$ m/s and $\theta_0 = 1^\circ$, (a) theory and (b) test.

for $U=35$ m/s and $\theta_0 = 1^\circ$. Figure 14(a) shows the theoretical results and 14(b) shows the test results. The grid paper is calibrated. In Figure 14(b), each square grid corresponds to one degree by one degree. The two results show the reasonably good agreement.

A typical LCO amplitude and LCO frequency vs flow velocity for $\theta_0 = 1^\circ$ and at the mid span position are shown in Figure 15(a) and (b), respectively. The theoretical and experimental amplitudes are taken as rms average values from a 50 second sampling interval. The symbols, \circ and \bullet , indicate the experimental results for increasing and decreasing flow velocity, respectively. The solid and broken lines (without symbols) indicate the theoretical results for increasing and decreasing flow velocity, respectively. The symbol, Δ , indicates the linear flutter velocity which is calculated from the perturbation eigenvalue solution. For the increasing flow velocity case, the theoretical limit cycle oscillation occurs when the flow velocity is larger than the perturbation flutter velocity and the amplitude has a jump from almost rest to a larger value. Once the onset of LCO occurs, the amplitude increases

smoothly with increasing the flow velocity. When $U > 38.6$ m/s, a numerical or possibly a physical divergence is found in the theoretical model. For the case of decreasing flow velocity, as shown by the broken line, the LCO amplitude decreases but does not exactly coincide with those for the increasing velocity case. Also there is a jump in the LCO response at $U=33.5$ m/s which is a distinctly lower velocity than that found for the increasing velocity case (i.e. $U=34.5$ m/s).

To show further details of the theoretical results, we use two "time history" figures to show the LCO responses obtained from the increasing and decreasing flow velocity processes. The results are shown in Figure 16(a) and (b) for $\theta_0 = 1^\circ$. Figure 16(a) is the result from increasing velocity and (b) is for decreasing velocity. There are eleven (11) flow velocities from $U=33$ m/s to 38 m/s with $\Delta U=0.5$ m/s considered in the calculation. At each flow velocity, the time history is computed until the system achieves a steady state LCO response. In general, it takes about 20 seconds (a time step of $\Delta t=1/2048$ seconds is used). The LCO response for the last one second is shown in Figure 16(a), i.e, the LCO response is shown in time intervals of one second for the several flow velocities. For the next flow velocity (increasing ΔU), we use initial conditions that are provided by the previous LCO state. This process is continuous in time until the flow velocity increases to $U=38$ m/s. For the decreasing velocity process, the results are shown in Figure 16(b). The process method is the same as the above. Again we see hysteresis in the response depending on whether the flow velocity is increasing or decreasing.

For the experimental measurement, we also observed two different LCO responses for increasing and decreasing flow velocity. With increasing flow velocity, we find a jump at

$U=33.5$ m/s which is similar to the theoretical results at $U=34.5$ m/s as shown by the symbol, \circ with a solid line. This jump velocity is called the experimental flutter velocity. As the flow velocity increases further, the LCO amplitude measured has a modestly larger increase than that found from theory. For model safety, the test was stopped at $U=36.5$ m/s. When the flow velocity is decreased, we find another jump at $U=32.4$ m/s as shown in Figure 16(a) and as indicated by the symbol, \bullet with a broken line. The experimental LCO amplitudes for decreasing velocity are modestly smaller than those found for increasing velocity.

The LCO frequency vs flow velocity is shown in Figure 15(b). The symbols used in this figure are the same as for Figure 15(a). As shown in Figure 15(b), the LCO frequency has a slight change as the flow velocity increases. At high velocity, the theoretical LCO has two close frequencies as discussed previously in regard to Figure 13. The theoretical/experimental agreement is reasonably good.

The theoretical/experimental results for LCO amplitude and frequency vs flow velocity for $\theta_0 = 0.25^\circ$ and at the mid span position are shown in Figure 17(a) and (b). The theoretical LCO "time histories" obtained from the increasing and decreasing flow velocity processes are shown in Figure 18(a) and (b). For the other pitch angles of attack, the experimental/theoretical results are very similar to those for $\theta_0 = 1^\circ$ and $\theta_0 = 0.25^\circ$.

A hysteresis phenomenon was found from both the theoretical prediction and experimental observation. To determine the source of the hysteresis, the theoretical calculation was repeated with the structural nonlinearity or the stall aerodynamic nonlinearity removed,

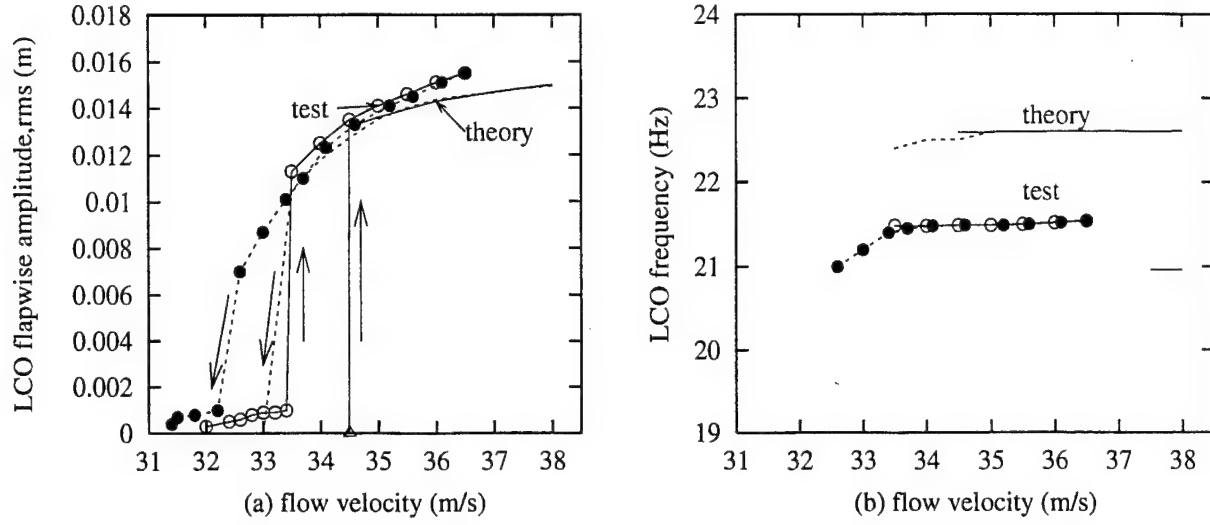


Figure 15: Mid-span LCO amplitude (a) and frequency (b) vs flow velocity for $\theta_0 = 1^\circ$.

alternatively. The results are shown in Figures 19 and 20 for $\theta_0 = 1.0^\circ$. It is found the structural nonlinearity does not lead the hysteresis and LCO as shown in Figure 19; however, the stall aerodynamic nonlinearity is responsible for this hysteresis and LCO behavior as shown in Figure 20.

CONCLUDING REMARKS

The present experimental and theoretical results provide new insights into nonlinear aeroelastic phenomena for high aspect ratio wings (with a tip slender body) that have a beam-like structural behavior. The effects of the geometric structural nonlinearity of the beam theory and aerodynamic stall on both the flutter instability boundary and the nonlinear response have been studied. The effects of the geometric structural nonlinearity depend upon the ratio of the flap and chordwise bending stiffnesses, EI_2/EI_1 . For relatively small EI_2/EI_1 , the flutter instability boundary has only a small change due to the structural nonlinearity and pre-flutter static deformation. The onset of a limit cycle oscillation is

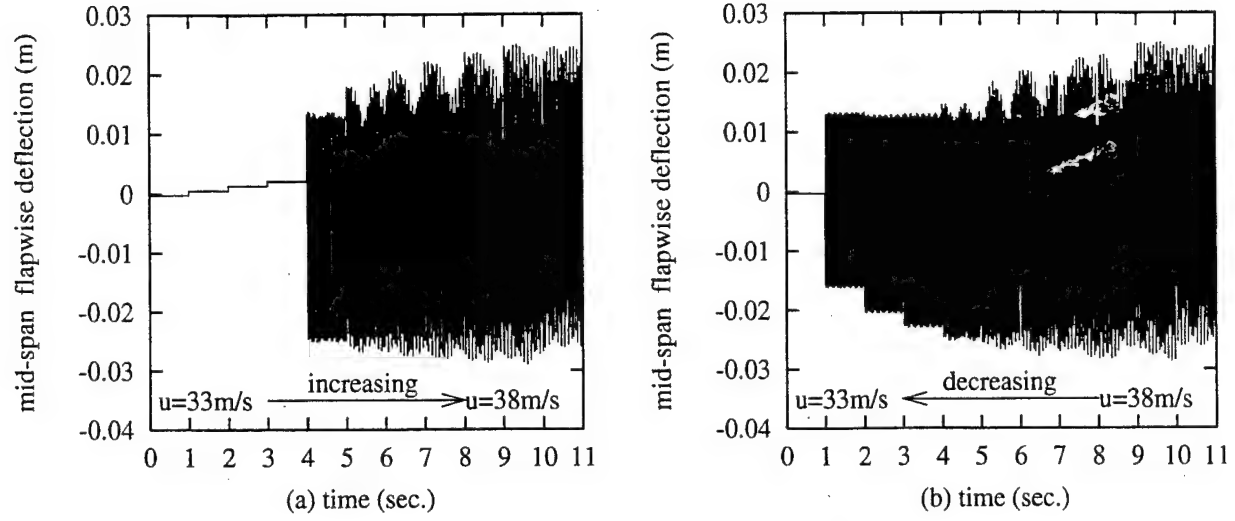


Figure 16: LCO "time history" at mid-span (a) increasing flow velocity process, and (b) decreasing process for $\theta_0 = 1^\circ$.

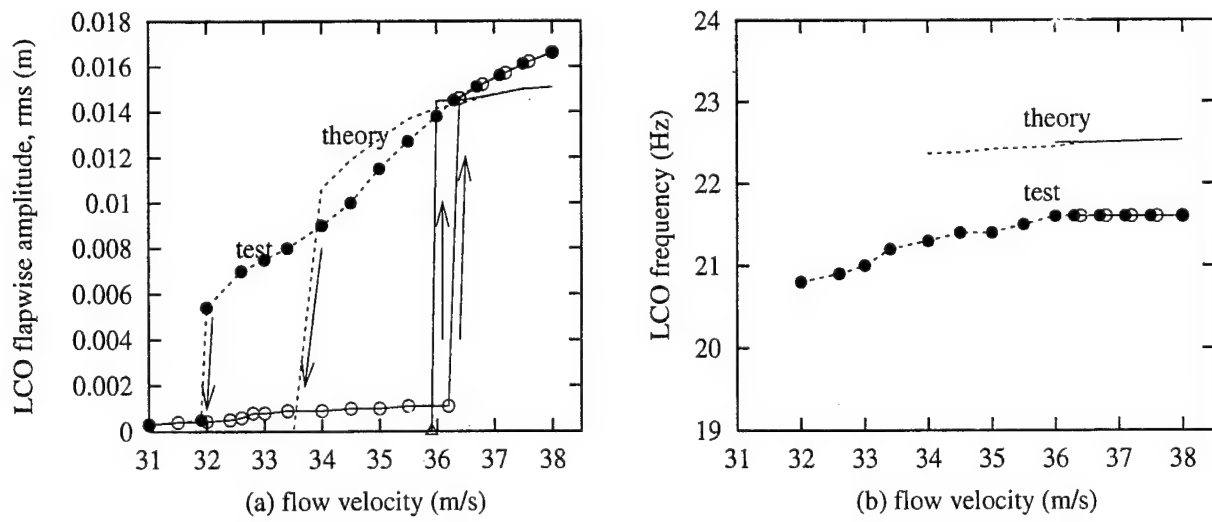


Figure 17: Mid-span LCO amplitude (a) and frequency (b) vs flow velocity for $\theta_0 = 0.25^\circ$.

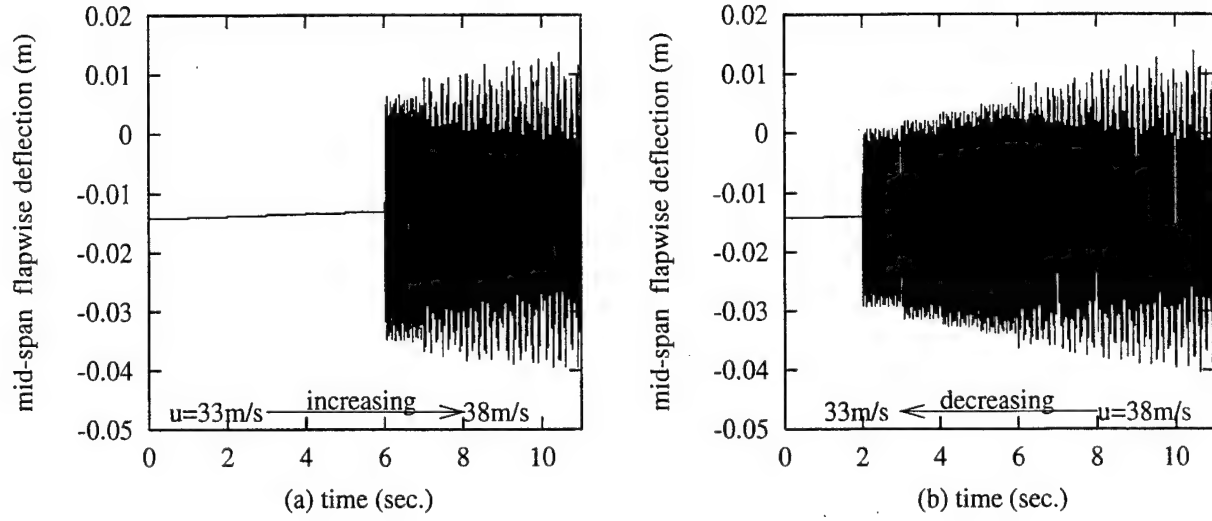


Figure 18: LCO "time history" at mid-span (a) increasing flow velocity process, and (b) decreasing process for $\theta_0 = 0.25^\circ$.

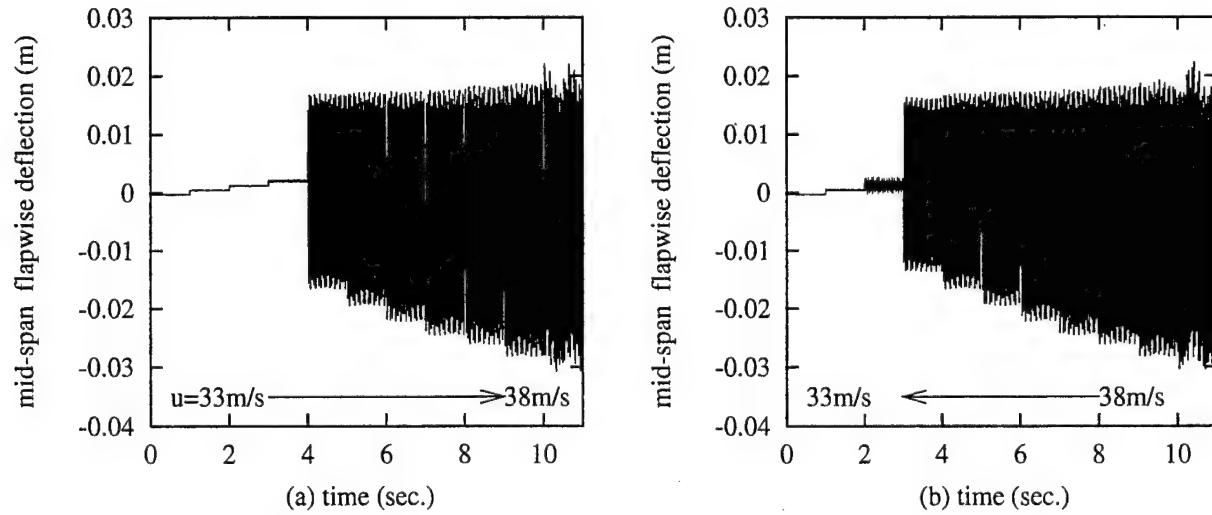


Figure 19: LCO "time history" at mid-span (a) increasing flow velocity process, and (b) decreasing process for $\theta_0 = 1^\circ$ and the structural nonlinearity removed.

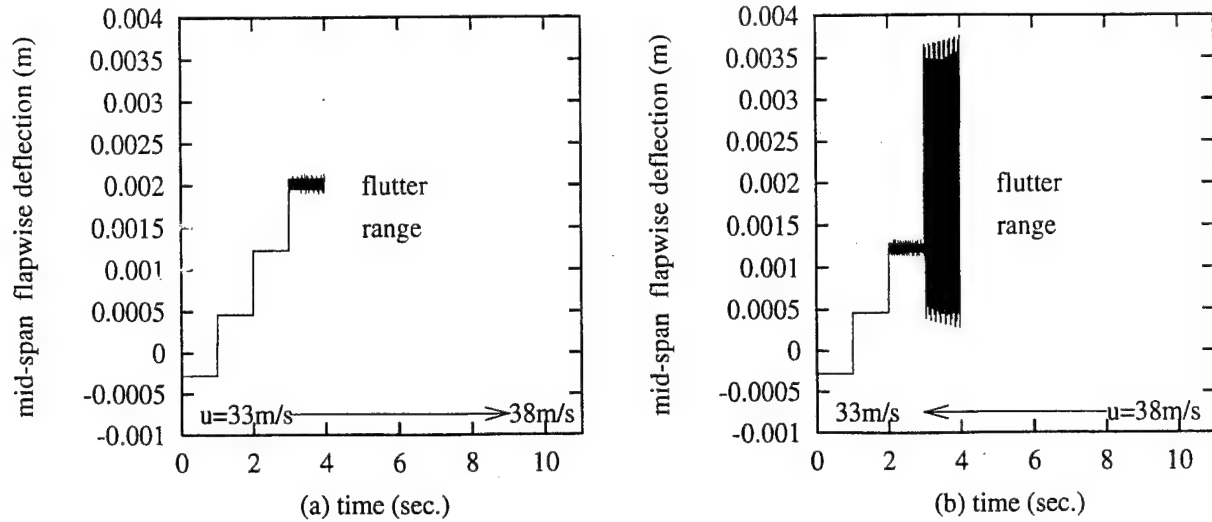


Figure 20: LCO "time history" at mid-span (a) increasing flow velocity process, and (b) decreasing process for $\theta_0 = 1^\circ$ and the stall aerodynamic nonlinearity removed.

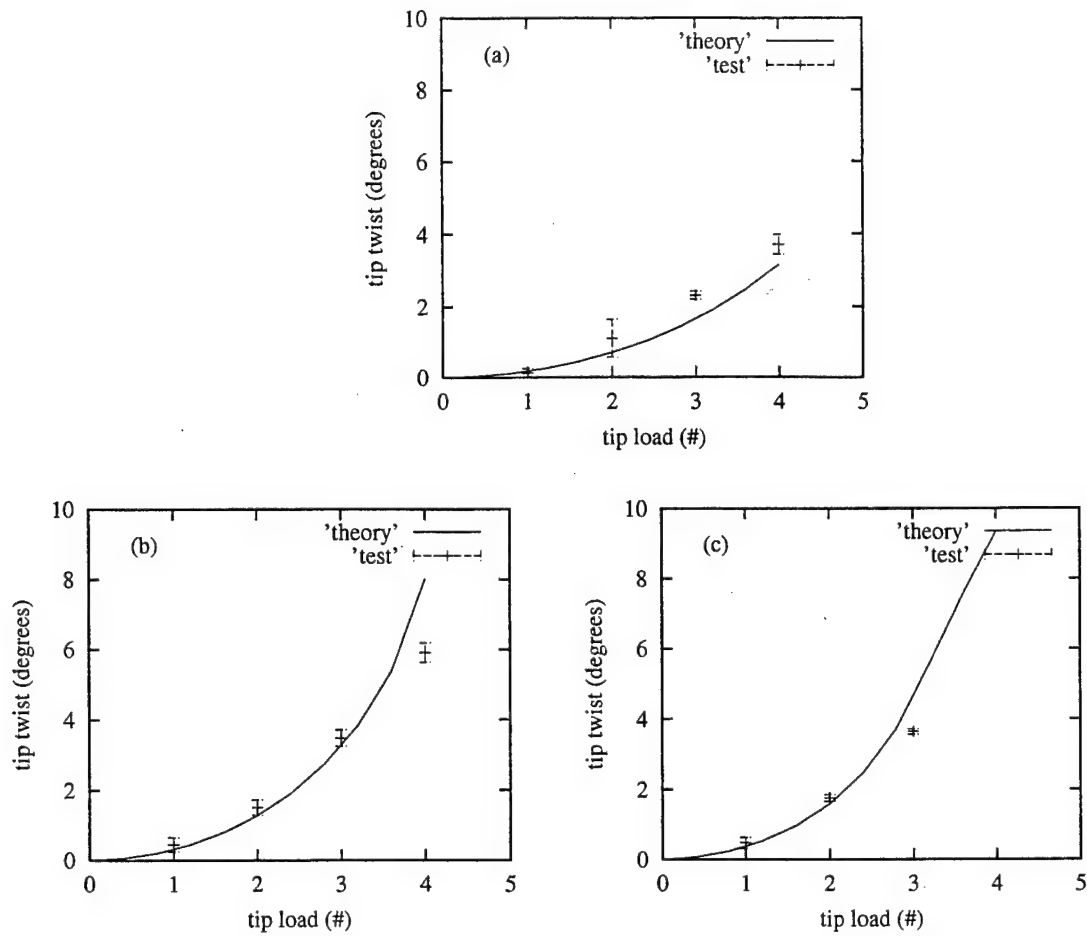
dependent upon a delicate balance between stall aerodynamics and the structural nonlinear forces [2,3]. However, the stall aerodynamics are dominant for the present experimental wing model.

ACKNOWLEDGMENTS

This work was supported by DARPA through AFOSR Grant F49620-99-1-00253, "Aeroelastic Leveraging and Control Through Adaptive Structures". under the direction of Dr. Ephraim Garcia and Dr. Dan Segalman. We would also like to thank our colleage, Dr. Robert Clark, for useful discussion of this work and graduate student, Emil Ardelean, for his assistance. All numerical calculations were done on a supercomputer, T916, in the North Carolina Supercomputing Center (NCSC).

Table 1: Experimental wing model data

Wing properties	
span (L)	0.4508 m
Chord (c)	0.0508 m
Mass per unit length	0.2351 kg/m
Mom. Inertia (50 % chord)	0.2056×10^{-4} kgm
Spanwise elastic axis	50 % chord
Center of gravity	49 % chord
Flap bending rigidity (EI_1)	0.4186 Nm^2
Chordwise bending rigidity (EI_2)	$0.1844 \times 10^2 \text{ Nm}^2$
Torsional rigidity (GJ)	0.9539 Nm^2
Flap structural modal damping (ξ_w)	0.02
Chordwise structural modal damping (ξ_v)	0.025
Torsional structural modal damping (ξ_ϕ)	0.031
Slender body properties	
Radius (R)	0.4762×10^{-2} m
Chord length (c_{SB})	0.1406 m
Mass (M)	0.0417 kg
Mom. Inertia (I_x)	$0.9753 \times 10^{-4} \text{ kgm}^2$
Mom. Inertia (I_y)	$0.3783 \times 10^{-5} \text{ kgm}^2$
Mom. Inertia (I_z)	$0.9753 \times 10^{-4} \text{ kgm}^2$



APPENDIX:

Static Deflections and Natural Frequencies Under Gravity Load,

Ref.[5]

As a further assessment of the present calculation method, a correlation study was made with the experimental data of Ref.[5]. The results are shown below in Figures 21 to 25 that correspond to the Figures 4 to 8 in Ref.[5]. For ease of comparison, the same notation is used in this Appendix as in [5]. Generally good agreement between theory and experiment is found.

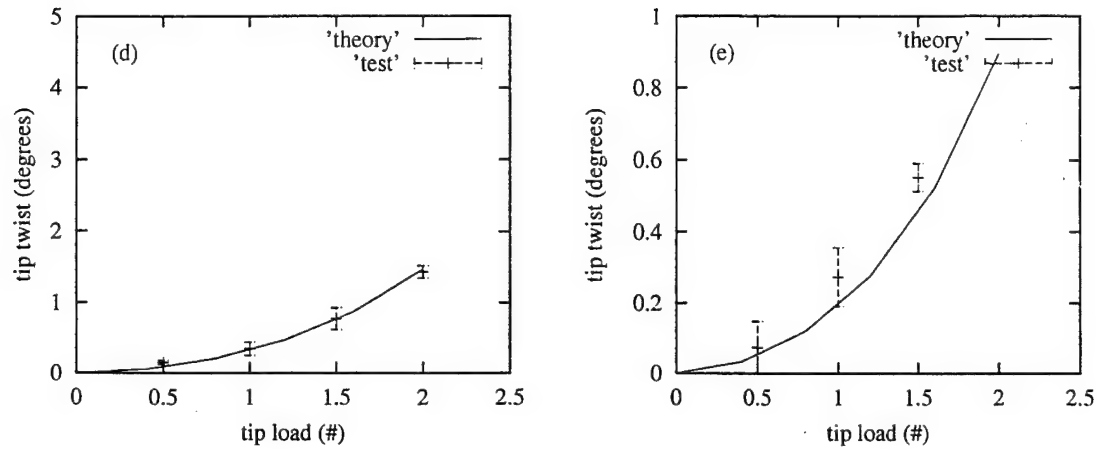


Figure 21: Static twist vs load. (a) $\theta = 15^\circ$; (b) $\theta = 30^\circ$; (c) $\theta = 45^\circ$; (d) $\theta = 60^\circ$; (e) $\theta = 75^\circ$.

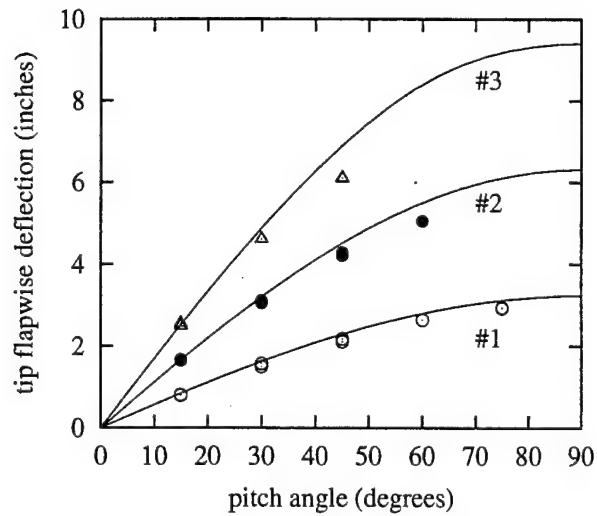


Figure 22: Static tip flapwise deflection vs pitch angle; various load. solid line, Theory. \bullet , Experiment: \triangle , $P=3$ pound; \bullet , $P=2$ pound; \circ , $P=1$ pound.

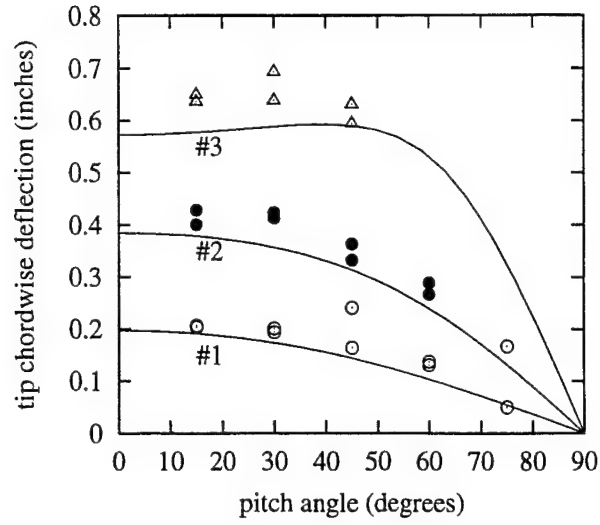


Figure 23: Static tip chordwise deflection vs pitch angle; various load. solid line, Theory. • , Experiment: \triangle , P=3 pound; \bullet , P=2 pound; \circ , P=1 pound.

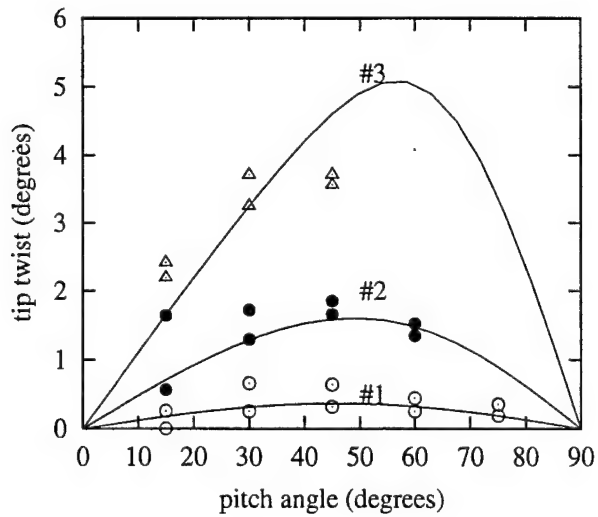


Figure 24: Static tip twist deflection vs pitch angle; various load. solid line, Theory. • , Experiment: \triangle , P=3 pound; \bullet , P=2 pound; \circ , P=1 pound.

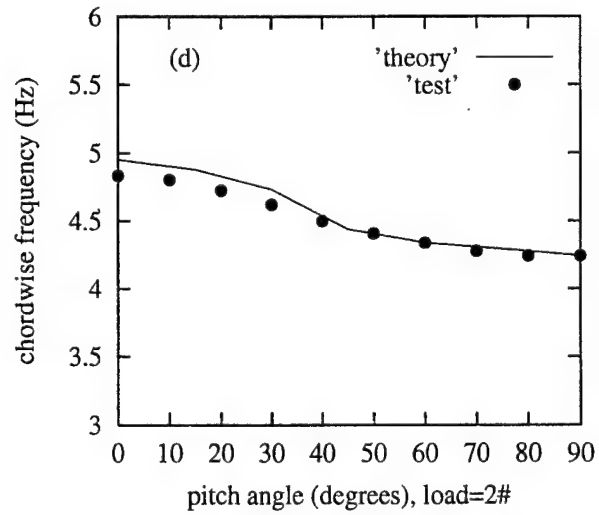
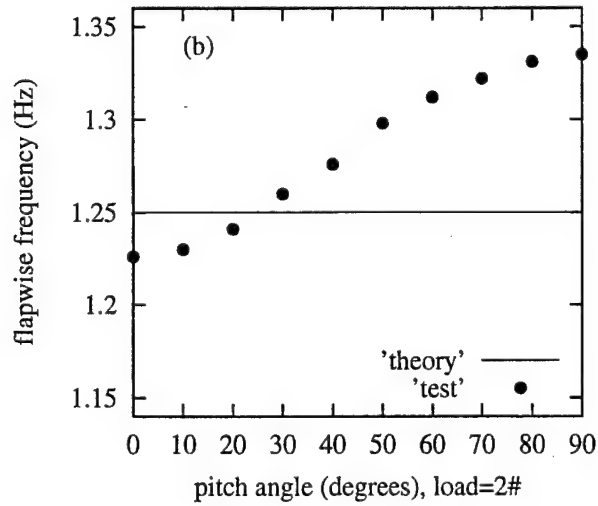
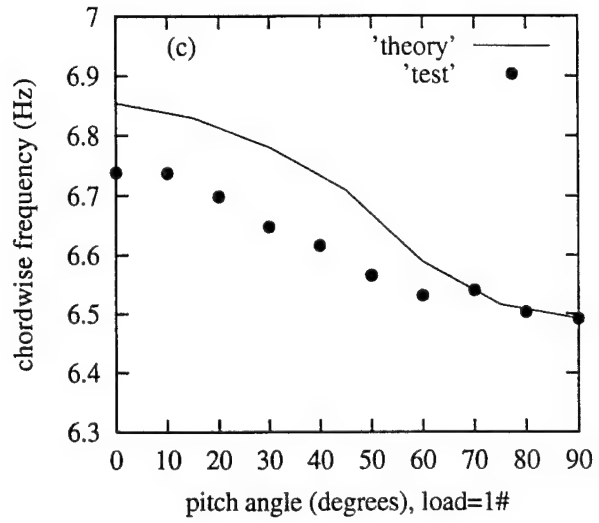
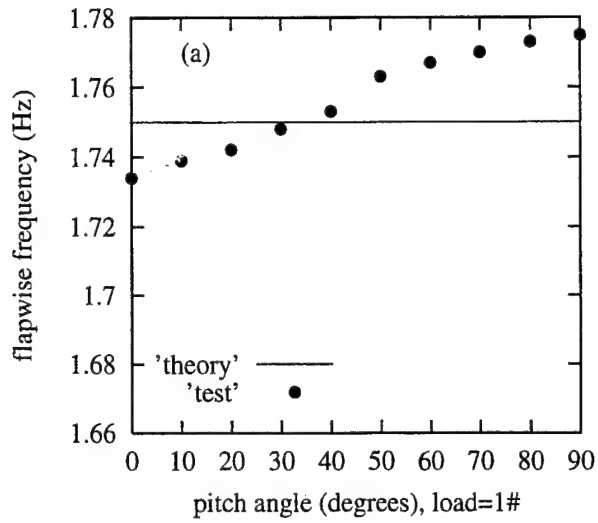


Figure 25: Flap frequency vs vs pitch angle. Solid line, theory and •, Experiment. (a) P=1 pound; (b) P=2 pound, chordwise frequency vs vs pitch angle; (c) P=1 pound, (d) P=2 pound.

References

1. Hodges, D.H., and Dowell, E.H., "Nonlinear Equations of Motion for the Elastic Bending and Torsion of Twisted Nonuniform Rotor Blades," NASA TN D-7818, 1974.
2. Patil, M. J., Hodges, D.H. and Cesnik, Carlos E. S, "Limit Cycle Oscillations in High-Aspect-Ratio Wings," AIAA Paper-99-1464.
3. Tang, D. M. and Dowell, E.H., "Effects of Geometric Structural Nonlinearity on Flutter and Limit Cycle Oscillations of High-Aspect Ratio Wings," submitted to *Journal of Fluids and Structures*, 2000.
4. Tran, C.T., and Petot, D., "Semi-Empirical Model for the Dynamic Stall of Airfoils in View to the Application to the Calculation of Responses of a Helicopter Blade in Forward Flight," *Vertica* Vol. 5, No. 1, 1981, pp. 35-53.
5. Dowell, E. H., Traybar, J. and Hodges, D.H., "An Experimental-Theoretical Correlation Study of Non-Linear bending and Torsion Deformations of A Cantilever Beam," *Journal of Sound and Vibration*, Vol.55(4), 1977, pp.533-544.
6. Patil, M. J., Hodges, D.H. and Cesnik, Carlos E. S, "Nonlinear Aeroelasticity and Flight Dynamics of High-Altitude Long-Endurance Aircraft," AIAA Paper-99-1470.
7. Patil, M. J. and Hodges, D.H., "On the Importance of Aerodynamic and Structural Geometrical Nonlinearities on Aeroelastic Behavior of High-Aspect-Ratio wings," AIAA Paper-2000-1448.

8. Minguet, Pierre, and Dugundji, John,"Experiments and Analysis for Composite Blades Under Large Deflections, Part II: Dynamic Behavior," *AIAA Journal* , (1990), Vol.28, pp. 1580-1588.

9. Bisplinghoff, R.L., Ashley, H. and Halfman, R.L.,"Aeroelasticity," Addison-Wesley, 1955.

AN ADAPTIVE AEROELASTIC WING WITH LEADING AND TRAILING EDGE CONTROL SURFACES

Earl H. Dowell, ¹ Donald B. Bliss ² and Robert L. Clark ³

Duke University, Durham, North Carolina 27708-0300

ABSTRACT

It is well known that the effectiveness of a trailing edge control surface can be substantially diminished due to the elastic twist of an airfoil or rolling wing. This aeroelastic phenomenon is known by the name of control surface reversal when the lift or rolling rate vanishes at a sufficiently large ratio of flow dynamic pressure to airfoil or wing stiffness.

However a leading edge control surface can be used to counteract control surface "reversal" and indeed, in principle, a leading edge control surface can entirely cancel the tendency of the trailing edge control surface to undergo reversal. Moreover analysis shows that by using a simple adaptive control strategy one can use a combination positive and negative control surface rotations to maintain lift and rolling effectiveness and minimize control surface rotations.

The beneficial effects of leading edge control surfaces on control surface reversal are known to practioners. However the present simple model makes these especially transparent and suggests an advantageous adaptive strategy using a combination of leading and trailing edge control surfaces.

¹J. A. Jones Professor, Department of Mechanical Engineering and Materials Science and Director of the Center for Nonlinear and Complex Systems. Dean Emeritus, Pratt School of Engineering.

²Associate Professor, Department of Mechanical Engineering and Materials Science, Pratt School of Engineering.

³Professor of Mechanical Engineering and Materials Science and Senior Associate Dean, Pratt School of Engineering.

Ref 2
Submitted
to AIAA
Journal

INTRODUCTION

Control surface reversal due to unfavorable aeroelastic effects is one of the classical phenomena of static aeroelasticity. It is treated in textbooks [1,2] and standard courses on aeroelasticity. Here this well known phenomenon is re-considered in the light of counter-acting the unfavorable aeroelastic effect associated with trailing edge control surfaces by a favorable effect of a leading edge control surface. By adaptively changing the ratio of leading edge control surface rotations, a particular advantageous result may be obtained.

To illustrate the concept and fundamental physical phenomena, two simple models of (1) an airfoil and (2) a rolling wing are considered. Inter alia, an interesting result for the divergence of a rolling wing is also highlighted.

The Active Flexible Wing and the Active Aeroelastic Wing programs have been pursued vigorously and reported widely. See, for example, Ref. [3-10]. A number of important insights and concepts have been highlighted in this literature concerning the effectiveness of multiple control surfaces. These include most notably leading edge control surfaces to offset the traditional loss of effectiveness of trailing edge control surfaces due to unfavorable aeroelastic wing twist. Noll and Eastep [3] present a cogent overview and organized an issue of the Journal of Aircraft on the Active Flexible Wing program. The most directly relevant paper in that issue was by Woods- Vedelee, Potozky and Hoadley[4] wherein they discussed various possible control laws and the means to obtain them to optimize (minimize) roll maneuver loads using active controls.

Later work by Anderson, Forster, Kolonay and Eastep [5] gave deeper insights into the favorable synergy that can be created by a combination of leading and trailing edge controls. In their work they noted that the unfavorable aeroelastic twist that can lead to trailing edge control surface reversal can be offset by a leading edge control surface. Moreover, the trailing edge control surface reversal can be eliminated and a constant roll authority maintained over a wide range of flight dynamic pressures by an appropriate combination of leading and trailing edge control surface deflections. In their approach (1) the trailing edge control surface rotation is tail down (for rolling to the left) at dynamic pressures below the classical reversal dynamic pressure (for only a trailing edge control surface in the absence of leading edge control), (2) then the trailing edge control surface rotation is set to zero at the dynamic pressure that corresponds to the classical reversal dynamic pressure and (3) finally the trailing edge control surface is rotated tail up at yet higher dynamic pressures.

The leading edge control also varies with dynamic pressure, but is always nose up with a maximum near the aforementioned classical reversal dynamic pressure.

These theoretical trends are consistent with experimental data from a cantilevered wing model of the Agile Falcon [10].

This is a creative and inventive approach. However as will be discussed below, it appears one can increase the rolling rate even beyond that for a rigid wing by an appropriately chosen combination of leading and trailing edge control surface deflections. Moreover, and as will be seen, the torsional stiffness need not be compromised based upon control surface reversal considerations.

More recent work on the Active Aeroelastic Wing concept has dealt with improvements in design optimization methodologies, reduction of drag, and an adaptive change in torsional stiffness to allow both pre- and post-classical reversal operation of an Active Aeroelastic Wing [6-9]. As will be seen, the same conceptual benefit that can be obtained by using a torsional stiffness change can also be realized by using an adaptive aeroelastic wing with the gearing ratio between leading and trailing edge control surfaces programmed to change with flight dynamic pressure.

The adaptive control law to achieve maximum rolling performance is straightforward. In the pre-reversal regime (defined by the classical reversal for a trailing edge control surface only [no leading edge control]), the trailing edge control surface should be at its maximum trailing edge down and the leading edge control should be at its maximum nose up. Such a control law minimizes the loss of roll rate due to aeroelastic effects and indeed if the leading edge control surface rotation is sufficiently large, then the roll rate of the aeroelastic wing can exceed that of a rigid wing. However, at a certain flight dynamic pressure which can be calculated from an appropriate aeroelastic analysis as given in the present paper or determined from a wind tunnel test of an aeroelastic model, it will be advantageous to change the sign of trailing edge control while maintaining the leading and trailing edge control deflections at their maximum values. Note that in this scheme the magnitude of the leading and trailing edge controls are always maintained at their maximum values at any dynamic pressure to maximize the roll rate and only the sign of the trailing edge control surface rotation is changed at a selected and optimized value of dynamic pressure. One can use similar considerations to take into account constraints on wing twist or structural loads as they may effect the adaptive control scheme to maximize roll rate. Indeed one could also

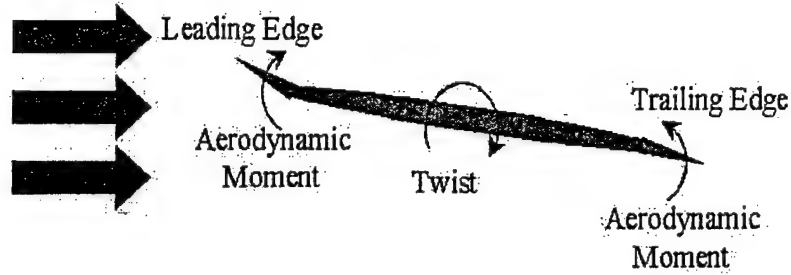


Figure 1: Schematic diagram of control surfaces and resulting moments.

determine the adaptive control law that would minimize wing twist for a given roll rate or maximum control surface deflection.

Before turning to the aeroelastic analysis, a brief discussion of control surface actuation is presented.

Implementation of an adaptive aeroelastic wing with leading and trailing edge control surfaces requires aeroservoelastic control. Current systems include hydraulics as well as electromechanical drives incorporating DC motors with appropriate gearing systems required to achieve the desired control surface stroke. For uninhabited aerial vehicles (UAVs) and uninhabited combat aerial vehicles (UCAVs), methods of implementing continuous (spatially deforming) as opposed to discrete control surfaces are desired to reduce radar signature and configure control surface actuation as a function of mission requirements. As shown in the results presented in this paper, it is possible to maintain the rolling effectiveness as a function of dynamic pressure through the use of a leading edge control surface. A schematic diagram of the conceptual control surfaces is provided in Figure 1. As illustrated, the leading edge control surface serves to provide an aerodynamic moment on the wing that counteracts the

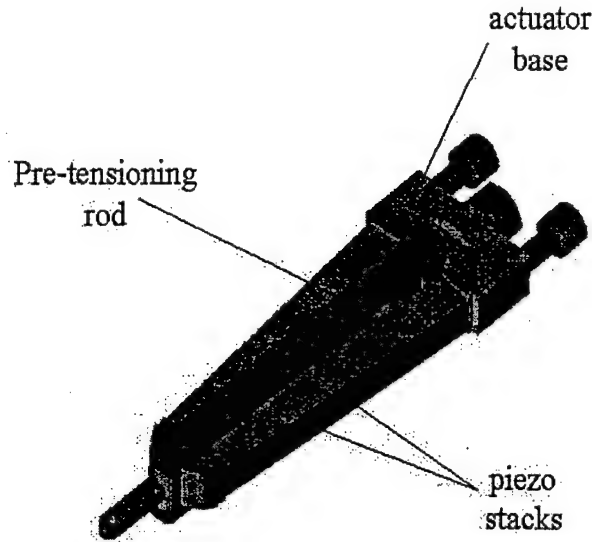


Figure 2: Schematic of V-stack actuator.

adverse effect of the aerodynamic moment introduced by the trailing edge control surface when used to increase lift. If the overall deflection of the leading edge is constrained to some finite value (a requirement for practical implementation), then the trailing edge control surface can be reversed at a point prior to compromising the rolling effectiveness of the vehicle. It is then possible to reverse the leading or trailing edge control surface at a given dynamic pressure and maneuver the vehicle beyond the conventional control surface reversal condition.

The dynamic control of the leading and trailing edge control surfaces, whether they be discrete, as illustrated in the two-dimensional schematic of Figure 1, or continuously distributed over the span of the wing, must be synchronously controlled. New actuation technologies are currently under development for high-bandwidth actuation, leveraging high energy density materials such as piezoceramics. Two such actuation technologies include the X-frame actuator developed at MIT [11] and the V-stack actuator developed at Duke University [12]. Stroke amplification on the order of a factor of 10 can be achieved, and the actuators can be impedance matched for the desired application of dynamic load. The V-stack actuator (Figure 2) can be readily modified for impedance matching applications

by simply removing the actuator base and modifying the separation distance between the two piezoelectric stacks by increasing or decreasing the dimension of the actuator base. The current prototype actuator has a total mass of 0.65 kg, produces a force of 125 pounds with a tip deflection of ± 1.5 mm, a frequency response extending to approximately 600 Hz, and a mass efficiency of approximately 15%.

Such actuation devices can be integrated as a function of span to control "segments" of a continuously distributed control surface, both on the leading and trailing edge of the wing. Such actuation technologies can be used for dynamics associated with aircraft maneuvers as well as aeroelastic control.

1. An Adaptive Aeroelastic Typical Section Airfoil with Leading and Trailing Edge Control Surfaces

1.1 Equations of Equilibrium

The equation of torsional equilibrium about the elastic axis is as follows [1,2]. It expresses the balance of moments about the elastic axis due to the elastic spring and the aerodynamic forces.

$$K_{\alpha}\alpha = Le + M_{AC} \quad (1)$$

or

$$K_{\alpha}\alpha = qc^2[C_L\frac{e}{c} + C_{MAC}] \quad (2)$$

Now define,

$$\lambda \equiv qc^2/K_{\alpha} \quad (3)$$

a non-dimensional ratio of aerodynamic dynamic pressure, q , to torsional spring stiffness, K_{α} . e is the distance from the aerodynamic center (of lift) to the elastic axis taken as positive aft. α is the elastic twist and c the airfoil chord.

Then Eq.(2) becomes

$$\alpha = \lambda[C_L\frac{e}{c} + C_{MAC}] \quad (4)$$

From aerodynamic theory [1,2], the lift and moment about the aerodynamic center may be expressed as follows.

$$C_L = C_{L\alpha}\alpha + C_{L\eta_{te}}\eta_{te} + C_{L\eta_{le}}\eta_{le} \quad (5)$$

$$C_{MAC} = C_{MAC\eta_{te}}\eta_{te} + C_{MAC\eta_{le}}\eta_{le} \quad (6)$$

where η_{te}, η_{le} are the trailing and leading edge control surface angular rotations and $C_{L\alpha}$, etc. are known (linear theory) aerodynamic coefficients that depend parametrically on Mach number and the wing and control surface planform geometries.

1.2 Reversal

By definition, $L = 0$ at reversal. Now using Eqs.(4) in (6), one may determine the corresponding torsional elastic twist, α_R , setting $L = 0$, of course.

$$\alpha_R = \lambda_R [C_{MAC\eta_{te}}\eta_{te} + C_{MAC\eta_{le}}\eta_{le}] \quad (7)$$

or

$$\alpha_R = \lambda_R [C_{MAC\eta_{te}} + r C_{MAC\eta_{le}}] \eta_{te} \quad (8)$$

where $r \equiv \eta_{le}/\eta_{te}$, is the ratio of leading to trailing edge control surface rotations. $\lambda_R \equiv$ reversal dynamic pressure.

Now from Eq.(5),

$$\alpha_R = \frac{-[C_{L\eta_{te}} + r C_{L\eta_{le}}]\eta_{te}}{C_{L\alpha}} \quad (9)$$

Dividing Eq.(8) by Eq.(9) and re-arranging, one has the following expression for λ_R .

$$\lambda_R = \frac{-[C_{L\eta_{te}} + r C_{L\eta_{le}}]}{C_{L\alpha}[C_{MAC\eta_{te}} + r C_{MAC\eta_{le}}]} \quad (10)$$

Note that λ_R does not depend upon e/c . Also for $r = 0$, one retrieves the classical reversal result for no leading edge control surface [1,2]. Finally note that $\lambda_R \rightarrow \infty$, when

$$r = -C_{MAC\eta_{te}}/C_{MAC\eta_{le}} \quad (11)$$

1.3 Divergence

This is the static instability for which $\alpha \rightarrow \infty$ for finite η_{te} or η_{le} , or alternatively for which α is finite when $\eta_{te} = \eta_{le} = 0$. Thus one may set $\eta_{te} = \eta_{le} = 0$ to determine λ_D , the divergence dynamic pressure. Using Eqs.(4) and (5),

$$\alpha_D = \lambda_D C_{L\alpha} \alpha_D \frac{e}{c}$$

or

$$\lambda_D = \frac{1}{C_{L\alpha} \frac{e}{c}} \quad \text{for} \quad \alpha_D \neq 0 \quad (12)$$

Note λ_D does not depend on η_{te} , η_{le} or their associated aerodynamic coefficients. Of course, in this linear model it does not depend on α_D either.

1.4 Lift Effectiveness (for general λ)

Now one can determine C_L taking into account twist, α , of the airfoil and the control surface rotations, η_{te} and η_{le} for any λ . First solve for α from Eq.(4), using Eqs.(5),(6) and (11),

$$\alpha = \frac{\lambda}{1 - \lambda/\lambda_D} \left\{ \frac{e}{c} [C_{L\eta_{te}} + r C_{L\eta_{le}}] + [C_{MAC\eta_{te}} + r C_{MAC\eta_{le}}] \right\} \eta_{te} \quad (13)$$

Also Eq.(5) may be re-written as

$$C_L = [C_{L\alpha} \left(\frac{\alpha}{\eta_{te}} \right) + C_{L\eta_{te}} + r C_{L\eta_{le}}] \eta_{te} \quad (14)$$

Using Eqs.(13) in (14) and the definitions of λ_R given by Eq.(10) and λ_D given by (12), one determines that

$$\frac{C_L}{[C_{L\eta_{te}} + r C_{L\eta_{le}}] \eta_{te}} = \frac{1 - \lambda/\lambda_R}{1 - \lambda/\lambda_D} \quad (15)$$

The left-hand side of Eq.(15) is the ratio of lift for the aeroelastic airfoil to that for a rigid airfoil. Note again that for $r = 0$, one retrieves the classical result for no leading edge control surface i.e a trailing edge control surface only. Of course, when $\lambda \rightarrow 0$ or $\lambda \ll \lambda_R$ and λ_D , the right hand side of Eq.(15) approaches unity.

Finally, note that when $\lambda_R = \lambda_D$, the aeroelastic airfoil lift is equal to the rigid airfoil lift for all λ . See Eq.(15). However, note from Eq.(13) that $\alpha \rightarrow \infty$ as $\lambda = \lambda_D$ even when $\lambda_R = \lambda_D$. Thus for the enhancement of lift effectiveness to be useful, one requires that $\lambda < \lambda_D$.

It is thus of interest to solve for the value of r such that $\lambda_R = \lambda_D$. From Eqs.(10) and (12),

$$r|_{\lambda_R=\lambda_D} = - \frac{[C_{L\eta_{te}} + \lambda_D C_{L\alpha} C_{MAC\eta_{te}}]}{[C_{L\eta_{le}} + \lambda_D C_{L\alpha} C_{MAC\eta_{le}}]} \quad (16)$$

where $\lambda_D \equiv \frac{1}{C_{L\alpha} \frac{e}{c}}$.

One can use Eq.(16) to find a λ_D or e/c such that r has a desired value including $r = 0$. Of course, the smaller the desired r the smaller the resulting $\lambda_D (= \lambda_R)$, so a design optimum will exist that balances a sufficiently large λ_D and not too large a value of r .

1.5 Numerical Results

Typical values of the aerodynamic coefficients are the following [13]. Control surface chords of 10% and 20% of total airfoil chord are considered for a thin airfoil at $M = 0$. Results for $M \neq 0$ are readily obtained using the Prandtl-Glauert transformation.

Coefficients	20%	10%
$C_{MAC\eta_{te}}$	-0.64	-0.54
$C_{MAC\eta_{le}}$	0.16	0.06
$C_{L\eta_{te}}$	3.45	2.49
$C_{L\eta_{le}}$	0.255	0.087

Of course, the leading and trailing edge control surface chords may be chosen to be different in an optimization design study. Here they are chosen to be the same.

1.5.1 Reversal results:

From Eq.(10) we determine the following.

τ	λ_R	λ_R
	20%	10%
0	0.86	0.73
1	1.23	0.86
2	1.97	1.01
3	4.19	1.22
4	∞	-
9	-	∞
-1	0.64	0.64
-2	0.49	0.56

1.5.2 Divergence results:

From Eq.(12), one determine the following.

e/c	λ_D
0	∞
0.05	3.18
0.1	1.59

1.5.3 Lift effectiveness results:

Using Eqs.(10),(12) and (15) the desired results may be obtained (only the case of 20% control surface chords is considered). These are shown in Figure 1 for $e/c = 0$ and 0.05. Of course, for $e/c \rightarrow 0$, $\lambda_D \rightarrow \infty$ and the variation of lift effectiveness with λ is linear. See Eq.(15).

For any e/c , the results for $r = 0$ are those for no leading edge control surface. When $r = 2$, for example, the leading edge control surface rotation is twice that of the trailing edge.

Consider first the results for $e/c = 0$. In Figure 3. it is seen that the lift effectiveness is increased substantially when $r > 0$. Note the reversal dynamic pressure is increased by over 100% by increasing r from 0 to 2. Note, in particular, that at $\lambda = 0.86$ (corresponding to reversal for $r = 0$), the lift effectiveness is greater than 50% for $r = 2$. Finally note that above a certain λ (of order 1), it will be advantageous to change the sign of r (see the results for $r = -2$) or the direction of the leading edge control surface rotation. Indeed by changing the sign of r above a certain λ one may achieve a lift effectiveness greater than that for a rigid wing.

Thus for small λ one might advantageously select $r > 0$ and operate in the pre-reversal regime and for larger λ one might select $r < 0$ and operate in the post-reversal regime.

Also for sufficiently large positive r ($r \geq 4$), the lift effectiveness may exceed that of a rigid wing. However for various practical reasons, such large values of r may be difficult to use in practice.

Now consider the results for $e/c = 0.05$. As expected, λ_R is the same as that for $e/c = 0$ (for any r). Recall Eq.(10). Moreover, as may be expected from an examination of Eq.(15), the lift effectiveness for $e/c = 0.05$ (or any $e/c > 0$) is always greater (in magnitude) than that for $\lambda \neq \lambda_R$. Of course, the lift effectiveness becomes very large as $\lambda \rightarrow \lambda_D$, i.e. $C_L \rightarrow -\infty$ (for $r < 4$) or $C_L \rightarrow +\infty$ (for $r > 4$). On the other hand, when $e/c < 0$,

$\lambda_D < 0$ and the lift effectiveness will be less than that for $e/c = 0$ for any λ other than $\lambda = \lambda_R$. For $e/c < 0$, the lift effectiveness as $\lambda \rightarrow \infty$ approaches λ_D/λ_R . [Recall $\lambda_D < 0$ for $e/c < 0$.]

Finally note that from Eq.(16), when $r = 2.70$, $\lambda_D = \lambda_R$, and the lift effectiveness is unity for all λ .

1.5.4 *Twist angle results:*

For too large a twist angle, the structural integrity of the airfoil or wing may be a concern. For simplicity set $e/c = 0$, and use Eq.(13) to determine an estimate for α .

$$\alpha|_{e/c=0} = \lambda[C_{MAC\eta_{te}} + rC_{MAC\eta_{le}}]\eta_{te} \quad (17)$$

For typical values of $\lambda \sim 0(1)$ and C_{MAC} , one sees that $\alpha|_{e/c=0}$ is on the order of η_{te} or less. Clearly in a practical design study, there must be a compromise between competing objectives. However the twist values seem reasonable for $r > 0$. For $r < 0$, the twist values will be larger, but still not beyond a plausible range of values.

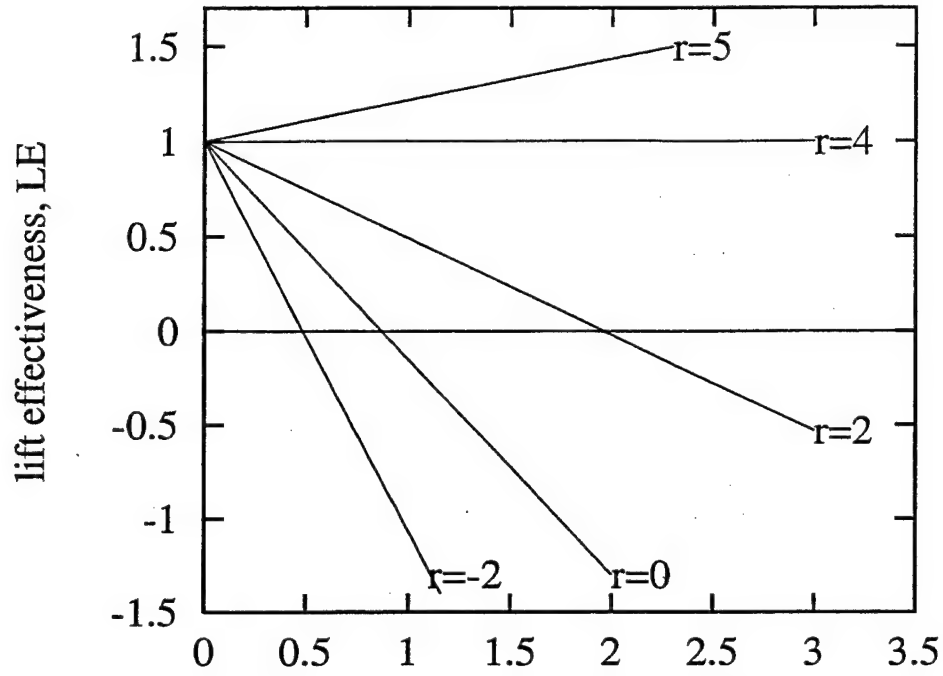
Note that for $r = 4$, the leading and trailing edge moments about the elastic axis balance and $\alpha = 0$. However for such a large r , nonlinear aerodynamic effects (not modeled here) may be important.

Of course, for $e/c > 0$ and $\lambda_D > 0$, the twist will tend to infinity as $\lambda \rightarrow \lambda_D$. Recall Eq.(13). Thus the estimate of Eq.(17) is valid for small e/c and/or $\lambda < \lambda_D$, say $e/c < 0.1$ and $\lambda/\lambda_D < 0.5$.

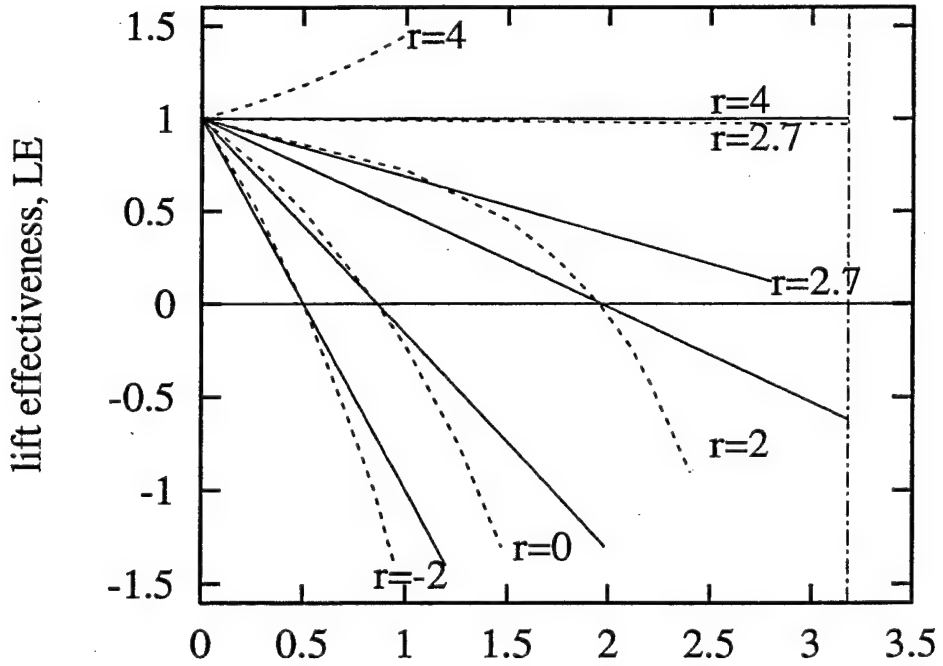
One can, of course, determine α for any e/c , r or λ from Eqs.(13).

2. An Adaptive Aeroelastic Rolling Wing with Leading and Trailing Edge Control Surfaces

Now consider a straight rectangular wing with leading and trailing edge control surfaces that are full span. A more complex geometric planform can be treated using modern computational models [14].



(a) dynamic pressure: $e/c=0$



(b) dynamic pressure: $e/c=0$ and 0.05

Figure 3: Lift effectiveness, $LE = \frac{C_L}{C_{L,RIGID}}$, vs dynamic pressure, λ ; (a) for $e/c \equiv 0$, (b) for $e/c \equiv 0$ and 0.05 . The solid line is for $e/c = 0$ and the broken line is for $e/c = 0.05$. The dash-dot line at $\lambda = 3.18 = \lambda_D$ is for $e/c = 0.05$ (Note: $\lambda_D \rightarrow \infty$ as $e/c \rightarrow 0$).

As will seen, the results for a rolling wing, including reversal, divergence and rolling effectiveness are entirely analogous to those found in the typical section airfoil model. One interesting sidelight of the study is the finding that including the rolling degree of freedom greatly increases the divergence dynamic pressure. In retrospect, at least, this is not surprising as the rolling moment due to lift must be zero for a constant or steady roll rate. Hence the lift due rolling rate tends to cancel the lift due to wing twist and this substantially alleviates the tendency of the aeroelastic wing to diverge as the dynamic pressure increases.

2.1 Torsional Equation of Equilibrium [1,2]

$$\frac{d}{dy}(GJ\frac{d\alpha}{dy}) + M_y = 0 \quad (18)$$

2.2 Aerodynamic Model

$$M_y = eL + M_{AC} \quad (19)$$

$$L = qcC_L \quad (20)$$

$$C_L = C_{L\alpha}(\alpha - \frac{py}{U}) + C_{L\eta te}\eta_{te} + C_{L\eta le}\eta_{le} \quad (21)$$

$$M_{AC} = qc^2 C_{MAC} \quad (22)$$

$$C_{MAC} = C_{MAC\eta te}\eta_{te} + C_{MAC\eta le}\eta_{le} \quad (23)$$

Thus Eq.(19)-(23) give

$$M_y = qc^2 \{ [C_{MAC\eta te}\eta_{te} + C_{MAC\eta le}\eta_{le}] + \frac{e}{c} [C_{L\alpha}(\alpha - \frac{py}{U}) + C_{L\eta te}\eta_{te} + C_{L\eta le}\eta_{le}] \} \quad (24)$$

where p is the rolling rate (angular velocity) and y is the spanwise spatial coordinate.

2.3 Rigid Body Rolling Equations of Equilibrium

$$\int_0^l Lydy = 0 \quad (25)$$

or

$$\int_0^l [C_{L\alpha}(\alpha - \frac{py}{U}) + C_{L\eta te}\eta_{te} + C_{L\eta le}\eta_{le}] y dy = 0 \quad (26)$$

2.4 Typical Values of the Aerodynamic Coefficients

The aerodynamic coefficients are chosen to be the same as those for the typical section airfoil, i.e. a "strip theory" aerodynamic model is employed. Only control surfaces of 20% chord are considered as an example.

$$C_{L\alpha} = 2\pi$$

$$C_{L\eta_{te}} = 3.45$$

$$C_{L\eta_{le}} = 0.255$$

$$C_{MAC\eta_{te}} = -0.64$$

$$C_{MAC\eta_{le}} = 0.16$$

2.5 Solution Procedure

Assume a single structural twist mode [1,2].

$$\alpha = \bar{\alpha} \sin \frac{\pi y}{2l} \quad (27)$$

Substituting Eq.(27) into (18) and using (24), multiplying through by $\sin \frac{\pi y}{2l}$ and integrating over the wing span, $\int \dots dy$ gives the following Galerkin mathematical model.

$$\begin{aligned} &[-(\frac{\pi}{2})^2 + \lambda C_{L\alpha} \frac{e}{c}] \bar{\alpha} + \lambda \{ [C_{MAC\eta_{te}} \eta_{te} + C_{MAC\eta_{le}} \eta_{le}] \\ &+ \frac{e}{c} [C_{L\eta_{te}} \eta_{te} + C_{L\eta_{le}} \eta_{le}] \} \frac{4}{\pi} - \lambda C_{L\alpha} \frac{e}{c} \frac{8}{\pi^2} \frac{pl}{U} = 0 \end{aligned} \quad (28)$$

Note: For simplicity, we have taken the control surfaces to be full span and as indicated use "strip theory" aerodynamics. Refinements to include partial span control surfaces and three-dimensional aerodynamics will not change the essential physical model, though they will clearly be important for design studies.

Also define,

$$\lambda \equiv \frac{qc^2 l^2}{GJ}$$

Substituting Eq.(27) into (26) gives

$$C_{L\alpha} (\frac{12}{\pi^2}) \bar{\alpha} - C_{L\alpha} (\frac{pl}{U}) + \frac{3}{2} [C_{L\eta_{te}} \eta_{te} + C_{L\eta_{le}} \eta_{le}] = 0 \quad (29)$$

Consider now some important special cases:

2.5.1 Rigid Wing ($\alpha \equiv 0$)

From (29) and $\bar{\alpha} = 0$,

$$\frac{pl}{U} = \frac{3}{2} \frac{[C_{L\eta te} + rC_{L\eta le}]\eta_{te}}{C_{L\alpha}} \quad (30)$$

where

$$r = \frac{\eta_{le}}{\eta_{te}} \quad (31)$$

2.5.2 Reversal ($pl/U = 0$)

From (29),

$$\bar{\alpha}_R = -\frac{3}{2} \frac{[C_{L\eta te} + rC_{L\eta le}]\eta_{te}}{\frac{12}{\pi^2} C_{L\alpha}} \quad (32)$$

From (28),

$$\bar{\alpha}_R = -\frac{\lambda_R \{ [C_{MAC\eta te} + rC_{MAC\eta le}] + \frac{e}{c} [C_{L\eta te} + rC_{L\eta le}] \} \frac{4}{\pi} \eta_{te}}{[-(\frac{\pi}{2})^2 + \lambda_R C_{L\alpha} \frac{e}{c}]} \quad (33)$$

Now equating the right hand sides of (32) and (33) and solving for λ_R , we obtain

$$\lambda_R = \frac{(\frac{\pi}{2})^2}{C_{L\alpha} \{ \frac{e}{c} [1 - \frac{96}{3\pi^3}] - \frac{96}{3\pi^3} \frac{[C_{MAC\eta te} + rC_{MAC\eta le}]}{[C_{L\eta te} + rC_{L\eta le}]} \}} \quad (34)$$

A further special case is $e/c = 0$. Then (34) reduces to

$$\lambda_R = -\frac{3\pi^5}{384 C_{L\alpha}} \frac{[C_{L\eta te} + rC_{L\eta le}]}{[C_{MAC\eta te} + rC_{MAC\eta le}]}$$

This is analogous to the result one obtains for lift reversal in the absence of rolling. Note also that the dependence of λ_R on e/c in (34) is very weak for typical values of e/c and the aerodynamic coefficients.

2.5.3 Divergence ($\eta_{te} = \eta_{le} = 0$)

Setting the determinant of coefficients of $\bar{\alpha}$ and (pl/U) from (28) and (29) to zero and solving for $\lambda = \lambda_D$, one obtains

$$\lambda_D = \frac{(\frac{\pi}{2})^2}{C_{L\alpha}(\frac{e}{c})[1 - \frac{96}{\pi^4}]} \quad (35)$$

Note: $\lambda_D = (\pi/2)^2$ is the divergence condition for "symmetrical" divergence, i.e. no rolling. Hence the λ_D with rolling included is much higher and indeed, with rolling,

$$\lambda_R \ll \lambda_D$$

Compare (34) to (35). This greatly increased value for λ_D when rolling occurs has presumably been observed by practioners for many years. However, the standard texts [1,2] are silent on this issue and an admittedly informal and incomplete survey of colleagues has not shown a general awareness of this result. Hancock [15] has pointed out that rigid body translation and pitching motions may impact symmetrical divergence.

2.5.4 Rolling Effectiveness (general λ)

Solving Eqs.(28) and (29), one obtains

$$\frac{pl}{U} = \frac{N_p}{D} \quad (36)$$

$$\bar{\alpha} = \frac{N_\alpha}{D} \quad (37)$$

where

$$D \equiv \left\{ -\left[\left(\frac{\pi}{2}\right)^2 + \frac{e}{c}\lambda C_{L\alpha}\right] + \frac{96}{\pi^4}\frac{e}{c}\lambda C_{L\alpha}\right\} C_{L\alpha} \quad (38)$$

$$\begin{aligned} N_p \equiv & \left\{ -\frac{3}{2}\left[\left(\frac{\pi}{2}\right)^2 + \frac{e}{c}\lambda C_{L\alpha}\right][C_{L\eta te} + rC_{L\eta le}] \right. \\ & \left. + \frac{48}{\pi^3}\lambda C_{L\alpha}[(C_{MAC\eta te} + rC_{MAC\eta le}) + \frac{e}{c}(C_{L\eta te} + rC_{L\eta le})] \right\} \eta_{te} \end{aligned} \quad (39)$$

$$\begin{aligned} N_\alpha \equiv & -C_{L\alpha}\left\{ -\frac{4}{\pi}\lambda[(C_{MAC\eta te} + rC_{MAC\eta le}) + \frac{e}{c}(C_{L\eta te} + rC_{L\eta le})] \right. \\ & \left. + \frac{3}{2}\frac{8}{\pi^2}\frac{e}{c}\lambda(C_{L\eta te} + rC_{L\eta le}) \right\} \eta_{te} \end{aligned} \quad (40)$$

Now using (35) and (38),

$$D = \left\{ \lambda C_{L\alpha} \frac{e}{c} \left[-1 + \frac{96}{\pi^4} \right] + \left(\frac{\pi}{2}\right)^2 \right\} C_{L\alpha} = \left(\frac{\pi}{2}\right)^2 C_{L\alpha} \left\{ 1 - \frac{\lambda}{\lambda_D} \right\} \quad (41)$$

and using (34) and (39)

$$N_p = \frac{3}{2} \left(\frac{\pi}{2}\right)^2 [C_{L\eta te} + rC_{L\eta le}] \left\{ 1 - \frac{\lambda}{\lambda_R} \right\} \eta_{te} \quad (42)$$

Thus from Eqs.(41) and (42), and recalling Eq.(30),

$$\frac{pl/U}{\frac{3}{2} \frac{[C_{L\eta te} + r C_{L\eta te}] \eta_{te}}{C_{L\alpha}}} = \frac{1 - \lambda/\lambda_R}{1 - \lambda/\lambda_D} \quad (43)$$

or

$$RE \equiv \frac{(pl/U)}{(pl/U)_{RIGID}} = \frac{1 - \lambda/\lambda_R}{1 - \lambda/\lambda_D}$$

Note: One could also determine a dynamic pressure for which $\bar{\alpha} = 0$, i.e. $N_\alpha = 0$. At such a dynamic pressure, the rolling rate is the same as that for a rigid wing of course.

2.6 Numerical Results

2.6.1 Reversal results:

From Eq.(34), one obtains the following.

e/c	r	λ_R
0	0	2.05
0	1	2.94
0	2	4.71
0	3	10.0
0	4	∞
0	5	-11.2
0	-1	1.53
0	-2	1.17

Note: These results are also quite accurate for say any $|\frac{e}{c}| < 0.1$

2.6.2 Divergence results:

From Eq.(35), one obtains the following.

$$\begin{aligned} e/c = 0 & \quad , \quad \lambda_D = \infty \\ e/c = 0.1 & \quad , \quad \lambda_D = 170 \end{aligned}$$

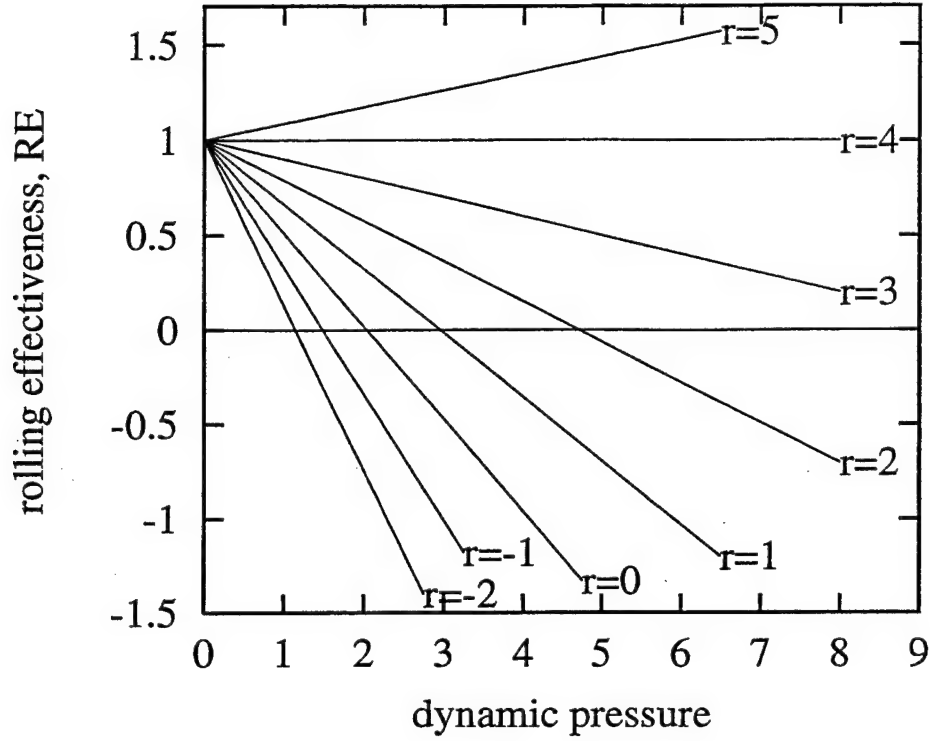


Figure 4: Rolling effectiveness, $RE = \frac{(pl/U)}{(pl/U)_{RIGID}}$, vs dynamic pressure, λ . Note: $\lambda \equiv \frac{qc^2l^2}{GJ}$, $\frac{pl}{U} = 0 \Rightarrow$ REVERSAL and $r \equiv$ ratio of leading to trailing edge control surface rotation.

Note that $\lambda_D \gg \lambda_R$ for a rolling wing. Thus (43) may be further simplified to

$$RE \equiv \frac{(pl/U)}{(pl/U)_{RIGID}} \cong 1 - \lambda/\lambda_R \quad (44)$$

These results are shown graphically in Figure 4 and are entirely analogous to those for the typical section airfoil. Note, in particular, that an adaptive control strategy where one selects $r > 0$ for small and $r < 0$ for large λ appears attractive. Of course, large λ occurs for large flow dynamic pressure, q , or small torsional stiffness, GJ .

2.7 Adaptive Design Considerations

The full implications for adaptive design are many. Here a few key ideas are highlighted. For simplicity we assume the elastic axis and aerodynamic center coincide, $e/c=0$. To make

the discussion more transparent, recall Eq. (30) and (34) and rewrite Eq. (44) as follows.

$$\tilde{P} \equiv \frac{pl}{\frac{3}{2}\sqrt{\frac{2GJ}{\rho c^2 l^2}}\eta_{te}} = \sqrt{\lambda} \left\{ \left[\frac{C_{L\eta te}}{C_{L\alpha}} + \lambda \frac{C_{MAC\eta te}}{3\pi^5/384} \right] + r \left[\frac{C_{L\eta le}}{C_{L\alpha}} + \lambda \frac{C_{MAC\eta le}}{3\pi^5/384} \right] \right\} \quad (45)$$

In this form, the explicit dependence of roll rate on the ratio of dynamic pressure to wing torsional stiffness, λ , is seen as well as the individual roles of the trailing and leading edge control surfaces. The rolling rate is now normalized with respect to a parameter based upon wing stiffness, chord, span and fluid density as well as control surface rotation, η_{te} .

In Eq. (45) the explicit dependence of the trailing edge control surface contribution to the rolling rate on dynamic pressure is clear. Recall the reversal dynamic pressure for the trailing edge control surface alone is

$$\lambda_R|_{r=0} = \frac{3\pi^5}{384} \frac{C_{L\eta te}}{C_{L\alpha} C_{MAC\eta te}} \quad (46)$$

Thus the contribution of the trailing edge control surface to the rolling rate changes sign when

$$\lambda > \lambda_R|_{r=0} \quad \text{or} \quad \lambda < \lambda_R|_{r=0}$$

Of course, the leading edge control surface alone does not undergo reversal since the twist due to the leading edge control surface rotation increases the rolling rate. See the term multiplied by r in Eq. (45).

From the above observations based upon Eq. (45), it is clear that one wants to make r as large as possible and then, when the contribution of the trailing edge control surface to the rolling rate goes to zero as $\lambda \rightarrow \lambda_R|_{r=0}$, reverse the sign of r and η_{te} to maximize the roll rate over the full range of dynamic pressure. To show this concisely consider Figure 5.

Figure 5 shows the variation of rolling rate (normalized by the trailing edge control surface rotation) with dynamic pressure for a given level of wing torsional stiffness. In our linear aeroelastic model the rolling rate is proportional to the trailing edge rotation for fixed ratio of leading to trailing edge rotations. Thus the inverse of Figure 5 may also be interpreted as the trailing edge rotation required for a given rolling rate.

When there is no leading edge control ($r=0$), there is a dynamic pressure when the rolling rate goes to zero, i.e. the reversal dynamic pressure for a trailing edge control surface only.

Of course, for small dynamic pressure and in the limit as the dynamic pressure tends to zero, the roll rate also tends to zero.

With leading edge control added ($r \neq 0$), reversal is eliminated using the adaptive strategy previously described. Indeed for a sufficiently large leading edge control authority, the rolling rate is a monotonically increasing function of dynamic pressure. This result also implies that for a given desired rolling rate, the trailing edge (and leading edge) control surface rotations needed are monotonically decreasing functions of dynamic pressure. This is an attractive design option as it implies that the leading and trailing edge control authority may be determined by low dynamic pressure requirements to achieve desired rolling rates.

The value of r for which the dependence of p on λ and vice versa is monotonic may be determined from a further analysis of Eq. (45). It is given by

$$r = 2 / \left[-3 \frac{C_{MAC\eta_{le}}}{C_{MAC\eta_{te}}} + \frac{C_{L\eta_{le}}}{C_{L\eta_{te}}} \right] \quad (47)$$

For the aerodynamic data used here, $r=2.43$.

Representative results from Eq. (45) are shown by the solid lines in Figure 5 using the adaptive control strategy. Also shown for reference are the results that are obtained when the sign of r is not changed adaptively. See the dashed lines in Figure 5. Clearly using the adaptive strategy has a very beneficial effect on the rolling rate.

There is another interesting set of questions regarding the optimum choice of wing torsional stiffness. For a sufficiently flexible wing, one could operate in the post-classical reversal regime, i.e. $\lambda > \lambda_R|_{r=0}$, for virtually the entire range of flight conditions. Of course divergence (or flutter) considerations may limit this option. Whether this option will prove attractive remains a subject for future investigation.

CONCLUDING REMARKS

A leading edge control surface may be used to counteract the tendency of a trailing edge control surface to undergo aeroelastic reversal. Results obtained here from simple mathematical models support results obtained in more complex models including flight test and wind tunnel results [3-10]. An attractive adaptive strategy to program the leading and trailing edge control surface rotations with flight condition has been suggested.

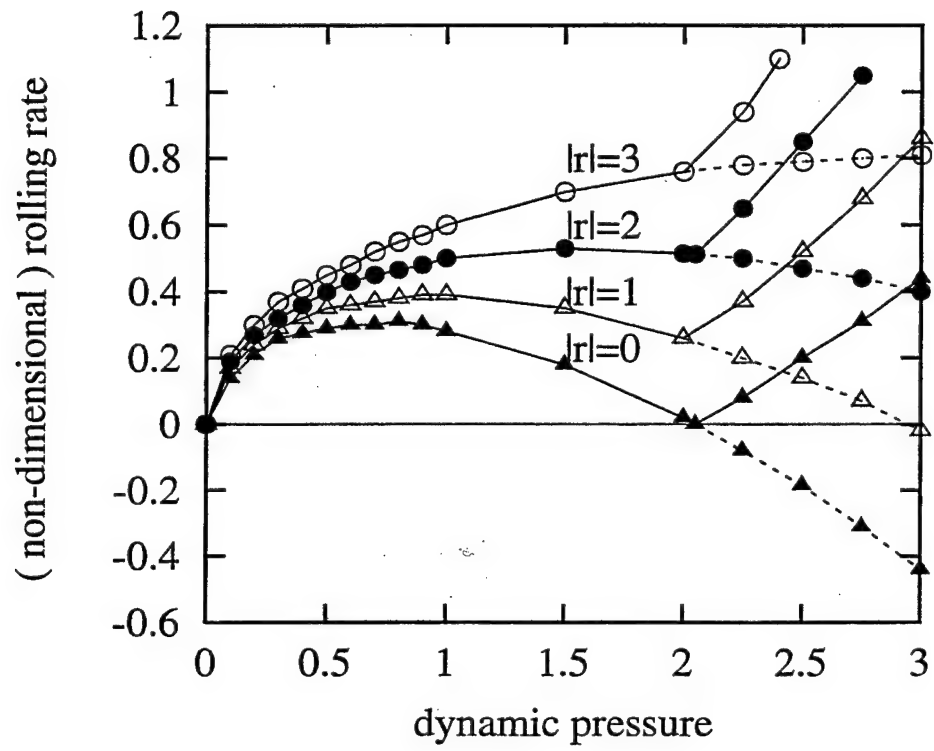


Figure 5: (Non-Dimensional) Rolling rate vs dynamic pressure: comparison of non-adaptive and adaptive control strategies.

Moreover the effect of the rolling degree of freedom to increase the dynamic pressure at which aeroelastic divergence occurs is emphasized. This suggests it may be of interest to include the rolling degree of freedom in the study of other aeroelastic phenomena including (anti-symmetric) flutter.

Finally, it is possible that the oscillation of a leading edge control surface may be used to create a favorable effect on such dynamic phenomena as vortex breaking or bursting. See [16] for a relevant experimental study. To assess this possibility will require a full dynamic, aeroelastic model and analysis, of course, and is well beyond the scope of this paper.

ACKNOWLEDGMENTS

The authors would like to thank Frank Eastep, Jay Kudva, Brian Sanders, Terry Weishaar and Rudy Yurkovich for helpful discussions of the literature and insights not yet reported in the literature.

REFERENCES

1. Bisplinghoff, R.L., Ashley, H. and Halfman, R.L., "*Aeroelasticity*," Addison-Wesley, 1955. Also available in a Dover Edition.
2. Dowell, E.H., Crawley, E.F., Curtiss, H.C., Jr., Peters, D.A., Scanlan, R.H. and Sisto, F., "*A Modern Course in Aeroelasticity*", Kluwer Publishers, Third Edition, 1995.
3. Noll, T. E. and Eastep, F. E., "Active Flexible Wing Program", *Journal of Aircraft*, Vol. 32, No. 1, January-February, 1995, pg. 9.
4. Woods-Vedeler, J. A., Pototzky, A. S. and Hoadley, S. T., "Rolling Maneuver Load Alleviation Using Active Controls", *Journal of Aircraft*, Vol. 32, No. 1, January-February, 1995, pp.68-76.
5. Andersen, G., Forster, E., Kolonay, R. and Eastep, F., "Multiple Control Surface Utilization in Active Aeroelastic Wing Technology", *Journal of Aircraft*, Vol. 34, No. 4, July-August, 1997, pp.552-557.
6. Zink, P. S., Mavris, D.N., Love, M. H. and Karpel, M., "Robust Design for Aeroelasti-

cally Tailored /Active Aeroelastic Wing", 7th AIAA/USAF/NASA/ SSMO Symposium on Multidisciplinary Analysis and Optimization, St. Louis, MO, September 2-4, 1998. AIAA Paper 98-4781.

7. Weisshaar, T.A., Duke, D.K. and Dobbins, A., "Active Aeroelastic Tailoring With Adaptive Continuous Control Surfaces", AIAA Paper 2000-1619.

8. Flick, P.M and Love, M. H., "The Impact of Active Aeroelastic Wing Technology on Conceptual Aircraft Design", Paper Presented at the RTO AVT Specialists Meeting on "Structural Aspects of Flexible Aircraft Control", Ottawa, Canada, October 18-20,1999. RTO MP-36.

9. Yurkovich, R. R., "Optimum Wing Shape for an Active Flexible Wing", Proceedings of the AIAA/ASME/ASCE/ARS 36th Structures, Structural Dynamics and Materials Conference, New Orleans, LA, 1995.

10. Pendleton, E., Lee, M. and Wasserman, L., "Application of Active Flexible Wing Technology to the Agile Falcon," *Journal of Aircraft*, Vol.29, No.3, May-June, 1992, pp. 444-451.

11. Prechtel, E. F., and Hall, S. R., "Design of a High Efficiency, Large Stroke, Electromechanical Actuator," *Journal of Smart Materials and Structures*, " Vol.8, No.1,1999, pp 13-30.

12. Ardilean, E., and Clark, R. L., "V-stack Piezoelectric Actuator", SPIE 8th Annual International Symposium on Smart Structures and Materials, 4-8 March, 2001, Newport Beach, CA.

13. Kuethe, A.M. and Chow, C.-Y., " *Foundations of Aerodynamics: Bases of Aerodynamic Design* " , Wiley, New York, 1986.

14. Dowell, E.H. and Hall, K.C., " Modeling of Fluid-Structure Interaction," *Annual Review of Fluid Mechanics*, 2001, Vol.33, pp. 445-490.

15. Hancock, G.J., "The Static Aeroelastic Deformation of Slender Configurations. Part I: Some Elementary Concepts of Static Deformation, and Part II: Some Calculations on Slender Plate Aircraft, Including Nonlinear Aerodynamics". *The Aeronautical Quarterly*, August, 1961, pp. 293-308 and November, 1961, pp. 372-394. [The authors would like to thank Professor Terence A. Weisshaar for drawing this reference to our attention.]

16. Sahin, B., Akilli, H., Lin, J.-C., and Rockwell, D., "Vortex Breakdown-Edge Interaction: Consequence of Edge Oscillations," *AIAA Journal*, Vol.39, No. 5, 2001, pp. 865-876.

EXPERIMENTAL AND THEORETICAL STUDY ON ROLLING EFFECTIVENESS OF MULTIPLE CONTROL SURFACES

Ref. 3
Submitted
to J. A. A. J.
Journal

Demian Tang ¹, Aiqin Li ² and Earl H. Dowell ³
Duke University, Durham, North Carolina 27708-0300

ABSTRACT

It is well known that the effectiveness of a trailing edge control surface can be substantially diminished due to the elastic twist of an airfoil or rolling wing. This aeroelastic phenomenon is known by the name of control surface reversal when the lift or rolling rate vanishes at a sufficiently large ratio of flow dynamic pressure to airfoil or wing stiffness.

However a leading edge control surface can be used to counteract control surface "reversal" and indeed, in principle, a leading edge control surface can entirely cancel the tendency of the trailing edge control surface to undergo reversal. Moreover analysis shows that by using a simple adaptive control strategy one can use a combination positive and negative control surface rotations to maximize lift and rolling effectiveness or minimize control surface rotations.

In the present work, a theoretical-experimental study of the effectiveness of trailing and leading edge control surfaces has been made for a rolling wing-fuselage model. An experimental model and wind tunnel test are used to assess the theoretical results. The theoretical model includes the inherently nonlinear dry friction damping moment between the spindle support and the experimental aeroelastic wing model for the rolling degree of freedom. A three dimensional vortex lattice aerodynamic theory is employed. The present paper provides new insights into the behavior and design of an adaptive aeroelastic wing using trailing and leading edge control surfaces.

¹Research Associate Professor, Department of Mechanical Engineering and Materials Science

²Research Assistant, Department of Mechanical Engineering and Materials Science

³J. A. Jones Professor, Department of Mechanical Engineering and Materials Science and Director of the Center for Nonlinear and Complex Systems. Dean Emeritus, Pratt School of Engineering

Introduction

Control surface reversal due to unfavorable aeroelastic effects is one of the classical phenomena of static aeroelasticity. It is treated in textbooks [1,2] and standard courses on aeroelasticity. However, an appropriately chosen combination of leading and trailing edge control surface deflections plus an adaptive control law can be used to achieve improved rolling performance and/or to minimize roll maneuver loads.

Related results have been reported from the Active Flexible Wing (AFW) program and more recent work on the Active Aeroelastic Wing (AAW) technology. Noll and Eastep [3] present a cogent overview and organized an issue of the Journal of Aircraft on the Active Flexible Wing program. In this special issue there are eleven (11) papers that report theoretical and experimental investigations on actively controlled wings.

Anderson, Forster, Kolonay and Eastep [4] gave deeper insights into the favorable synergy that can be created by a combination of leading and trailing edge controls. In their work they noted that the unfavorable aeroelastic twist that can lead to trailing edge control surface reversal can be offset by a leading edge control surface. Moreover, the trailing edge control surface reversal can be eliminated and a constant roll authority maintained over a wide range of flight dynamic pressures by an appropriate combination of leading and trailing edge control surface deflections.

More recent work on the Active Aeroelastic Wing technology has dealt with improvements in design optimization methodologies, reduction of drag, and an adaptive change in torsional stiffness to allow both pre- and post-classical reversal operation of an Active Aeroelastic Wing [5-8].

As reported previously [9], the same conceptual benefit that can be obtained by using an adaptive torsional stiffness change can also be realized by using an adaptive aeroelastic wing with the gearing ratio between leading and trailing edge control surfaces programmed to change with flight dynamic pressure. Also some new actuation technologies are currently under development for high-bandwidth actuator, leveraging high energy density materials such as piezoceramics. Two such actuation technologies include the X-frame actuator developed at MIT [10] and the V-stack actuator developed at Duke University [11]. Thus, implementation of an adaptive aeroelastic wing with leading and trailing edge control surfaces appears promising and practical.

Reference [9] considered the basic adaptive concept and the fundamental physical phenomena for two models of (1) an airfoil and (2) a rolling wing. These results using simple structural models and aerodynamic strip theory have shown the effectiveness of an adaptive strategy that programs the leading and trailing edge control surface rotations with flight condition. In order to validate the predictions of the theory, a wind tunnel wing-fuselage model with the leading and trailing edge control surfaces has been designed and tested to measure the rolling effectiveness vs dynamic pressure for different combination of leading and trailing edge control surface rotation. Of course, the wing-fuselage model is in a three-dimensional flow field. A three dimensional incompressible (linear) vortex lattice aerodynamic theory and a corresponding reduced order aerodynamic model are used in the present analysis [12]. Results for subsonic, compressible flow can be obtained using the Prandtl-Glauert scaling law.

Finally, it is noted that for the present wind tunnel test model, there is a nonlinear dry friction damping arising from the rubbing or sliding between the experimental aeroelastic wing-fuselage model and the support spindle. This nonlinear factor is considered in the present experimental-theoretical study.

Experimental Model and Measurements

The experimental model consists of a right and left wing and a fuselage (slender body). For simplicity, the wing model is a rectangular aluminum plate of thickness 0.317 cm, total chord length (c) of 10.16 cm (including the leading and trailing control surface chords) and span length (l) of 10.16 cm. The plate has a very large bending and torsional stiffness and thus the wing per se is assumed to be rigid. The leading and trailing control surfaces each have a chord length of 1.73 cm (17% c) and a full span length of 10.16 cm (100% l) hinged on the leading and trailing edges, respectively. The rotation angle of the control surface can be adjusted. The torsional flexibility of the wing is provided by a flat spring at the wing root which can be adjusted. The elastic axis is placed at the quarter of the wing chord. In order to also place the chordwise center of gravity axis of the wing at the elastic axis, the leading edge control surface is made of brass and the trailing control surface is made of aluminum plate. Also a small slender body mounted at the wing root is used to provide weight balance.

The fuselage has a circular cross-section with a diameter of 2.54 cm. It includes two parts. The front part is a slender body with a parabolic forebody which can rotate about

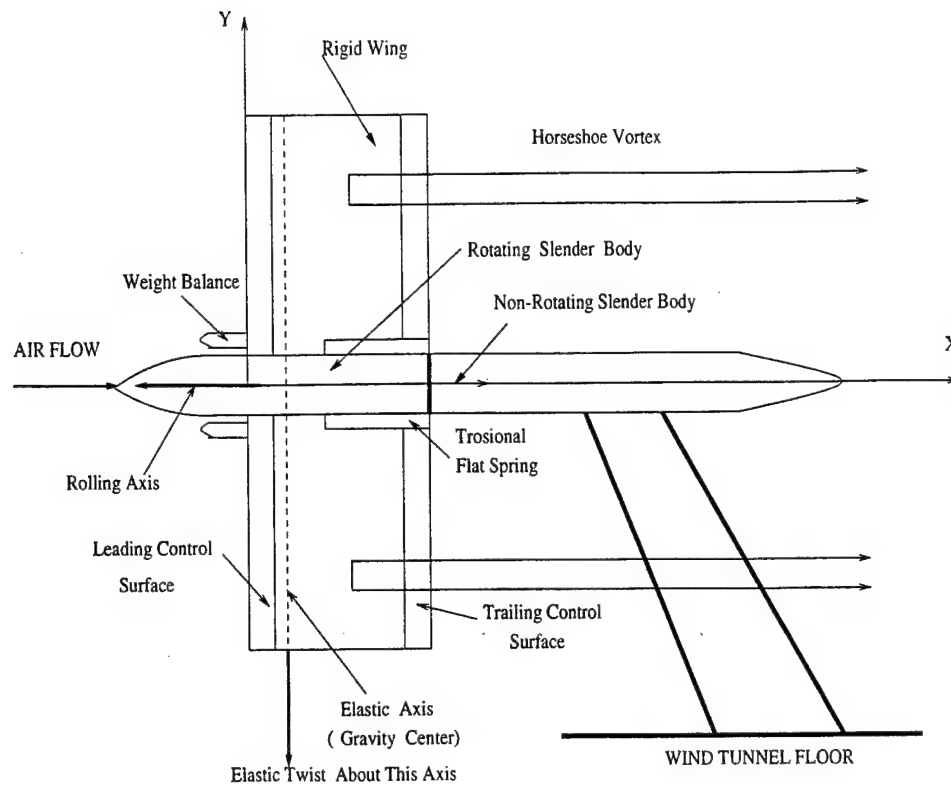


Figure 1: Physical representation of experimental model. Also shown is a three-dimensional vortex lattice model (linear) of the unsteady flow.

the fuselage center axis and supports the wings. The rear part is a non-rotating slender body with a parabolic aftbody which is used to support the front portion of the slender body and is connected to the wind tunnel floor by a support or sting rod. See Figure 1.

The wings are allowed to rotate (roll) about the center axis of the fuselage. The rolling rate (angular velocity) is measured by an angular transducer, R30A, mounted on the rear end of the non-rotating portion of the slender body.

A physical representation of wing model geometry along with a three-dimensional vortex lattice model (linear) of the unsteady flow is shown in Figure 1 and a photograph of the aeroelastic model in the wind tunnel is shown in Figure 2.

Static Aeroelastic Equations

As shown in Figure 1, a straight rectangular wing with leading and trailing edge control

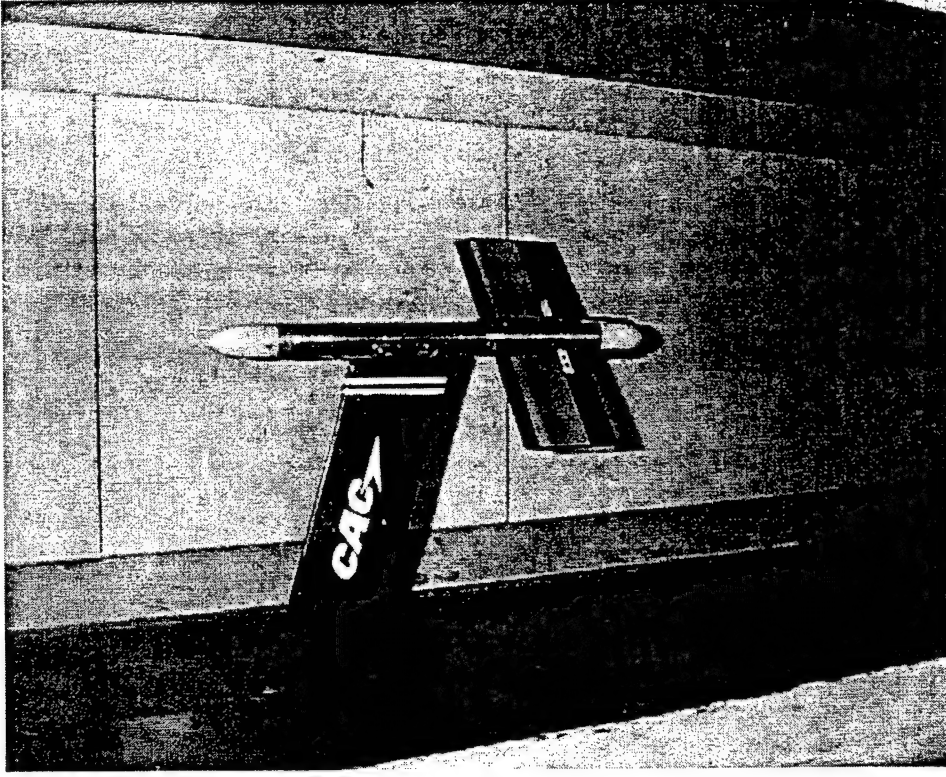


Figure 2: Photograph of the aeroelastic model in the wind tunnel.

surfaces that are full span is considered. The experimental model is symmetrical about the center axis of the fuselage. The aerodynamic forces on the fuselage (slender body) are neglected. The equation of torsional equilibrium about the elastic axis of the rigid wing is as follows [1,2]. It expresses the balance of moments about the elastic axis due to the elastic spring and the aerodynamic forces in the Eulerian coordinate system (x,y,z) .

$$K_{\alpha}\alpha + M_y = 0 \quad (1)$$

or

$$K_{\alpha}\alpha + \int_{r_f}^{l+r_f} \int_0^c \Delta p(x,y)(x - x_e) dx dy = 0 \quad (2)$$

where $\Delta p(x,y)$ is the pressure distribution on the wing, x_e is the distance from the elastic center to leading edge of the wing, K_{α} is the torsional stiffness and α is the twist angle of the wing. r_f is the radius of the slender body (fuselage).

The rigid body rolling equation of equilibrium about the center axis of the fuselage is expressed as follows.

$$\int_{r_f}^{l+r_f} Lydy - M_d \frac{p}{|p|} = 0 \quad (3)$$

or

$$\int_{r_f}^{l+r_f} y \int_0^c \Delta p(x, y) dx dy - M_d \frac{p}{|p|} = 0 \quad (4)$$

In this equation a dry friction damping moment between the spindle support and the aeroelastic wing model is taken into account. M_d is the nonlinear Coulomb friction damping moment and p is the wing rolling rate.

Introducing non-dimensional quantities in Eq.(2) and (4) as follows,

$$\begin{aligned} \overline{\Delta p}(x, y) &= \frac{\Delta p(x, y)}{\rho U^2} \quad , \quad \bar{x} = \frac{x}{c} \quad , \quad \bar{x}_e = \frac{x_e}{c} \\ \bar{y} &= \frac{y}{c} \quad , \quad \bar{K}_\alpha = \frac{K_\alpha}{\rho U^2 c^3} \quad \text{and} \quad \bar{M}_d = \frac{M_d}{\rho U^2 c^3} \end{aligned}$$

the dimensionless equations corresponding to Eq.(2) and (4) are

$$\bar{K}_\alpha \alpha + \int_{r_f/c}^{(l+r_f)/c} \int_0^1 \overline{\Delta p}(\bar{x}, \bar{y}) (\bar{x} - \bar{x}_e) d\bar{x} d\bar{y} = 0 \quad (5)$$

and

$$\int_{r_f/c}^{(l+r_f)/c} \bar{y} \int_0^1 \overline{\Delta p}(\bar{x}, \bar{y}) d\bar{x} d\bar{y} - \bar{M}_d \frac{p}{|p|} = 0 \quad (6)$$

To model the above aeroelastic structural/fluid system, the aerodynamic flow about the structural model is assumed to be incompressible, inviscid and irrotational. Here an unsteady (linear) vortex lattice method is used to model this flow [12]. The wing and wake are divided into a number of elements. In the wake and on the wing all the elements are of equal size, dx , in the streamwise direction. Point vortices are placed on the wing and in the wake at the quarter chord of the elements. At the three-quarter chord of each panel element a collocation point is placed for the downwash, i.e. we require the velocity induced by the discrete vortices to equal the downwash arising from the unsteady motion of the wing. Thus the following relationship is obtained,

$$w_i^{t+1} = \sum_j^{kmm} K_{ij} \Gamma_j^{t+1}, \quad i = 1, \dots, km \quad (7)$$

where w_i^{t+1} is the dimensionless downwash at the i th collocation point at time step $t + 1$, Γ_j is the j th normalized vortex strength by cU , and K_{ij} is an aerodynamic kernel function for the horseshoe vortex. km and kmm are the number of vortex elements on the wing and

total number of vortices on both the wing and wake in the x- direction, respectively. For the three-dimensional incompressible flow, the kernel function is given by (see Ref.[13])

$$K_{ij}(\bar{x}, \bar{y}, \bar{x}_a, \bar{y}_a, \bar{x}_b, \bar{y}_b) = \frac{-1}{4\pi(\bar{y}_i - \bar{y}_{ja})} \left[1 + \frac{\sqrt{(\bar{x}_i - \bar{x}_{ja})^2 + (\bar{y}_i - \bar{y}_{ja})^2}}{\bar{x}_i - \bar{x}_{ja}} \right] \\ + \frac{1}{4\pi(\bar{y}_i - \bar{y}_{jb})} \left[1 + \frac{\sqrt{(\bar{x}_i - \bar{x}_{ja})^2 + (\bar{y}_i - \bar{y}_{jb})^2}}{\bar{x}_i - \bar{x}_{ja}} \right] \quad (8)$$

where \bar{x}_i is the location of the i th collocation point, and \bar{y}_{ja} and \bar{y}_{jb} are the locations of the two j th trailing vortex segments which are parallel to the x axis at $\bar{y} = \bar{y}_a$ and $\bar{y} = \bar{y}_b$.

The aerodynamic matrix equation (general) is given by

$$[A]\{\Gamma\}^{t+1} + [B]\{\Gamma\}^t = [T]\{w\}^{t+1} \quad (9)$$

where $[A]$ and $[B]$ are aerodynamic coefficient matrices. $[T]$ is a transfer matrix for determining the relationship between the global vortex lattice mesh and the local vortex lattice mesh on the wing. For the present model the wing span is finite and anti-symmetric about the center axis of the fuselage. An anti-symmetric vortex condition is used for reducing the aerodynamic degrees of freedom. In this case the aerodynamic coefficient matrix, $[A]$, corresponding to the kernel function can be expressed as

$$A = K_{i,j}(\bar{x}, \bar{y}, \bar{x}_a, \bar{y}_a, \bar{x}_b, \bar{y}_b) - K_{i,j}(\bar{x}, \bar{y}, \bar{x}_b, -\bar{y}_b, \bar{x}_a, -\bar{y}_a)$$

The nondimensional downwash, w , contains contributions from the steady angle of attack α , the wing rolling rate, p , and rotational angles, η_{le}, η_{te} of the leading and trailing control surfaces, respectively. For the present model, Eq.(9) is expressed in matrix form as

$$[A]\{\Gamma\}^{t+1} + [B]\{\Gamma\}^t = \{T_\alpha\}\alpha^{t+1} - \{T_p\}\frac{p}{U}^{t+1} + \{T_t\}\eta_{te} + \{T_l\}\eta_{le} \quad (10)$$

where $\{T_\alpha\}$ and $\{T_p\}$ are the elastic twist and rolling rate transfer matrices for determining the relationship between the global vortex lattice mesh and the local vortex lattice mesh on the wing. $\{T_t\}$ and $\{T_l\}$ are the transfer matrices for determining the relationship between the global vortex lattice mesh and the local vortex lattice mesh on the trailing and leading control surfaces, respectively.

The nondimensional pressure distribution on the rigid wing at the j th point is given by

$$\overline{\Delta p_j} = \frac{c}{\Delta x} [(\Gamma_j^{t+1} + \Gamma_j^t)/2 + \sum_i^j (\Gamma_i^{t+1} - \Gamma_i^t)] \quad (11)$$

Substituting Eq.(11) into Eq.(5) gives

$$\overline{K}_\alpha \alpha + \sum_{n=1}^{kn} \sum_{m=1}^{km} (\bar{x}_m - \bar{x}_e) [(\Gamma_{nm}^{t+1} + \Gamma_{nm}^t)/2 + \sum_i^m (\Gamma_{ni}^{t+1} - \Gamma_{ni}^t)] \Delta \bar{y} = 0 \quad (12)$$

or as expressed in matrix form,

$$\overline{K}_\alpha \alpha + \{D_2\}^T \{\Gamma\}^{t+1} + \{D_1\}^T \{\Gamma\}^t = 0 \quad (13)$$

where kn and km are the chordwise and spanwise numbers of vortex elements on the wing and here the superscript T indicates the matrix transpose.

Substituting Eq.(11) into Eq.(6) gives

$$\left\{ \sum_{n=1}^{kn} \bar{y}_n \sum_{m=1}^{km} [(\Gamma_{nm}^{t+1} + \Gamma_{nm}^t)/2 + \sum_i^m (\Gamma_{ni}^{t+1} - \Gamma_{ni}^t)] \right\} \Delta \bar{y} - \overline{M}_d \frac{p}{|p|} = 0 \quad (14)$$

or as expressed in matrix form,

$$\{C_2\}^T \{\Gamma\}^{t+1} + \{C_1\}^T \{\Gamma\}^t - \overline{M}_d \frac{p}{|p|} = 0 \quad (15)$$

where D_1, D_2, C_1 and C_2 are coefficient matrices describing the vortex element forces and moments on the wing.

Thus, combining Eq.(10),(13) and (15), a complete static aeroelastic state-space equation in matrix form is obtained for the unknown variables, Γ , α and p .

$$\begin{bmatrix} A & -T_\alpha & T_p/U \\ D_2^T & \overline{K}_\alpha & 0 \\ C_2^T & 0 & 0 \end{bmatrix} \begin{Bmatrix} \Gamma \\ \alpha \\ p \end{Bmatrix}^{t+1} + \begin{bmatrix} B & 0 & 0 \\ D_1^T & 0 & 0 \\ C_1^T & 0 & 0 \end{bmatrix} \begin{Bmatrix} \Gamma \\ \alpha \\ p \end{Bmatrix}^t = \begin{Bmatrix} T_t \eta_{te} + T_l \eta_{le} \\ 0 \\ \overline{M}_d \frac{p}{|p|} \end{Bmatrix}^{t+\frac{1}{2}} \quad (16)$$

Following a similar treatment as described in Ref.[14], a reduced order aerodynamic model with static correction is constructed and the final aeroelastic state space model is given by

$$\begin{bmatrix} I & -Y_{Ra}^T [I - A(A+B)^{-1}]E \\ G_2 X_{Ra} & K + G_2(A+B)^{-1}E \end{bmatrix} \begin{Bmatrix} \gamma \\ \theta \end{Bmatrix}^{t+1} + \begin{bmatrix} -Z_{Ra} & -Y_{Ra}^T B(A+B)^{-1}E \\ G_1 X_{Ra} & G_1(A+B)^{-1}E \end{bmatrix} \begin{Bmatrix} \gamma \\ \theta \end{Bmatrix}^t = \begin{Bmatrix} 0 \\ -(G_1 + G_2)(A+B)^{-1}(T_t \eta_{te} + T_l \eta_{le}) + F_N \end{Bmatrix}^{t+\frac{1}{2}} \quad (17)$$

where where $\{\theta\} = \{\alpha, p\}$ is a vector of unknown variables and

$$[E] = [\{T_\alpha\}, \{-T_p/U\}] , [G_2] = \begin{bmatrix} \{D_2\}^T \\ \{C_2\}^T \end{bmatrix} , [G_1] = \begin{bmatrix} \{D_1\}^T \\ \{C_1\}^T \end{bmatrix}$$

$$[K] = \begin{bmatrix} \bar{K}_\alpha & 0 \\ 0 & 0 \end{bmatrix} , \{F_N\} = \begin{Bmatrix} 0 \\ \bar{M}_d \frac{p}{|p|} \end{Bmatrix} \quad (18)$$

$[X_{Ra}], [Y_{Ra}]$ are the reduced right and left eigenvector matrices of the vortex lattice eigenvalue model and $[Z_{Ra}]$ is a reduced eigenvalue matrix, $\Gamma = X_{Ra}\gamma$, with only the most dominant eigenmodes retained in the analysis.

Numerical Study

1. Validation of Aerodynamic Computation Code

In order to validate the present aerodynamic code, first consider a two dimensional thin airfoil and use two dimensional vortex lattice theory at $M = 0$. Results are presented for the pressure and lift coefficient responses to a step angle of attack of the airfoil, leading and trailing control surfaces, i.e. $\alpha = 1(rad)$, $\eta_{le} = 1(rad)$ and $\eta_{te} = 1(rad)$, respectively. Control surface chords of 20% are considered. The airfoil was modeled using 40 vortex elements, i.e., $km=40$. The wake was modeled using 160 vortex elements, i.e., $kmm=200$. The total number of vortex elements (or aerodynamic degrees of freedom) was 200. The vortex relaxation factor was taken to be $\alpha = 0.992$. The nonlinear Coulomb dry friction moment, M_d , is set to zero.

Figure 3 shows the lift coefficient of the airfoil vs nondimensional time, τ ($\tau = \frac{tU}{c}$). The solid line is for $\alpha = 1(rad)$, the broken line is for $\eta_{le} = 1(rad)$ and the dashed line is for $\eta_{te} = 1(rad)$, step angle of attack excitations. Figure 4 shows the corresponding nondimensional pressure distributions vs nondimensional chord, x , as the flow reaches its steady state, $\tau \rightarrow \infty$. A comparison between the present results and typical values of the aerodynamic coefficients from Ref.[15] is shown below in tabular form.

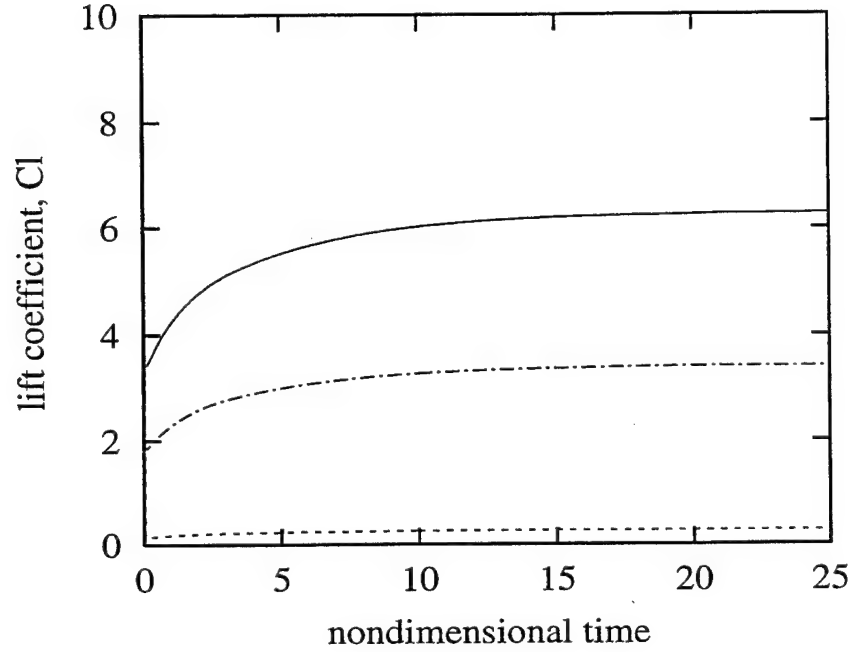


Figure 3: Lift coefficients of a thin airfoil vs nondimensional time, τ , for several different step angle of attack excitations of the airfoil and control surfaces.

Coefficients	Ref.[15]	present method
$C_{MAC\alpha}$	0	-0.0037
$C_{MAC\eta_{te}}$	-0.64	-0.65
$C_{MAC\eta_{le}}$	0.16	0.165
$C_{L\alpha}$	2π	6.271
$C_{L\eta_{te}}$	3.45	3.398
$C_{L\eta_{le}}$	0.255	0.266

The agreement is very close.

Consider now the present three dimensional flow model for the wing. Here again the aerodynamic coefficients are calculated. The wing was modeled using 400 vortex elements, i.e, $km=40$, $kn=10$. The wake was modeled using 800 vortex elements, i.e, $kmm=120$. The total number of vortex elements (or aerodynamic degrees of freedom) was 1200. The control surface chords are 20% of the total wing chord and the spans are 50% of the total wing span. The control surfaces are located on the outer half of the wing span. Both local and total aerodynamic lift coefficients are considered. The nonlinear Coulomb dry friction moment, M_d , is set to zero.

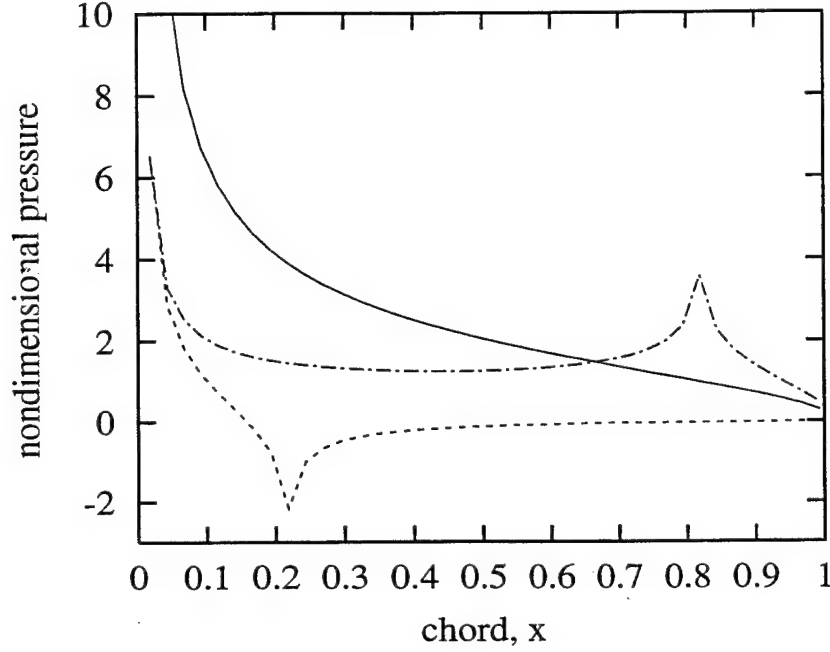


Figure 4: The nondimensional pressure distribution of a thin airfoil vs nondimensional chord position for different step angle of attack excitation as $\tau \rightarrow \infty$.

The local lift at $y = y_j$ is obtained by integrating the pressure difference along the local chord-line.

$$L_{local}^{t+1}(y_j) = \int_0^c \Delta p^{t+1}(x, y_j) dx \quad (19)$$

The local lift coefficient $C_{l,local}$ at $y = y_j$ is defined as

$$C_{l,local}^{t+1}(y_j) = L_{local}^{t+1}(y_j) / (\frac{1}{2} \rho U^2 c) \quad (20)$$

The total lift is obtained by integrating the local total lift along the span.

$$L^{t+1} = \int_{r_f}^{l+r_f} L_{local}^{t+1}(y) dy = l \sum_{j=1}^{k_n} L_{local}^{t+1}(y_j) \Delta \bar{y} \quad (21)$$

where $\Delta \bar{y} = \frac{l}{c} \frac{1}{k_n}$ and k_n is the number of spanwise discrete elements.

The total aerodynamic lift coefficient, C_l is defined by

$$C_l^{t+1} = L^{t+1} / \frac{1}{2} \rho U^2 A_w \quad (22)$$

where A_w is the total wing area.

The results are shown in Figure 5(a)-(b) for step angles of attack of the wing, leading and trailing control surfaces, respectively. Figure 5(a) shows the total lift coefficient of the wing vs nondimensional time, τ . The solid line is for $\alpha = 1(rad)$, the dashed line is for $\eta_e = 1(rad)$ and the broken line is for $\eta_{te} = 1(rad)$, step angle of attack excitations of the aerodynamic flow. All results have reached their steady values when $\tau > 10$. The steady total lift coefficients of the wing are $C_{L\alpha} = 1.97$, $C_{L\eta_{te}} = 0.73$ and $C_{L\eta_e} = 0.021$. Note that the lift contribution due to the leading edge control surface is quite small relative to the wing and trailing edge control surface. Figure 5(b) shows the corresponding nondimensional pressure distribution at mid-span vs nondimensional wing chord as $\tau \rightarrow \infty$. For the step angle of attack excitation of the wing, the maximum pressure is near the leading edge. For the leading control surface, the maximum pressure is still at the leading edge, but there is a negative peak pressure ($\overline{\Delta p} = -2.2$) at $\bar{x} = 0.22$, i.e. near the trailing edge of the leading edge control surface. The pressure distribution is almost zero when $\bar{x} > 0.3$. For the trailing edge control surface, the maximum pressure is ($\overline{\Delta p} = 2.7$) at $\bar{x} = 0.82$, i.e near the leading edge of the trailing edge control surface.

Figure 6 (a) shows the local lift coefficient of the wing vs nondimensional span. As expected, the local lift coefficient decreases near the tip and root of the wing for the step angle of attack excitation of the wing. (Note that an anti-symmetric vortex condition is used). The maximum value of 1.76 at $\bar{y} = 0.55$ is about 28% of that for a thin airfoil. For the leading edge control surface step angle of attack excitation, the maximum local lift coefficient is 0.024 at $\bar{y} = 0.65$. For the trailing edge control surface step angle of attack excitation, the maximum local lift coefficient is 1.06 at $\bar{y} = 0.75$. Figure 6 (b) shows the local moment coefficient of the wing vs nondimensional span. For the step angle of attack excitation of the wing, the maximum value is 0.11 at $\bar{y} = 0.25$. For the leading edge control surface excitation, the maximum local moment coefficient is 0.14 at $\bar{y} = 0.75$. For the trailing edge control surface excitation, the maximum local moment coefficient is -0.47 at $\bar{y} = 0.75$.

Figure 5 and Figure 6 are the results for the right wing. For the left wing, the aerodynamic excitations and forces are anti-symmetrical with respect to the center axis of the fuselage. Note that rolling is not permitted in this purely aerodynamic simulation.

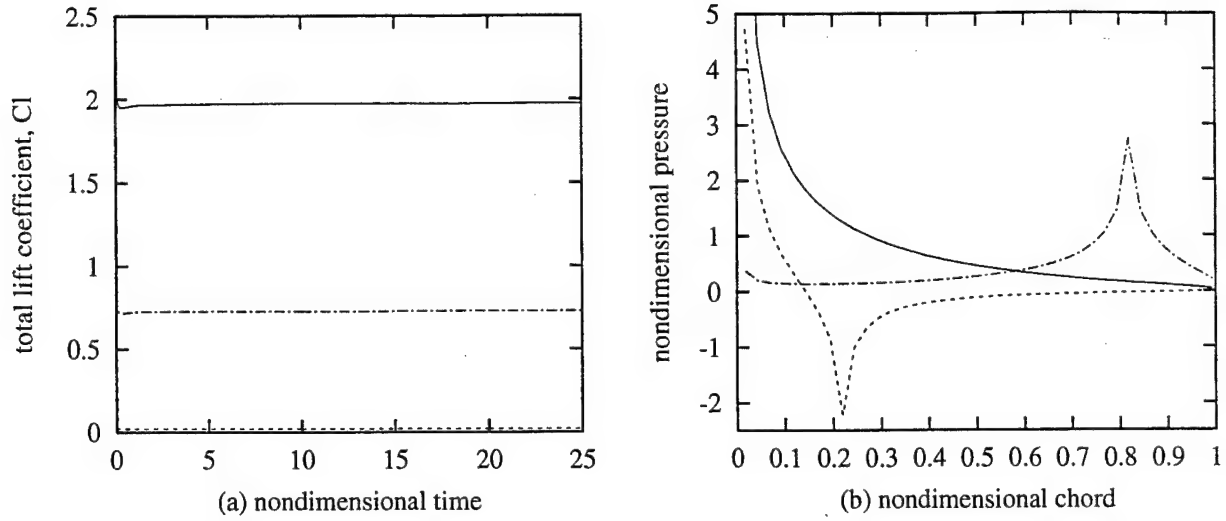


Figure 5: Aerodynamic response to step angles of attack for wing, leading and trailing edge control surfaces. (a) total lift coefficients, (b) nondimensional pressure distribution ($\tau \rightarrow \infty$).

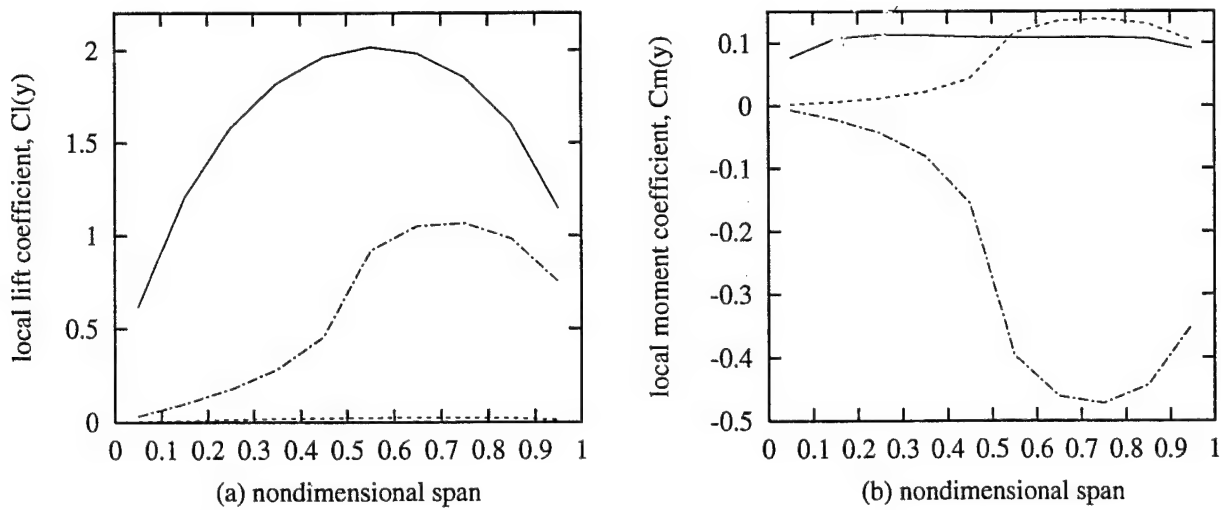


Figure 6: Aerodynamic response to step angles of attack for wing, leading and trailing edge control surfaces. (a) local lift coefficients, (b) local moment coefficients along the span.

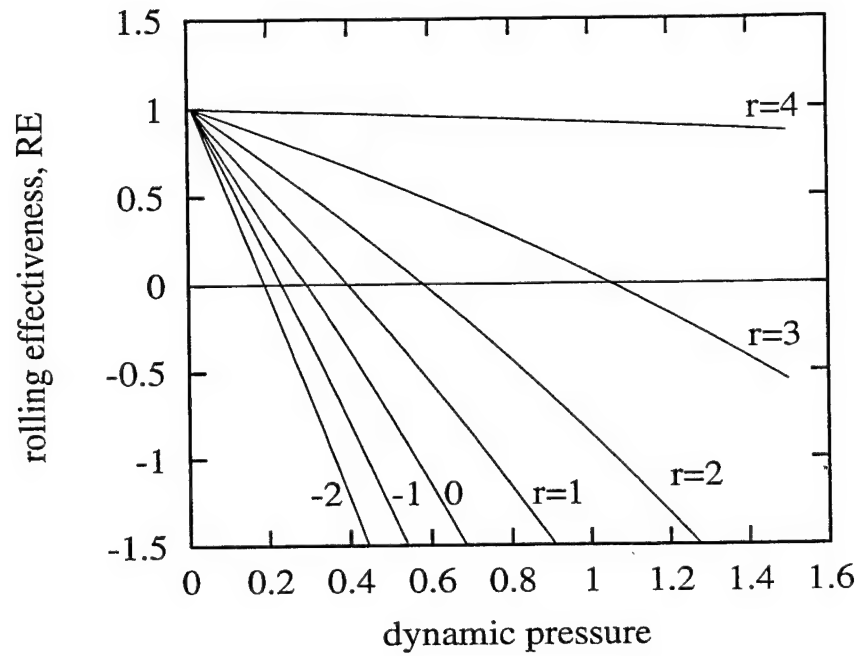


Figure 7: rolling effectiveness, RE , vs dynamic pressure, λ , for different r .

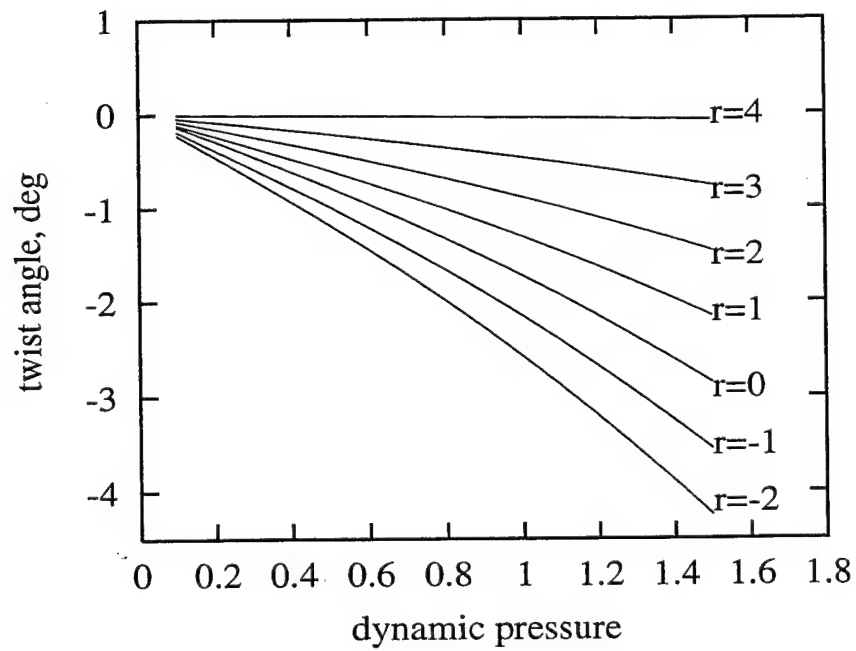


Figure 8: Elastic twist angle, α , vs dynamic pressure, λ , for different r .

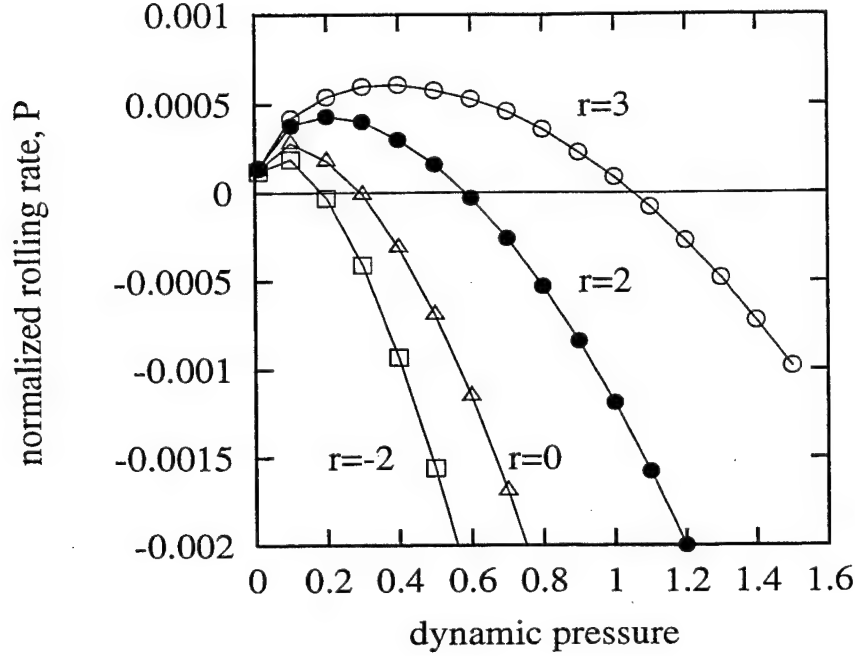


Figure 9: variation of notmalized rolling rate, \tilde{P} , vs dynamic pressure, λ , for $r=3, 2, 0$ and -2 .

2. Numerical Results for Effectiveness of Control Surfaces

A standard discrete time marching algorithm has been used to calculate the static response of this aeroelastic system using the full aerodynamic model, Eq.(16), and also the reduced order aerodynamic model, Eq.(17). The time step is constant for a given flow velocity U , $\Delta t = \Delta x/U$. For these calculations, $\bar{x}_e = 0.3$, $K_\alpha = 0.131$ kgm/rad and $M_d = 0$. The rotation angles of the leading and trailing control surfaces, η_{le} and η_{te} are the variables for a given flow velocity.

For the following discussion, the non-dimensional dynamic pressure λ , rolling effectiveness, RE , and rolling rate normalized by the trailing edge control surface rotation, \tilde{P} are defined as

$$\lambda \equiv \frac{\rho U^2 c^3}{K_\alpha}, \quad RE \equiv \frac{(pl/U)}{(pl/U)_{RIGID}}, \quad \lambda_R \equiv \lambda|_{pl/u=0}$$

and

$$\tilde{P} \equiv \frac{pl}{\sqrt{K_\alpha/\rho c^3}}/\eta_{te} = \sqrt{\lambda} \left(\frac{pl}{U} \right) / \eta_{te} \quad (23)$$

Figure 7 shows the rolling effectiveness, RE , vs dynamic pressure, λ for several different

ratios of leading to trailing edge control surface rotation. Rolling reversal occurs, i.e. $\frac{p_l}{U} = 0$ when $\lambda = 1.1, 0.6, 0.4, 0.3, 0.2, 0.15$ for $r = 3, 2, 1, 0, -1$ and -2 , respectively. Note that λ_R decreases as r decreases. Figure 8 shows the twist angle, α , vs dynamic pressure. The twist angle increases as dynamic pressure increases and r decreases for the range of parameters shown.

Figure 9 shows the variation of rolling rate, \tilde{P} , vs dynamic pressure, λ , for $r = 3, 2, 0$ and -2 . In our linear aeroelastic model the rolling rate is proportional to the trailing edge rotation for a fixed ratio of leading to trailing edge rotations. Thus the inverse of Figure 9 may also be interpreted as the trailing edge rotation required for a given rolling rate.

Note that to achieve the maximum rolling rate one should reverse the sign of r near $\lambda = \lambda_R|_{r=0}$ as was found previously for simpler models [9].

Theoretical and Experimental Correlation

For the present computational and experimental model, the aerodynamic and structural parameters are described in the previous Section, "Experimental Model and Measurements". The measured torsional stiffness is $K_\alpha = 0.032$ kgm/rad. The trailing edge control surface rotation is $\eta_t = 5^\circ$. Three typical cases for leading edge control are considered, i.e. the ratios of leading to trailing edge control surface rotations are $r = -1, 0$ and 1 .

The dry friction damping moment between the spindle support and the aeroelastic wing model, M_d , is determined by a experimental method as follows. From the wind tunnel test, a specific flow velocity called U_d can be determined where the rolling is just started from a rest state due to the aerodynamic rolling moment over-coming dry friction moment in the test model. Note that this flow velocity varies with the structural parameters. Substituting the known U_d and $p = 0$ into Eq.(10) and (13), the state variables, Γ^t, Γ^{t+1} and α^{t+1} can be solved using a standard discrete algorithm. Using Eq.(15), the Coulomb friction moment M_d of this system can be determined by

$$\overline{M}_d = \{C_2\}^T \{\Gamma\}^{t+1} + \{C_1\}^T \{\Gamma\}^t \quad (24)$$

where

$$M_d = \overline{M}_d \rho U_d^2 c^3 \quad (25)$$

Note that $\frac{p}{|p|} \equiv 1$ when $p = 0$.

The Coulomb friction moment, M_d , obtained from the experiment has a small variation with r . An average value, $M_d=0.00021$ kgm, is used in the following calculations.

Eq.(16) or (17) is a nonlinear equation to determine p and α when M_d is known. The computational procedure is follows.

Assuming a set of initial values, Γ^t, α^t and $p^t = 0$, the state variables of the next time step, $t + 1$, can be calculated using Eq.(16) or (17). Now if

$$|\{C_2\}^T \{\Gamma\}^{t+1} + \{C_1\}^T \{\Gamma\}^t| \leq \overline{M}_d$$

then $p = 0$; otherwise the computational code is time marched using the previous state as the set of initial conditions until the system achieves a steady state. It is noted that the transient time histories computed here are for very light (zero moment of inertia) wings and hence they are not shown as they are of little physical interest. Later studies will incorporate realistic moments of inertia.

Figure 10 shows the steady state rolling rate vs flow velocity and a comparison of theory and experiment for a certain combination of leading and trailing edge control surface rotations, i.e. zero leading edge control surface rotation, $r=0$, and the flexible torsional stiffness case. Note that two theoretical results are shown, with (solid line) and without (broken line) the dry friction of the spindle support mechanism included. The symbols of Δ and \circ points are results obtained from the experiment. The \circ points show the results when increasing flow velocity and the Δ points are for when decreasing flow velocity. The above two experimental results are very close except for the flow velocity at which rolling starts when increasing flow velocity or stops when decreasing flow velocity. The starting flow velocity is about $U_d=10.3$ m/s and the stopping flow velocity is about 5.4 m/s. This difference is because there is an inertial rolling moment when the flow velocity is decreasing and the wing is still rolling. From this figure it is seen that the theoretical reversal flow velocity is in a range from $U = 21.5 \rightarrow 25$ m/s for dry friction damping included, and at a point velocity at $U = 23.6$ m/s for no dry friction damping included. The experimental reversal flow velocity is also in a range from $U = 21.6 \rightarrow 24$ m/s for increasing flow velocity, and $U = 21.5 \rightarrow 23.7$ m/s for decreasing flow velocity.

Figure 11 shows the corresponding rolling rate vs flow velocity for the rigid torsional stiffness case. The lines and symbols shown in this figure (and following figures) are the

same as for Figure 10. Accounting for the dry friction improves the quantitative agreement between theory and experiment both for the rigid and flexible torsional stiffness cases.

Figure 12 shows the rolling rate vs flow velocity for $r=1$ and the flexible torsional stiffness case. The experimental starting flow velocity is about $U_d=7.5$ m/s and the stopping flow velocity is about 5.2 m/s. From this figure it is also seen that the theoretical reversal flow velocity is in a range from $U = 25 \rightarrow 27$ m/s for dry friction damping included, and a point velocity at $U = 26.5$ m/s for no dry friction damping included. These are higher than those for $r=0$ case. The experimental reversal flow velocity is also in a range from $U = 26.5 \rightarrow 27.6$ m/s for both increasing and decreasing flow velocity. A similar result is shown in Figure 13 for the rigid torsional stiffness case.

Figure 14 and Fig.15 show the rolling rate vs flow velocity for $r=-1$ for the flexible and the rigid torsional stiffness cases, respectively. The experimental starting flow velocity is about $U_d=12$ m/s. The theoretical reversal flow velocity is from $U = 19 \rightarrow 23$ m/s for dry friction damping included, and a point velocity at $U = 21.5$ m/s for no dry friction damping included. The experimental reversal flow velocity is from $U = 17.2 \rightarrow 21$ m/s for increasing flow velocity. The difference between the experimental data for increasing and decreasing flow velocity is larger for $r=-1$ than for $r=0$ or $+1$ due to smaller rolling rate, i.e. there is a smaller aerodynamic rolling moment relative to the dry friction damping moment. For decreasing flow velocity, the stopping flow velocity is at 19.1 m/s. For the rigid torsional stiffness case, as shown in Figure 15, the agreement between theory and experiment is closer because the aerodynamic rolling moment is more dominant relative to the dry friction damping moment.

To more clearly show the effects of the parameter, r , on the reversal flow velocity and rolling rate, $\frac{p^l}{U}$, a summary of data from Fig.10-15 is shown in Figure 16 and Fig. 17. Figure 16 shows the rolling rate vs flow velocity for $r=-1, 0$ and 1 , and the flexible torsional stiffness case. Figure 17 shows the corresponding rolling rate vs flow velocity for the rigid torsional stiffness case. Comparing Figure 16 to Figure 7 or Figure 9, it is found the reversal flow velocity decreases as r decreases both theoretically and experimentally.

Concluding Remarks

The generally good agreement between theory and experiment is encouraging and perhaps even a bit of a pleasant surprise. It is encouraging because it confirms that the adaptive use of a combination of leading and trailing edge control surfaces can lead to substantially

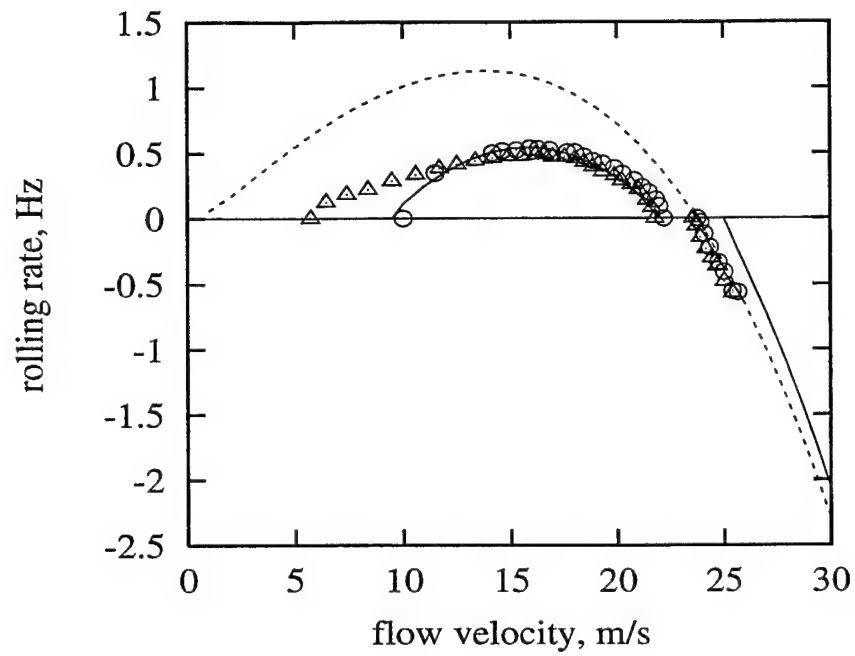


Figure 10: Rolling rate vs flow velocity: Comparison of theory and experiment for $r=0$, and with flexible torsional stiffness. Two theoretical results are shown, with (solid line) and without (broken line) the dry friction of the spindle support mechanism included. Two experimental results are shown, the \circ points show the results for the increasing flow velocity and the \triangle points for decreasing flow velocity.

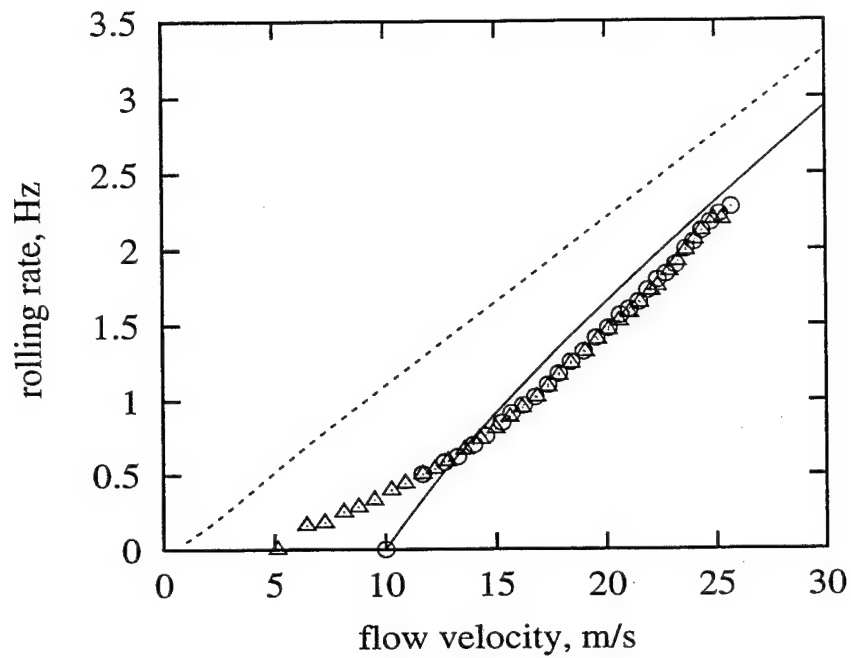


Figure 11: Rolling rate vs flow velocity: Comparison of theory and experiment for $r=0$, and with rigid torsional stiffness.

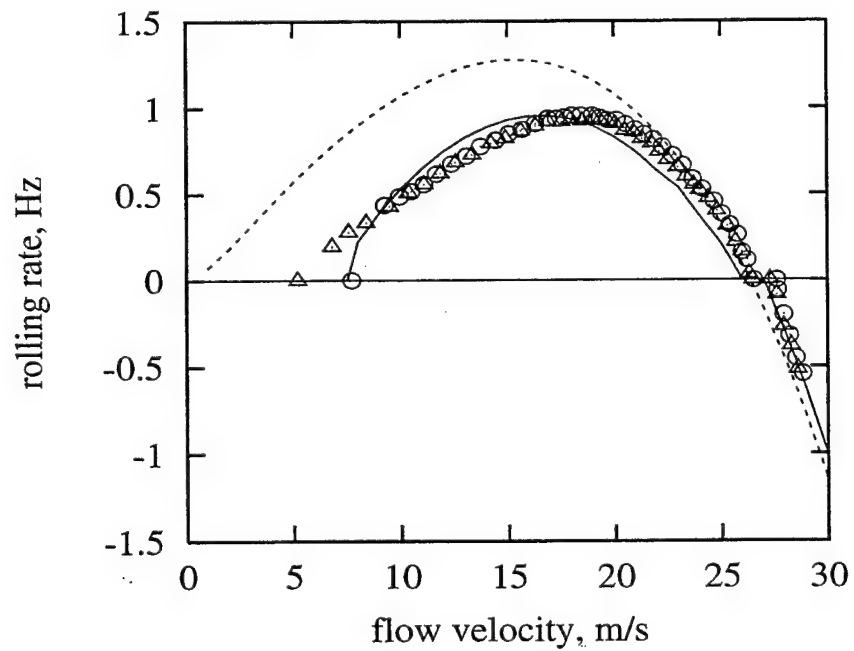


Figure 12: Rolling rate vs flow velocity: Comparison of theory and experiment for $r=1$, and with flexible torsional stiffness.

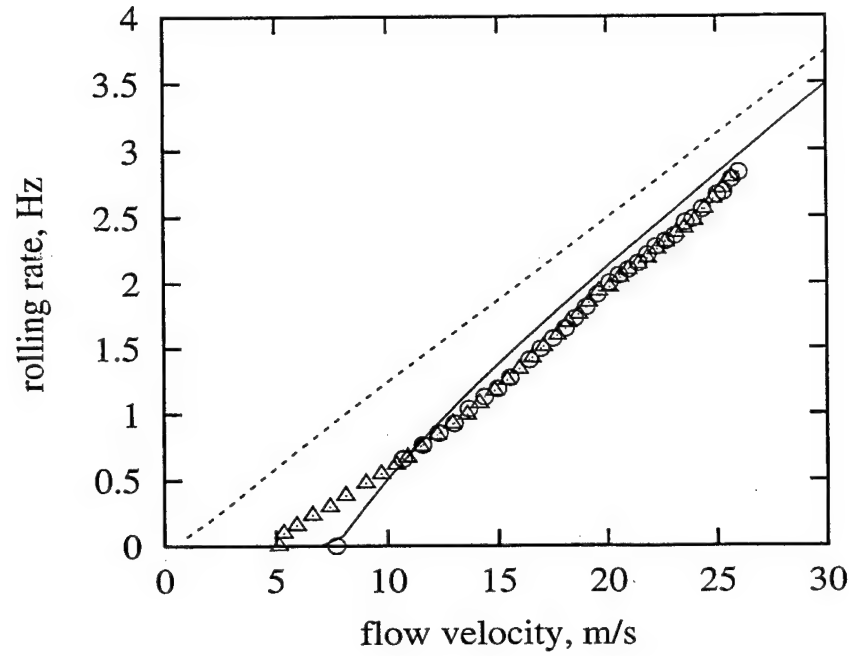


Figure 13: Rolling rate vs flow velocity: Comparison of theory and experiment for $r=1$, and with rigid torsional stiffness.

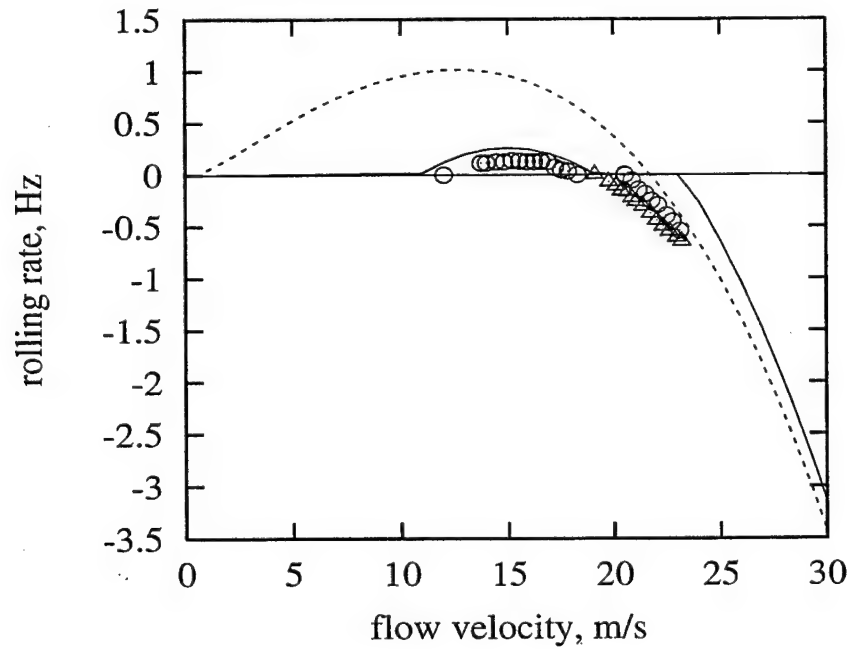


Figure 14: Rolling rate vs flow velocity: Comparison of theory and experiment for $r=-1$, and with flexible torsional stiffness.

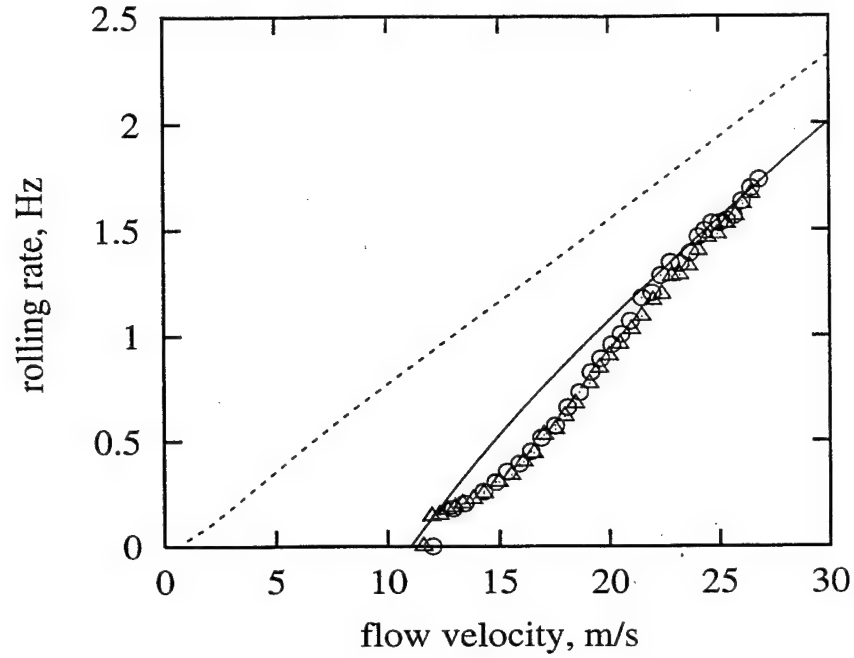


Figure 15: Rolling rate vs flow velocity: Comparison of theory and experiment for $r = -1$, and with rigid torsional stiffness.

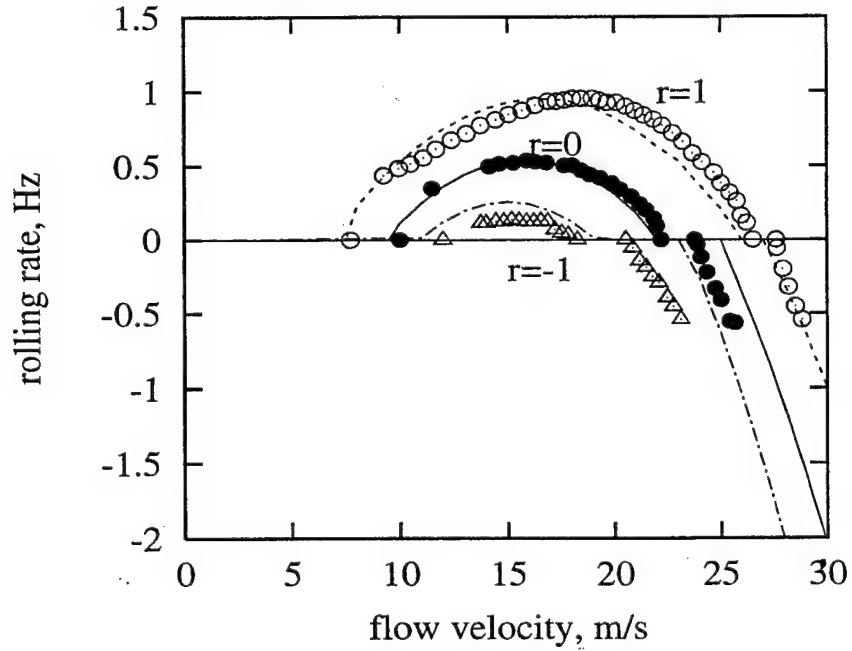


Figure 16: Rolling rate vs flow velocity: Comparison of theory and experiment for $r = -1, 0$ and 1, and with flexible torsional stiffness.

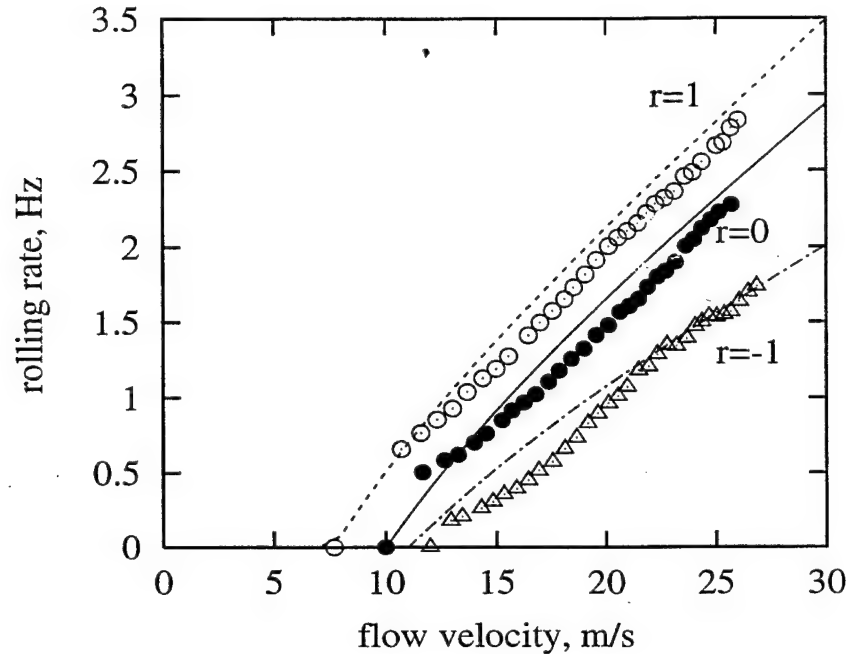


Figure 17: Rolling rate vs flow velocity: Comparison of theory and experiment for $r = -1, 0$ and 1 , and with rigid torsional stiffness.

improved rolling performance in aerospacecraft and by implication enhanced performance for other maneuvers as well.

It should be emphasized that to obtain good quantitative agreement between theory and experiment it was necessary to model the nonlinear dry friction damping at the interface between the wing experimental model and its support mounting. In a freely flying model such dry friction would not be present of course.

The good agreement between theory and experiment may also be a bit surprising for those who have been aware that often the prediction of aerodynamic characteristics of control surfaces has been found to be deficient relative to measured values. While direct measurements of the aerodynamic characteristics of the leading and trailing edge control surfaces have not been made here, nevertheless the very good agreement between theory and experiment for rolling rates as a function of dynamic pressure suggests that our theoretical aerodynamic model has been more than adequate to predict the aerodynamic performance of the control surfaces. This may be because for the present experimental model there is no gap between the wing and the control surfaces that would lead to leakage flows. On the other hand viscous effects per se, which are often cited as a possible source of disagreement between measured

and computed values, must not be significant here even though the Reynolds' number based upon total wing chord is only about 136000 for $U=20$ m/s.

Finally a few words about possible next steps. Even though we have used time marching simulation to compute the steady state rolling performance, the present experimental/theoretical study is essentially for static equilibrium conditions. It will be of considerable interest to extend the theoretical and experimental work to dynamic, transient conditions. Such a study is planned and preliminary work is underway.

Acknowledgments

This work was supported by DARPA through AFOSR Grant F49620-99-1-00253, "Aeroelastic Leveraging and Control Through Adaptive Structures", under the direction of Dr. Ephraim Garcia and Dr. Dan Segalman. Dr. Robert Clark is the Duke University Principal Investigator. All numerical calculations were done on a supercomputer, T916, in the North Carolina Supercomputing Center (NCSC).

REFERENCES

1. Bisplinghoff, R.L., Ashley, H. and Halfman, R.L., "*Aeroelasticity*," Addison-Wesley, 1955. Also available in a Dover Edition.
2. Dowell, E.H., Crawley, E.F., Curtiss, H.C., Jr., Peters, D.A., Scanlan, R.H. and Sisto, F., "*A Modern Course in Aeroelasticity*", Kluwer Publishers, Third Edition, 1995.
3. Noll, T. E. and Eastep, F. E., "Active Flexible Wing Program", *Journal of Aircraft*, Vol. 32, No. 1, January-February, 1995, pg. 9.
4. Andersen, G., Forster, E., Kolonay, R. and Eastep, F., "Multiple Control Surface Utilization in Active Aeroelastic Wing Technology", *Journal of Aircraft*, Vol. 34, No. 4, July-August, 1997, pp.552-557.
5. Zink, P. S., Mavis, D.N., Love, M. H. and Karpel, M., "Robust Design for Aeroelastically Tailored /Active Aeroelastic Wing", 7th AIAA/USAF/NASA/ SSMO Symposium on Multidisciplinary Analysis and Optimization, St. Louis, MO, September 2-4, 1998. AIAA

Paper 98-4781.

6. Weisshaar, T.A., Duke, D.K. and Dobbins, A., "Active Aeroelastic Tailoring With Adaptive Continuous Control Surfaces", AIAA Paper 2000-1619.

7. Flick, P.M and Love, M. H., "The Impact of Active Aeroelastic Wing Technology on Conceptual Aircraft Design", Paper Presented at the RTO AVT Specialists Meeting on "Structural Aspects of Flexible Aircraft Control", Ottawa, Canada, October 18-20,1999. RTO MP-36.

8. Yurkovich, R. R., "Optimum Wing Shape for an Active Flexible Wing", Proceedings of the AIAA/ASME/ASCE/ARS 36th Structures, Structural Dynamics and Materials Conference, New Orleans, LA, 1995.

9. Dowell, E.H., Bliss D.B. and Clark, R.L., "An Adaptive Aeroelastic Wing with Leading and Trailing Edge Control Surfaces," submitted for publication, 2001.

10. Prechtel, E. F., and Hall, S. R. (1999). "Design of a High Efficiency, Large Stroke, Electromechanical Actuator," *Journal of Smart Materials and Structures*, 8(1), pp 13-30.

11. Ardilean, E., and Clark, R. L. (2001). "V-stack Piezoelectric Actuator", SPIE 8th Annual International Symposium on Smart Structures and Materials, 4-8 March, Newport Beach, CA.

12. Dowell, E.H. and Hall, K.C., " Modeling of Fluid-Structure Interaction," *Annual Review of Fluid Mechanics*, 2001, Vol.33, pp. 445-490.

13. Katz, Joseph and Plotkin, Allen, *Low-Speed Aerodynamics* , McGraw-Hill, Inc. 1991, p297.

14. Tang, D.M. and Dowell, E.H., "Effects of Angle of Attack on Nonlinear Flutter of A Delta Wing", *AIAA Journal*, Vol.39, No. 1, 2001, pp. 15-21.

15. Kuethe, A.M. and Chow, C.-Y., " *Foundations of Aerodynamics: Bases of Aerodynamic Design* " , Wiley, New York, 1986.

Transient Response Study on Rolling Effectiveness of Multiple Control Surfaces

Demian Tang ¹, Aiqin Li ² and Earl H. Dowell ³
Duke University, Durham, North Carolina 27708-0300

ABSTRACT

In the present paper, a transient response study of the effectiveness of trailing and leading edge control surfaces has been made for a rolling wing-fuselage model. An experimental model and wind tunnel test are used to assess the theoretical results. The theoretical model includes the inherently nonlinear dry friction damping moment that is present between the spindle support and the experimental aeroelastic wing model. The roll trim equation of motion and the appropriate aeroelastic equations are solved for different combinations of leading and trailing edge control surface rotations using a reduced order aerodynamic model based upon the fluid eigenmodes of three dimensional vortex lattice aerodynamic theory. The present paper provides new insights into the transient dynamic behavior and design of an adaptive aeroelastic wing using trailing and leading edge control surfaces.

¹Research Associate Professor, Department of Mechanical Engineering and Materials Science

²Research Assistant, Department of Mechanical Engineering and Materials Science

³J. A. Jones Professor, Department of Mechanical Engineering and Materials Science and Director of the Center for Nonlinear and Complex Systems. Dean Emeritus, Pratt School of Engineering

Ref. 4
has been
submitted
for publication

NOMENCLATURE

A, B	vortex lattice aerodynamic coefficient matrices
c	wing chord (including the leading and trailing control surface chords)
I_α, I_ϕ	torsional and rolling inertias, respectively
M_d	Coulomb friction damping moment coefficient
km, kn	numbers of vortex elements on wing in x -, y - directions, respectively
kmm	total number of vortices on both the wing and wake in the x - direction
K_α	torsional stiffness of the wing
l	wing span
p	rolling rate
p_s	static or steady state rolling rate
r	$\equiv \frac{\eta_{le}}{\eta_{te}}$
R_a	degrees of freedom of reduced order aerodynamic model
t	time
U	airspeed
x, y	streamwise and spanwise coordinates
X, Y	right and left eigenvector matrices of vortex lattice eigenvalue model
Z	eigenvalue matrix of vortex lattice aerodynamic model
α	twist angle of the wing
ϕ	rolling angle
ξ	damping coefficient
Γ	the vortex strength
Δt	the time step, $\Delta x/U$
Δx	$\equiv \frac{c}{km}$
ρ_∞	air density
η_{le}, η_{te}	rotational angle of leading and trailing control surfaces
$()$	$d()/dt$

Introduction

Some interesting results reported from the Active Flexible Wing (AFW) program [1] and more recent work [2-6] on Active Aeroelastic Wing (AAW) technology have shown that

an appropriately chosen combination of leading and trailing edge control surface deflections plus an adaptive control law can be used to achieve improved rolling performance and/or to minimize roll maneuver loads. As reported previously [7,8], the same conceptual benefit that can be obtained by using an adaptive torsional stiffness change can also be realized by using an adaptive aeroelastic wing with the gearing ratio between leading and trailing edge control surfaces programmed to change with flight dynamic pressure. Also some new actuation technologies are currently under development for high-bandwidth actuator, leveraging high energy density materials such as piezoceramics. Two such actuation technologies include the X-frame actuator developed at MIT [9] and the V-stack actuator developed at Duke University [10]. Thus, implementation of an adaptive aeroelastic wing with leading and trailing edge control surfaces appears promising.

Reference [7] considered theoretically the basic adaptive concept and the fundamental physical phenomena for two models, (1) an airfoil and (2) a rolling wing. The theoretical results have been validated by subsequent experimental work [8]. In Ref.[8], a wind tunnel wing-fuselage model with leading and trailing edge control surfaces has been designed and tested to measure the steady state rolling effectiveness vs flow velocity for different combination of leading and trailing edge control surface rotation. Time marching simulation has been used to compute the steady state rolling performance, but the experimental/theoretical study was essentially for static equilibrium conditions. A three dimensional incompressible (linear) vortex lattice aerodynamic theory and a corresponding reduced order aerodynamic model was used in [7,8] and in the present analysis, see [11]. Steady state results for subsonic, compressible flow can be obtained using the Prandtl-Glauert scaling law. It is noted that for the wind tunnel test model, there is a nonlinear dry friction damping arising from the rubbing or sliding between the experimental aeroelastic wing-fuselage model and the support spindle. This nonlinear factor is considered in the experimental-theoretical correlation study.

Extending the work of [7,8], dynamic, transient conditions are considered in the present paper. A dynamic roll trim equation of motion of the wing-fuselage model with multiple control surfaces has been derived including aeroelastic effects and solved using a time marching technique. The capabilities of multiple control surfaces to effect roll maneuver transient response of the wing-fuselage model with a torsionally flexible wing are examined theoretically and experimentally. These results provide new insights into the dynamic behavior and design of an adaptive aeroelastic wing using trailing and leading edge control surfaces.

Experimental Model and Measurements

The experimental model consists of a right and left wing and a fuselage (slender body). For simplicity, the wing model is a rectangular aluminum plate of thickness 0.317 cm, total chord length (c) of 10.16 cm (including the leading and trailing control surface chords) and span length (l) of 10.16 cm. The plate has a very large bending and torsional stiffness and thus the wing per se is assumed to be rigid. The torsional flexibility of the wing is provided by a flat spring at the wing root which can be adjusted. The elastic axis is placed at the quarter of the wing chord. In order to place the chordwise center of gravity axis of the wing at the elastic axis as well, the leading edge control surface is made of brass and the trailing control surface is made of aluminum plate. Also a small slender body mounted at the wing root is used to provide weight balance. The leading and trailing control surfaces each have a chord length of 1.73 cm (17% c) and a full span length of 10.16 cm (100% l) hinged on the leading and trailing edges, respectively. The rotation angle of each control surface can be adjusted.

The fuselage has a circular cross-section with a diameter of 2.54 cm. It includes two parts. The front part is a slender body with a parabolic forebody which can rotate about the fuselage center axis and supports the wings. The rear part is a non-rotating slender body with a parabolic aftbody which is used to support the front portion of the slender body and is connected to the wind tunnel floor by a support or sting rod. See Figure 1.

The wings are allowed to rotate (roll) about the center axis of the fuselage. The start and stop mechanism for the rotation is provided by an electrical magnet brake. The transient rolling state (rolling angle) is measured by an Optical Shaft Encoder, E11, with 500 pulses per revolution mounted on the rear end of the non-rotating portion of the slender body. Every pulse corresponds to a certain rolling angle. But the time duration for one pulse may be changed during the experiment.

Note that in the experimental testing protocol, the control surfaces are at a fixed rotation and the magnetic brake is used to prevent roll until a steady state aerodynamic field and aeroelastic deformation is achieved. Then the brake is released and the rolling transient is observed and measured.

A physical representation of wing model geometry along with a three-dimensional vortex lattice model (linear) of the unsteady flow is shown in Figure 1 and a photograph of the

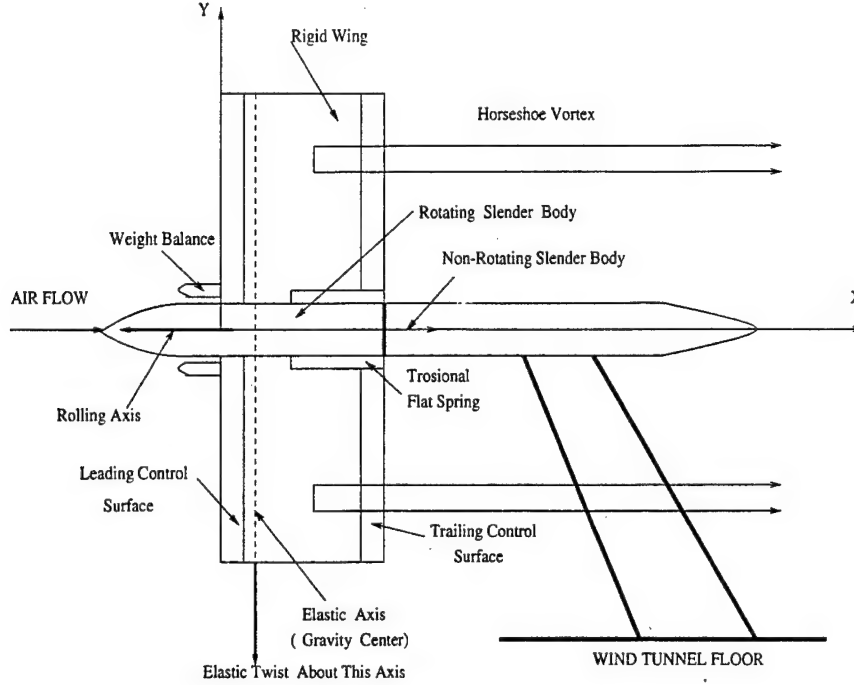


Figure 1: Physical representation of experimental model. Also shown is a three-dimensional (linear) vortex lattice model of the unsteady flow.

aeroelastic model in the wind tunnel is shown in Figure 2.

Dynamic Aeroelastic Theoretical Model

As shown in Figure 1, a straight rectangular wing with leading and trailing edge control surfaces that are full span is considered. The theoretical/experimental model is symmetrical about the center axis of the fuselage. The aerodynamic forces on the fuselage (slender body) are neglected. The dynamic equation of torsional equilibrium about the elastic axis of the rigid wing expresses the balance of moments about the elastic axis due to the elastic spring and the aerodynamic forces in the Eulerian coordinate system (x,y,z) .

$$I_\alpha \ddot{\alpha} + K_\alpha \alpha + M_y = 0 \quad (1)$$

OR

$$I_\alpha \ddot{\alpha} + K_\alpha \alpha + \int_{r_f}^{l+r_f} \int_0^c \Delta p(x,y)(x-x_e) dx dy = 0 \quad (2)$$

where $\Delta p(x,y)$ is the pressure distribution on the wing, x_e is the distance from the elastic center to leading edge of the wing, I_α and K_α are the torsional inertia and stiffness, and α is the twist angle of the wing. r_f is the radius of the slender body (fuselage).

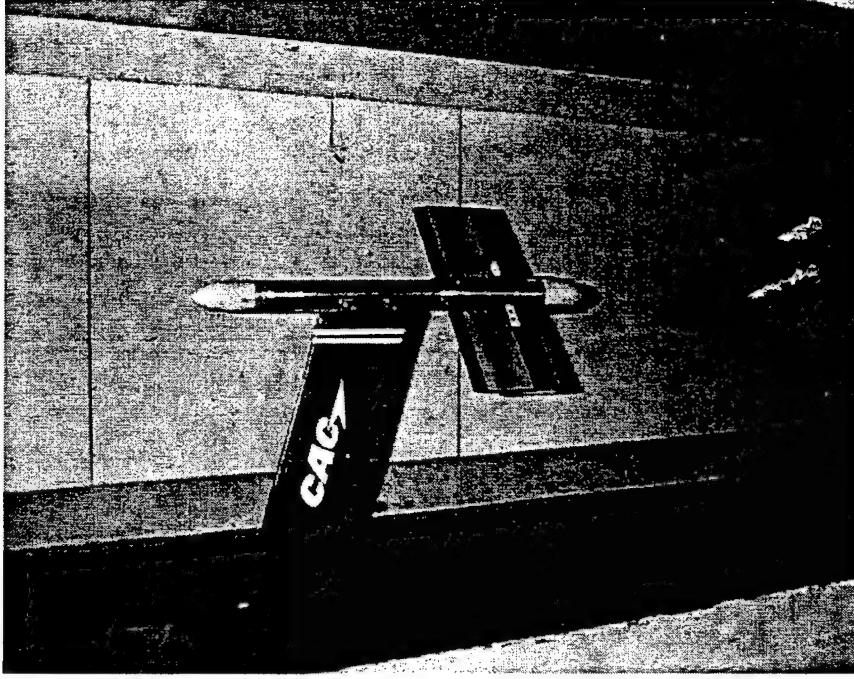


Figure 2: Photograph of the aeroelastic model in the wind tunnel.

The rigid body dynamic rolling equation of equilibrium about the center axis of the fuselage is expressed as follows.

$$I_\phi \ddot{\phi} + M_d \frac{\phi}{|\phi|} - \int_{r_f}^{l+r_f} L y dy = 0 \quad (3)$$

or

$$I_\phi \ddot{\phi} + M_d \frac{\phi}{|\phi|} - \int_{r_f}^{l+r_f} y \int_0^c \Delta p(x, y) dx dy = 0 \quad (4)$$

In this equation a dry friction damping moment between the spindle support and the aeroelastic wing model is taken into account. I_ϕ is the rolling inertia and ϕ is the wing rolling angle. M_d is the nonlinear Coulomb friction damping moment coefficient

Introducing non-dimensional quantities into Eq.(2) and (4) as follows,

$$\overline{\Delta p}(x, y) = \frac{\Delta p(x, y)}{\rho U^2} \quad , \quad \overline{x} = \frac{x}{c} \quad , \quad \overline{x}_e = \frac{x_e}{c} \quad , \quad \overline{y} = \frac{y}{c}$$

$$\overline{I}_\alpha = \frac{I_\alpha}{\rho U^2 c^3} \quad , \quad \overline{I}_\phi = \frac{I_\phi}{\rho U^2 c^3} \quad , \quad \overline{K}_\alpha = \frac{K_\alpha}{\rho U^2 c^3} \quad \text{and} \quad \overline{M}_d = \frac{M_d}{\rho U^2 c^3}$$

the dimensionless equations corresponding to Eq.(2) and (4) are

$$\overline{I}_\alpha \ddot{\alpha} + \overline{K}_\alpha \alpha + \int_{r_f/c}^{(l+r_f)/c} \int_0^1 \overline{\Delta p}(\overline{x}, \overline{y}) (\overline{x} - \overline{x}_e) d\overline{x} d\overline{y} = 0 \quad (5)$$

and

$$\bar{I}_\phi \ddot{\phi} + \bar{M}_d \frac{\phi}{|\phi|} - \int_{r_f/c}^{(l+r_f)/c} \bar{y} \int_0^1 \bar{\Delta p}(\bar{x}, \bar{y}) d\bar{x} d\bar{y} = 0 \quad (6)$$

To model the above aeroelastic structural/fluid system, the aerodynamic flow about the structural model is assumed to be incompressible, inviscid and irrotational. Here an unsteady (linear) vortex lattice method is used to describe this flow. The wing and wake are divided into a number of elements. In the wake and on the wing all the elements are of equal size, dx , in the streamwise direction. Point vortices are placed on the wing and in the wake at the quarter chord of the elements. At the three-quarter chord of each panel element a collocation point is placed for the downwash, i.e. the velocity induced by the discrete vortices is required to be equal to the downwash arising from the unsteady motion of the wing. Thus the following relationship is obtained,

$$w_i^{t+1} = \sum_j^{kmm} K_{ij} \Gamma_j^{t+1}, \quad i = 1, \dots, km \quad (7)$$

where w_i^{t+1} is the dimensionless downwash at the i th collocation point at time step $t + 1$, Γ_j is the j th vortex strength normalized by cU , and K_{ij} is an aerodynamic kernel function for the horseshoe vortex. km and kmm are the number of vortex elements on the wing and total number of vortices on both the wing and wake in the x -direction, respectively. For the three-dimensional incompressible flow, the kernel function is given by

$$K_{ij}(\bar{x}, \bar{y}, \bar{x}_a, \bar{y}_a, \bar{x}_b, \bar{y}_b) = \frac{-1}{4\pi(\bar{y}_i - \bar{y}_{ja})} \left[1 + \frac{\sqrt{(\bar{x}_i - \bar{x}_{ja})^2 (\bar{y}_i - \bar{y}_{ja})^2}}{\bar{x}_i - \bar{x}_{ja}} \right] \quad (8)$$

$$+ \frac{1}{4\pi(\bar{y}_i - \bar{y}_{jb})} \left[1 + \frac{\sqrt{(\bar{x}_i - \bar{x}_{ja})^2 + (\bar{y}_i - \bar{y}_{jb})^2}}{\bar{x}_i - \bar{x}_{ja}} \right]$$

where \bar{x}_i is the location of the i th collocation point, and \bar{y}_{ja} and \bar{y}_{jb} are the locations of the two j th trailing vortex segments which are parallel to the x axis at $\bar{y} = \bar{y}_a$ and $\bar{y} = \bar{y}_b$.

The aerodynamic matrix equation (general) is given by

$$[A]\{\Gamma\}^{t+1} + [B]\{\Gamma\}^t = [T]\{w\}^{t+1} \quad (9)$$

where $[A]$ and $[B]$ are aerodynamic coefficient matrices. $[T]$ is a transfer matrix for determining the relationship between the global vortex lattice mesh and the local vortex lattice mesh on the wing. For the present model the wing span is finite and anti-symmetric about the center axis of the fuselage. An anti-symmetric vortex condition is used for reducing

the aerodynamic degrees of freedom. In this case the aerodynamic coefficient matrix, $[A]$, corresponding to the kernel function can be expressed as

$$A = K_{i,j}(\bar{x}, \bar{y}, \bar{x}_a, \bar{y}_a, \bar{x}_b, \bar{y}_b) - K_{i,j}(\bar{x}, \bar{y}, \bar{x}_b, -\bar{y}_b, \bar{x}_a, -\bar{y}_a)$$

The nondimensional downwash, w , contains contributions from the steady angle of attack α , the wing rolling rate, $p \equiv \frac{d\phi}{dt}$, and rotational angles, η_{le}, η_{te} of the leading and trailing control surfaces, respectively. For the present model, Eq.(9) is expressed in matrix form as

$$[A]\{\Gamma\}^{t+1} + [B]\{\Gamma\}^t = \{T_\alpha\}\alpha^{t+1} - \{T_p\}\frac{p^{t+1}}{U} + \{T_t\}\eta_{te} + \{T_l\}\eta_{le} \quad (10)$$

where $\{T_\alpha\}$ and $\{T_p\}$ are the elastic twist and rolling rate transfer matrices for determining the relationship between the global vortex lattice mesh and the local vortex lattice mesh on the wing. $\{T_t\}$ and $\{T_l\}$ are the transfer matrices for determining the relationship between the global vortex lattice mesh and the local vortex lattice mesh on the trailing and leading control surfaces, respectively.

The nondimensional pressure distribution on the rigid wing at the j th point is given by

$$\overline{\Delta p_j} = \frac{c}{\Delta x} [(\Gamma_j^{t+1} + \Gamma_j^t)/2 + \sum_i^j (\Gamma_i^{t+1} - \Gamma_i^t)] \quad (11)$$

Substituting Eq.(11) into Eq.(5) gives

$$\bar{I}_\alpha \ddot{\alpha} + \bar{K}_\alpha \alpha + \sum_{n=1}^{kn} \sum_{m=1}^{km} (\bar{x}_m - \bar{x}_e) [(\Gamma_{nm}^{t+1} + \Gamma_{nm}^t)/2 + \sum_i^m (\Gamma_{ni}^{t+1} - \Gamma_{ni}^t)] \Delta \bar{y} = 0 \quad (12)$$

or as expressed in matrix form,

$$\bar{I}_\alpha \ddot{\alpha} + \bar{K}_\alpha \alpha + \{D_2\}^T \{\Gamma\}^{t+1} + \{D_1\}^T \{\Gamma\}^t = 0 \quad (13)$$

where kn and km are the chordwise and spanwise numbers of vortex elements on the wing and here the superscript T indicates the matrix transpose.

Substituting Eq.(11) into Eq.(6) gives

$$\bar{I}_\phi \ddot{\phi} + \bar{M}_d \frac{\phi}{|\phi|} - \left\{ \sum_{n=1}^{kn} \bar{y}_n \sum_{m=1}^{km} [(\Gamma_{nm}^{t+1} + \Gamma_{nm}^t)/2 + \sum_i^m (\Gamma_{ni}^{t+1} - \Gamma_{ni}^t)] \right\} \Delta \bar{y} = 0 \quad (14)$$

or as expressed in matrix form,

$$\bar{I}_\phi \ddot{\phi} + \bar{M}_d \frac{\phi}{|\phi|} - \{C_2\}^T \{\Gamma\}^{t+1} - \{C_1\}^T \{\Gamma\}^t = 0 \quad (15)$$

where D_1, D_2, C_1 and C_2 are coefficient matrices describing the vortex element forces and moments on the wing.

Thus, combining Eq.(10),(13) and (15), a complete static aeroelastic state-space equation in matrix form is obtained for the unknown variables, Γ , α and ϕ .

$$\begin{bmatrix} A & 0 & T_p/U & -T_\alpha & 0 \\ D_2^T & & & & \\ -C_2^T & [K_2] & & & \\ 0 & & & & \\ 0 & & & & \end{bmatrix} \begin{Bmatrix} \Gamma \\ \dot{\alpha} \\ \dot{\phi} \\ \alpha \\ \phi \end{Bmatrix}^{t+1} + \begin{bmatrix} B & 0 & 0 & 0 & 0 \\ D_1^T & & & & \\ -C_1^T & [K_1] & & & \\ 0 & & & & \\ 0 & & & & \end{bmatrix} \begin{Bmatrix} \Gamma \\ \dot{\alpha} \\ \dot{\phi} \\ \alpha \\ \phi \end{Bmatrix}^t = \begin{Bmatrix} T_t \eta_{te} + T_l \eta_{le} \\ 0 \\ -\overline{M}_d \frac{\phi}{|\phi|} \\ 0 \\ 0 \end{Bmatrix}^{t+\frac{1}{2}} \quad (16)$$

Following a similar treatment as described in Ref.[12], a reduced order aerodynamic model with static correction is constructed and the final aeroelastic state space model is given by

$$\begin{bmatrix} I & -Y_{Ra}^T [I - A(A+B)^{-1}] E \\ G_2 X_{Ra} & K_2 + G_2 (A+B)^{-1} E \end{bmatrix} \begin{Bmatrix} \gamma \\ \theta \end{Bmatrix}^{t+1} + \begin{bmatrix} -Z_{Ra} & Y_{Ra}^T B (A+B)^{-1} E \\ G_1 X_{Ra} & K_1 + G_1 (A+B)^{-1} E \end{bmatrix} \begin{Bmatrix} \gamma \\ \theta \end{Bmatrix}^t = \begin{Bmatrix} 0 \\ -(G_1 + G_2)(A+B)^{-1} (T_t \eta_{te} + T_l \eta_{le}) + F_N \end{Bmatrix}^{t+\frac{1}{2}} \quad (17)$$

where where $\{\theta\} = \{\dot{\alpha}, \dot{\phi}, \alpha, \phi\}$ is a vector of unknown variables and

$$[E] = [0, \{-T_p/U\}, \{T_\alpha\}, 0], \quad [G_2] = \begin{bmatrix} \{D_2\}^T \\ -\{C_2\}^T \\ 0 \\ 0 \end{bmatrix}, \quad [G_1] = \begin{bmatrix} \{D_1\}^T \\ -\{C_1\}^T \\ 0 \\ 0 \end{bmatrix}$$

$$[K_2] = \begin{bmatrix} \overline{I}_\alpha/\Delta t & 0 & \overline{K}_\alpha/2 & 0 \\ 0 & \overline{I}_\phi/\Delta t & 0 & 0 \\ -1/2 & 0 & 1/\Delta t & 0 \\ 0 & -1/2 & 0 & 1/\Delta t \end{bmatrix}$$

$$[K_1] = \begin{bmatrix} -\overline{I}_\alpha/\Delta t & 0 & \overline{K}_\alpha/2 & 0 \\ 0 & -\overline{I}_\phi/\Delta t & 0 & 0 \\ -1/2 & 0 & -1/\Delta t & 0 \\ 0 & -1/2 & 0 & -1/\Delta t \end{bmatrix}, \quad \{F_N\} = \begin{Bmatrix} 0 \\ -\overline{M}_d \frac{\phi}{|\phi|} \\ 0 \\ 0 \end{Bmatrix} \quad (18)$$

$[X_{Ra}], [Y_{Ra}]$ are the reduced right and left eigenvector matrices of the vortex lattice aerodynamic model and $[Z_{Ra}]$ is a reduced aerodynamic eigenvalue matrix, $\Gamma = X_{Ra}\gamma$, with only the most dominant eigenmodes retained in the analysis.

Numerical Study

A standard discrete time marching algorithm has been used to calculate the dynamic response of this aeroelastic system using the full aerodynamic model, Eq.(16), and also the reduced order aerodynamic model, Eq.(17). The time step is constant for a given flow velocity U , $\Delta t = \Delta x/U$. For these calculations, the parameters of an experimental model studied here and in Ref.[8] are used. The measured torsional and rolling inertia moments are $I_\alpha = 8.22 \times 10^{-6} \text{kgms}^2$ and $I_\phi = 8.95 \times 10^{-5} \text{kgms}^2$ for $r=0$ or $I_\phi = 8.78 \times 10^{-5} \text{kgms}^2$ for $r=1$ or $r=-1$, respectively. The leading edge device for $r=0$ is (slightly) different from that for $r=\pm 1$ hence the difference in values for I_ϕ . The measured torsional stiffness is $K_\alpha=0.032 \text{kgm/rad}$. The trailing edge control surface rotation is $\eta_{te} = 5^\circ$. Two typical cases for leading edge control are considered, i.e. the ratios of leading to trailing edge control surface rotations are $r=0$ and 1. The measured dry friction damping moment between the spindle support and the aeroelastic wing model is $M_d=0.00021 \text{kgm}$.

Consider now the present three dimensional flow model for the wing. The wing was modeled using 400 vortex elements, i.e, $km=40$, $kn=10$. The wake was modeled using 800 vortex elements, i.e, $kmm=120$. The total number of vortex elements (or aerodynamic degrees of freedom) was 1200. The aerodynamic eigenmodes are extracted from this model and a small number, $R_a=11$, are used in the aeroelastic analysis. A convergence study has shown that $R_a=11$ is sufficient to give good accuracy.

Figure 3(a) shows the transient response of rolling rate, p , for $U=25 \text{ m/s}$, $r=1$ and $M_d = 0$ (Note that $p \equiv \dot{\phi}$). The initial conditions for ϕ and α are zero. There are three curves in this figure for three distinct cases. When both torsional and rolling inertia moments are considered the response is indicated by the broken line. This is a rising oscillatory curve. The aeroelastic oscillatory frequency is near the torsional natural frequency $\omega_\alpha = 10 \text{Hz}$. (Note that the oscillatory frequency varies with the flow velocity). When only the rolling inertia is considered and the torsional inertia neglected, ($I_\alpha = 0$), the response is indicated by the solid line. This is similar to a unit-step response of a first-order system. One of the important characteristics of this response is an exponential response function and convergence to a

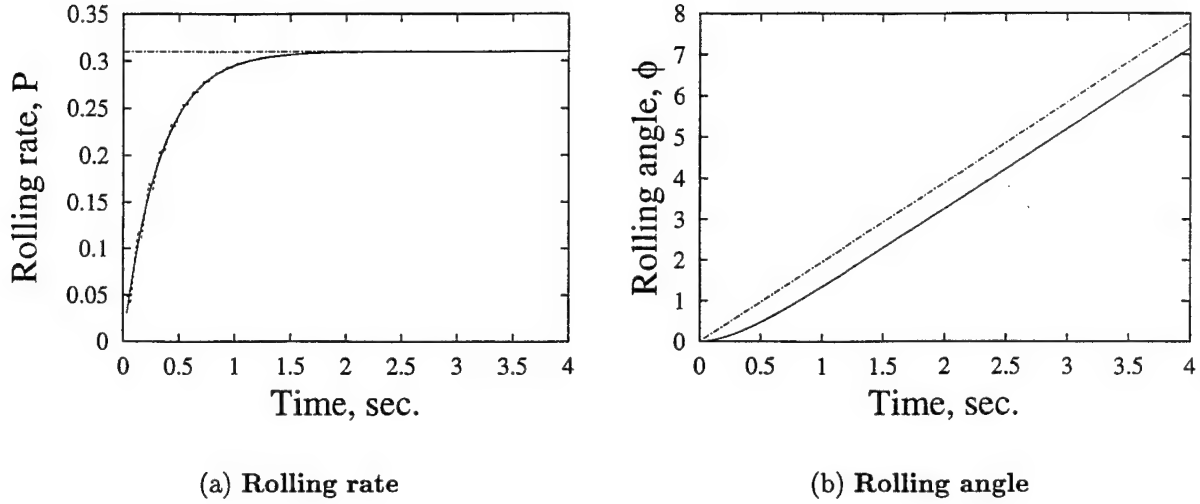


Figure 3: Transient response for $u=25$ m/s and $r=1$.

steady value. For reference, the static rolling rate for both $I_\alpha = 0$ and $I_\phi = 0$ is shown by the dashed-point line. Figure 3(b) shows the transient response of the rolling angle, ϕ . The response is almost the same with and without torsional inertia included as shown by the broken and solid lines. There is a difference between the dynamic and static response for the rolling angle and this difference is constant when the steady state is reached. The value of the rolling angle is dependent on the rolling inertia and system damping. The rolling rate for both the transient dynamic and static or steady state response is the same when the steady state is reached.

Examining the solid line curve of the figure 3, the transient response of this system can be described approximately by an exponential function, i.e.

$$p(t) = p_s(1 - e^{-\xi t}) \quad (t \geq 0) \quad (19)$$

where p_s is a static rolling rate and ξ is a damping coefficient.

A curve fitting method is used to determined the damping coefficient from data such as that shown in Fig.3. Figure 4 shows a typical transient response time history and the corresponding fitted data for $U=15$ m/s, $r=1$ and $M_d = 0$. The time history and static rolling rate (steady value) are indicated by the solid line. The fitted data is indicated by the symbol of \circ . From these data a settling time, t_s can be defined. The settling time is the time required for the response curve to reach within a certain range of the steady (static) value, say within 5%. This 5% tolerance criterion may be useful for studies of rolling rate

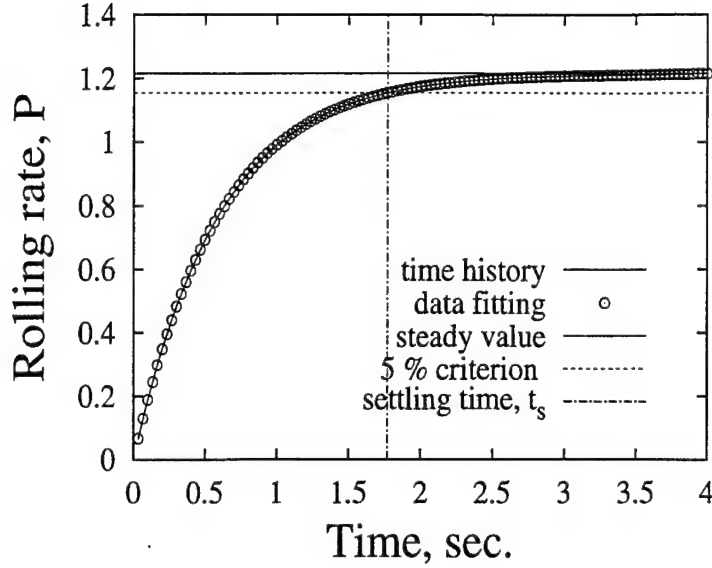


Figure 4: Transient response time history and corresponding the fitted data for $u=15$ m/s and $r=1$.

control. For the present conditions, t_s is 1.7 seconds as indicated by a dashed-point line.

Figure 5 shows the transient response of the rolling rate for three flow velocities $U=15, 27$ and 30 m/s for $r=1$, $I_\alpha = 0$. The solid line is for the case of $M_d = 0$ and the broken line is for the case of $M_d = 0.00021$ kgm. For $U=15$ and 30 m/s, the initial rolling rate is zero and the transient responses have the expected exponential response behavior. The rolling rate with dry friction damping is smaller than that without dry friction damping. For $U=27$ m/s, the initial rolling rate is set to 1 Hz, thus a difference between with and without dry friction damping cases can be more readily seen. At this velocity, the steady rolling rate is $p=0$ with dry friction damping included. In this case, the response does not have an exponential response behavior.

Figure 6(a) and 6(b) show the system damping, ξ , and settling time, t_s , vs flow velocity for $r=1$, $I_\alpha = 0$. The solid line with the points, \circ , is for the case of $M_d = 0$ and the broken line with the points, \triangle , is for the case of $M_d = 0.00021$ kgm. The results are obtained using a data fitting method. As shown in Figure 6(a), for the case of $M_d = 0.00021$ kgm, there are some missing points for $U < 7.5$ m/s and 25 m/s $< U < 28$ m/s, because in these ranges the steady rolling rates are zero due to the effects of dry friction. The damping increases as the flow velocity increases and the damping is almost independent of dry friction damping over most, but not all, of the flow velocity range. This means the system damping, ξ , is

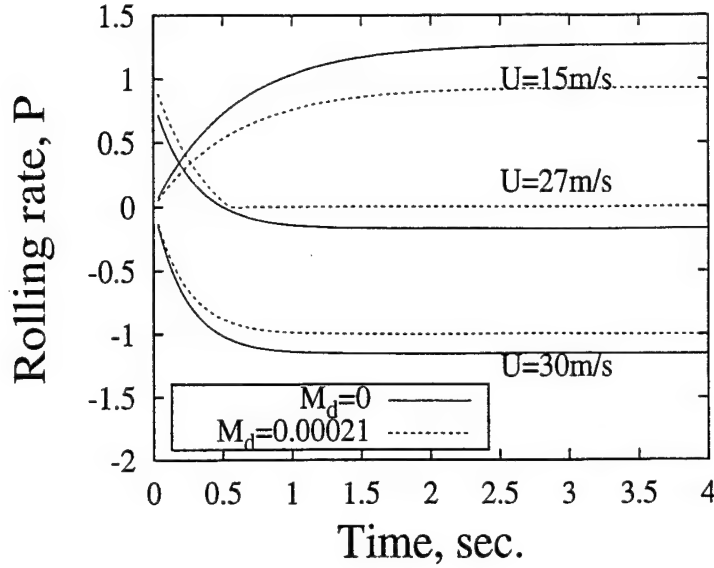
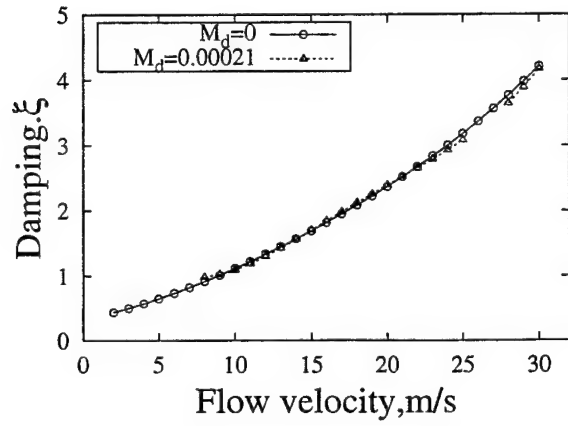


Figure 5: Transient response curves for $U=15, 27, 30$ m/s and $r=1$.

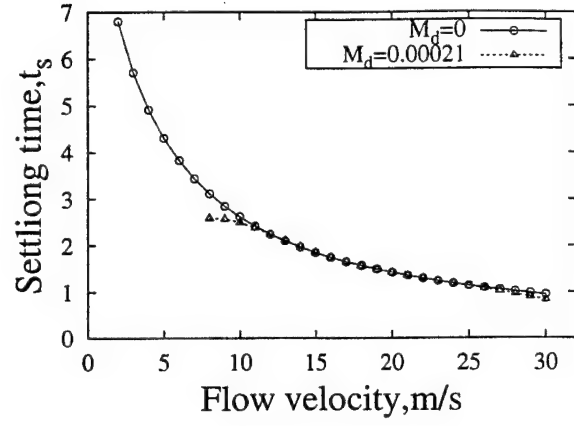
generally dominated by the aerodynamic damping. As shown in Figure 6(b), the settling time, t_s , decreases as the flow velocity increases.

Similar results are obtained for $r=0$ as will be shown later. It is interesting to note that the system damping, ξ , and settling time, t_s , are very close to those for $r=1$, i.e. the effects of r on the aerodynamic damping and t_s are very small.

Now consider the rigid wing case, i.e. the torsional stiffness is infinite, $K_\alpha = \infty$. Figure 7 shows the transient response of the rolling rate for two typical flow velocities $U=6, 18$ m/s, $r=1$ and $I_\alpha = 0$. The solid line is for the case of $M_d = 0$ and the broken line is for the case of $M_d = 0.00021$ kgm. For $U=18$ m/s, the initial rolling rate is zero and the transient responses have an exponential response behavior. The rolling rate with dry friction damping is smaller than that without dry friction damping. For $U=6$ m/s, the initial rolling rate is set to 1 Hz and the transient response of the rolling rate with dry friction damping approaches zero when $t > 2.7$ seconds. It does not have an exponential response behavior. Figure 8(a) and 8(b) show the system damping, ξ , and settling time, t_s , vs flow velocity for $r=1$, $I_\alpha = 0$. The lines and symbols have the same meaning as in Figure 6. The results are similar to those for the torsionally elastic case, but the damping values are different. Structural torsional stiffness has a larger effect on the aerodynamic damping than the control surface rotation



(a) System damping



(b) Settling time

Figure 6: System damping, ξ , and settling time, t_s , vs flow velocity for $r=1$.

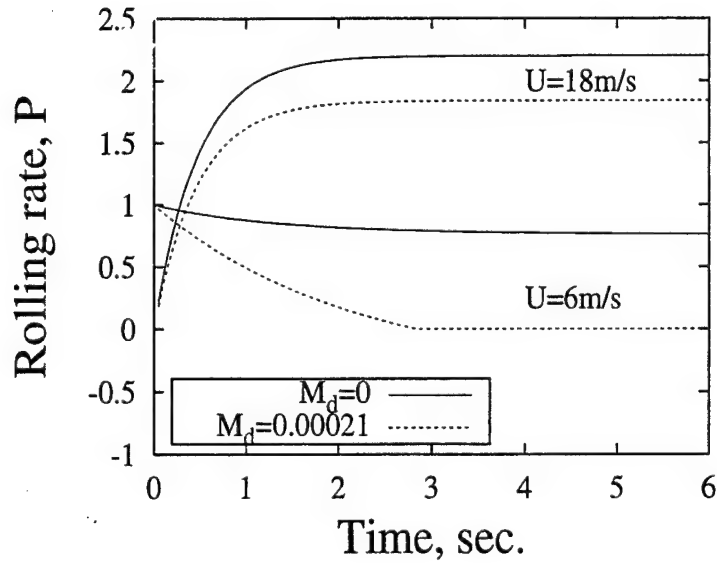


Figure 7: Transient response curves for the rigid case for $U=6, 18$ m/s and $r=1$.

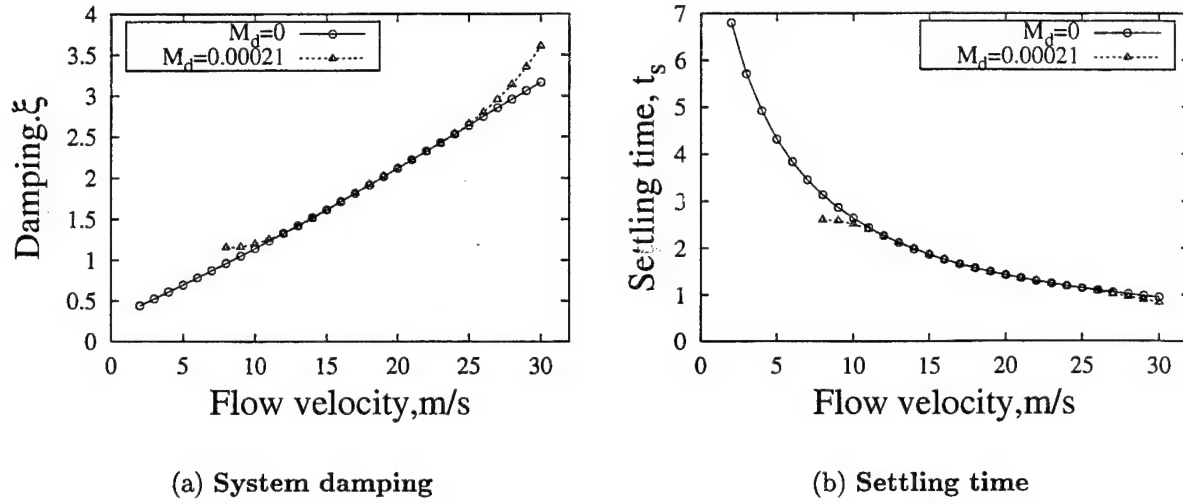


Figure 8: System damping, ξ and settling time, t_s vs flow velocity for the rigid case and $r=1$.

angles, r .

Figure 9(a) shows the transient response when increasing or decreasing flow velocity. The calculation model is a torsional elastic system with only the rolling inertia moment included for $r=1$ and $M_d = 0.00021$ kgm. The solid line is for increasing flow velocity and the broken line is for decreasing flow velocity. There are eight (8) flow velocities considered in the calculation from $U=9$ m/s to 30 m/s with $\Delta U=3$ m/s when flow velocity is increasing and $U=27$ m/s to 6 m/s with $\Delta U=3$ m/s when it is decreasing. The calculation starts from the increasing flow velocity case with zero initial rolling rate. At each flow velocity, the computation is for 4 seconds. The computational time step, Δt , is $1/2048$ seconds. The transient response is shown in time intervals of four (4) seconds for each flow velocity increment. For the next flow velocity (increasing ΔU), initial conditions are provided by the previous transient response state. This process is continuous in time until the flow velocity increases to $U=30$ m/s. For the decreasing velocity process, initial conditions are provided by the last transient response of $U=30$ m/s to calculate the transient response of $U=27$ m/s. This process is continuous in time until the flow velocity decreases to $U=6$ m/s.

Figure 9(b) shows a typical transient response for the increasing and decreasing flow velocity cases from $U=18$ m/s to 21 m/s and from $U=21$ m/s to 18 m/s, respectively. The solid line is the result from the time history and the broken line is the result from a data fitting. The system damping is $\xi=1.17$ for $U=21$ m/s and the increasing velocity case, and

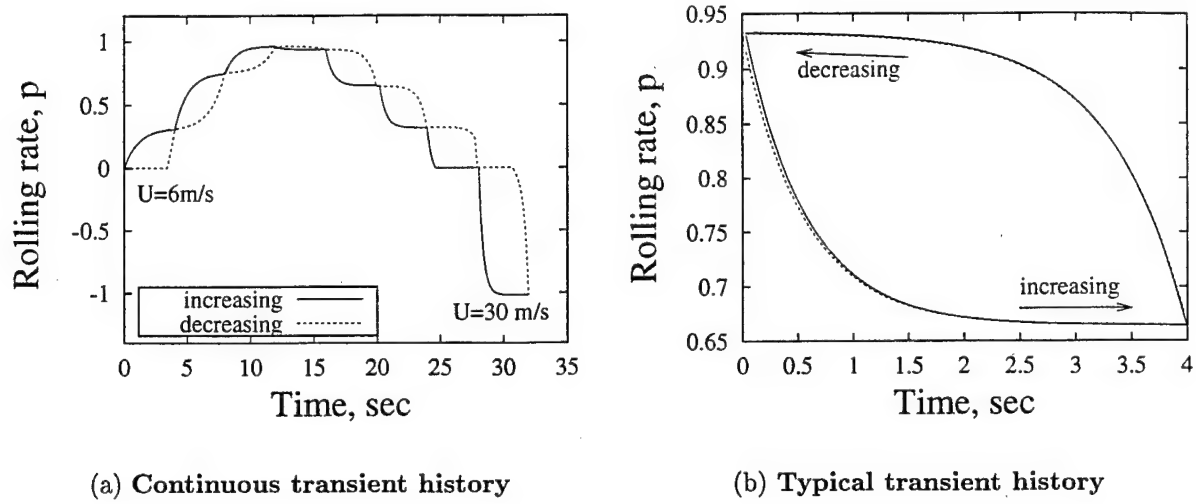


Figure 9: Transient time history for the increasing and decreasing flow velocities for $r=1$ and $M_d = 0.00021$ kgm.

$\xi=1.4$ for $U=18$ m/s and the decreasing velocity case.

Corresponding to Fig.9, Figure 10(a) and 10(b) show the system damping, ξ , and settling time, t_s , vs flow velocity. The symbol, \circ , is the result from the increasing flow velocity process and the symbol, Δ , is the result from the decreasing flow velocity process. Note that at $U=6$ and 27 m/s, one cannot calculate the damping value, ξ , using the present data fitting method because of the discontinuous change in slope of the rolling rate as a function of time due to dry friction effects. See Fig.7. The two results from the increasing and decreasing flow velocity cases are very close. No detectable hysteresis phenomenon was found from the theoretical model, even though the effects of dry friction damping are included.

Theoretical and Experimental Correlation

For the present computational and experimental model, the aerodynamic and structural parameters are described in the previous Section, "Experimental Model and Measurements". The trailing edge control surface rotation is $\eta_{te} = 5^\circ$. Two typical cases are considered in the experiment, i.e. the ratios of leading to trailing edge control surface rotations are $r=0$ and $r=1$.

From the experiment measurement, a time series of 500 pulses is obtained as shown in

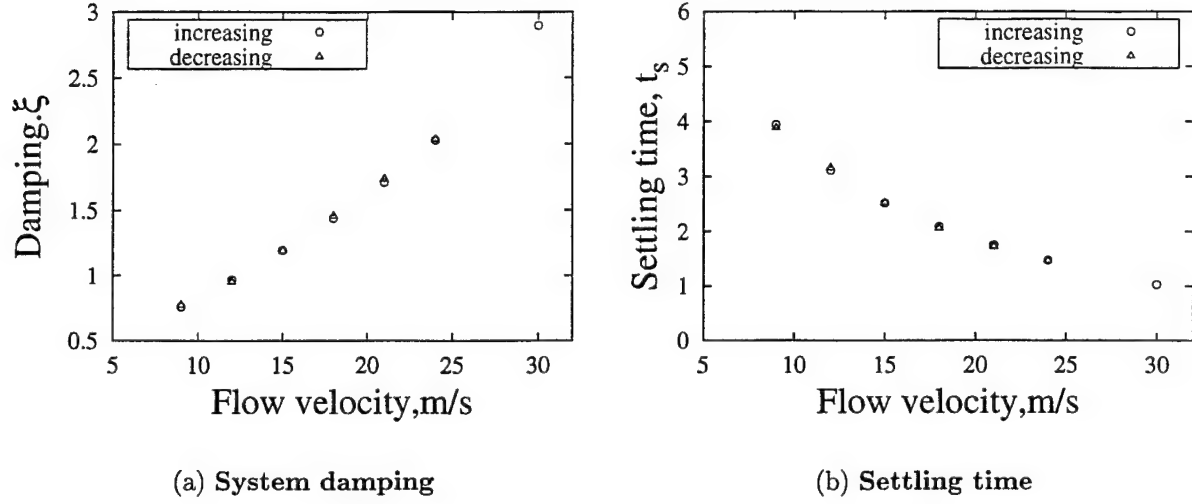


Figure 10: System damping, ξ , and settling time, t_s , vs flow velocity for $r=1$. $M_d = 0.00021$ kgm and $K_\alpha=0.032$ kgm/rad.

Figure 11. $t_0, t_1, \dots, t_i, \dots, t_n$ in the figure are the time sequence. Thus, the rolling angle at t_1 is $\frac{2\pi}{500}$ rad and at t_i , the rolling angle is represented as

$$\phi = i \frac{2\pi}{500} \quad (20)$$

As an example, Figure 12 (a) shows the measured data from Encoder transducer, E11, for $U=14.83$ m/s for the case of $r=1$ and the flexible wing. Because the measured data do not provide an exact square wave, an average pulse voltage is calculated as shown by the dashed line of Figure 12(a). The pulse time sequence t_i is then determined using an intersection point of the i^{th} pulse with the average line. The corresponding rolling angle can be determined using Eq.(20). The results are shown in Figure 12(b).

A curve fitting method is then used to determine the damping coefficient, ξ , and the steady rolling rate, P . This method is similar to that used in the theoretical analysis. The transient rolling rate is determined by a numerical differentiation method from the measured rolling angle data.

Figure 13 shows the transient response history and a comparison of theory with experiment for $U=14.83$ m/s for the case of $r=1$ and the flexible wing. The solid line shows the results from theoretical analysis and the symbols, \bullet , are the results obtained from the experiment. The experiment is repeated over ten times. All the experimental results are shown

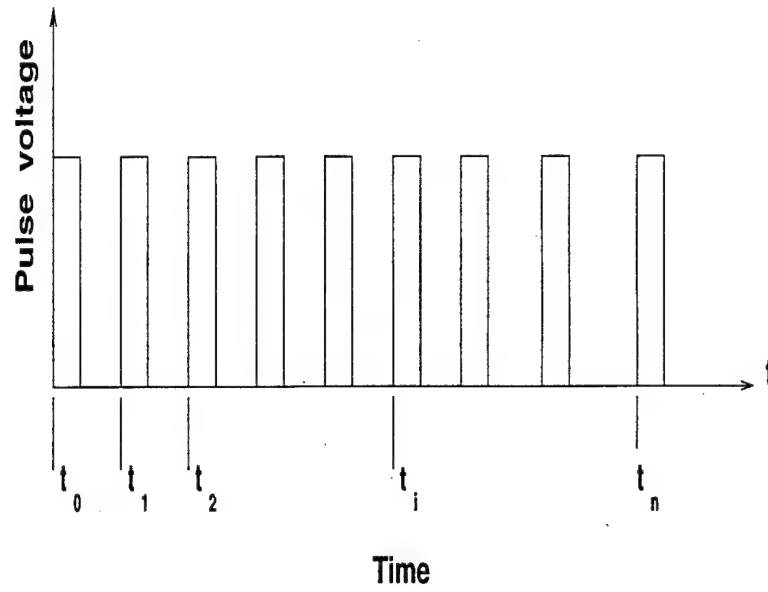
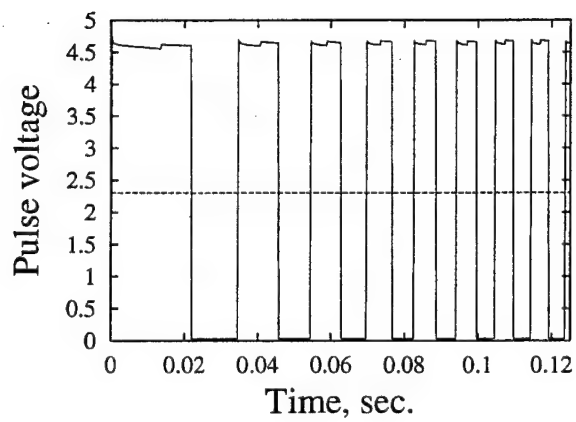
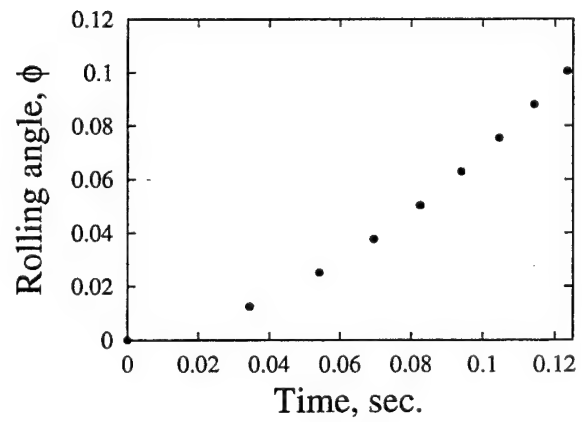


Figure 11: Diagram for pulses obtained from Encoder, E11



(a) Pulses



(b) Rolling Angle

Figure 12: Pulses and corresponding rolling angle for $u=14.83$ m/s and $r=1$.

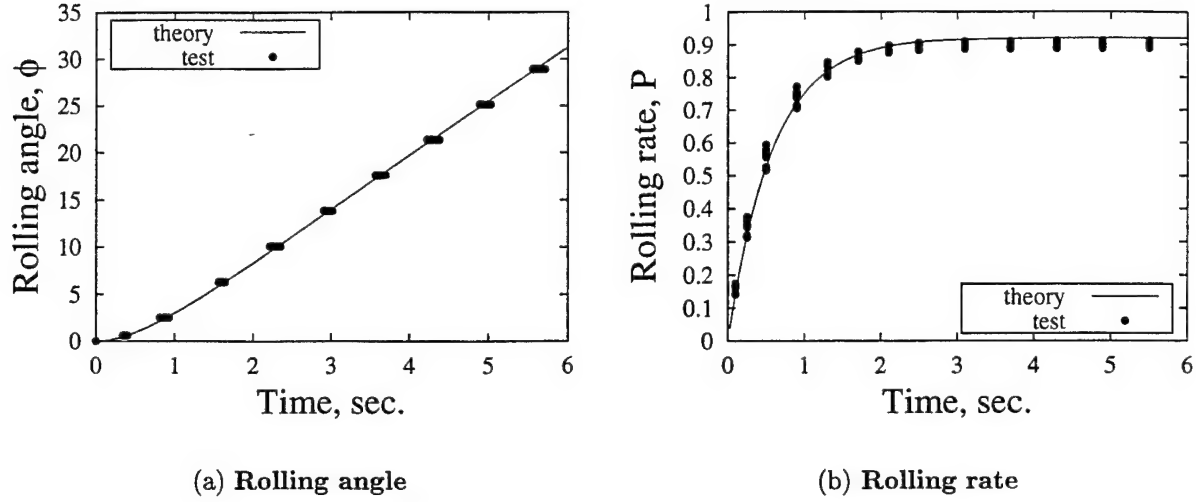


Figure 13: Transient response for $u=14.83$ m/s and $r=1$.

in Figure 13. Figure 13 (a) shows the transient response of rolling angle, ϕ . Note that for a particular rolling angle, the pulse time is slightly different for each test run. Figure 13 (b) shows the transient response for the rolling rate, p . Theoretical and experimental results are in good agreement.

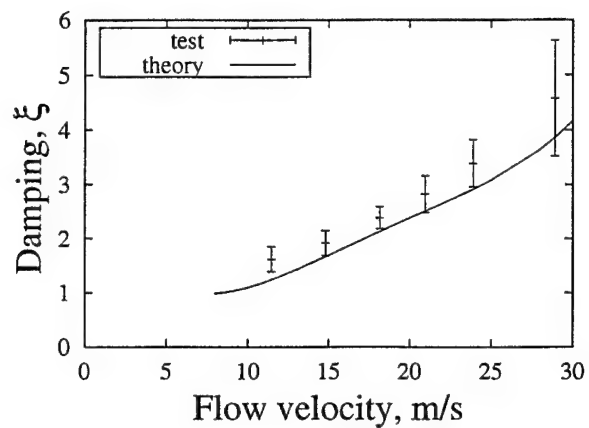
Because the damping coefficient, ξ , is very sensitive to the measurement error, ten tests for each case are used in the present measurement. The mean value and error tolerance of the damping coefficient are then calculated. Figure 14(a) and 14 (b) show the system damping, ξ , and settling time, t_s , vs flow velocity for $r=1$ and the flexible wing. The solid line shows the theoretical results and the bars show the experiment data including measurement uncertainty. The agreement between theory and experiment is reasonably good.

Similar results are obtained for $r=0$ as shown in Figure 15. The line and symbols shown in this figure are the same as for Figure 14.

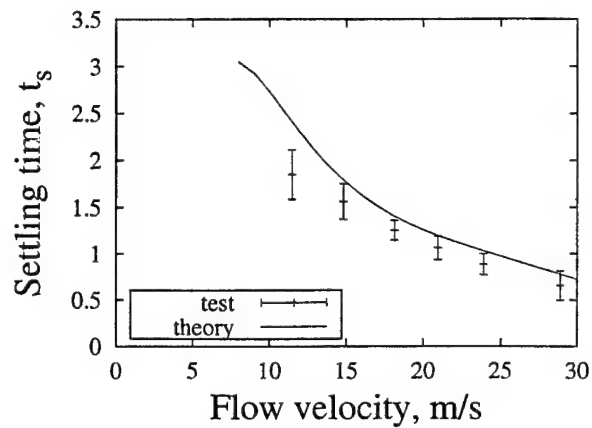
Figure 16 shows the transient response for $r=1$ and the rigid wing. The solid line indicates the theoretical results and the dashed line is for experimental data. The agreement is again good.

Concluding Remarks

An experimental/theoretical correlation study for transient response of a rolling aeroe-

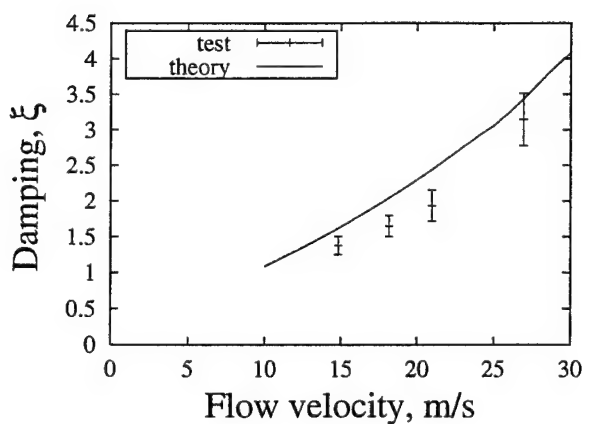


(a) System damping

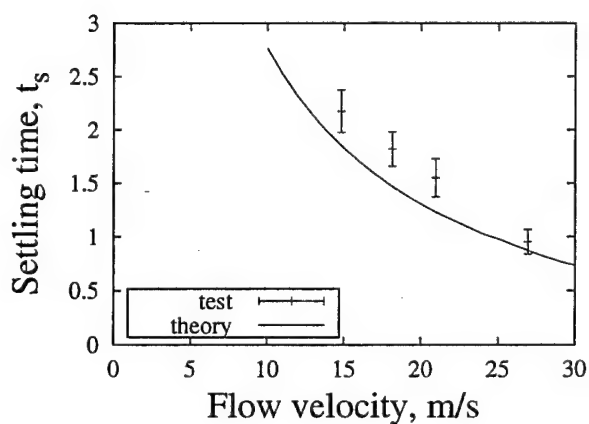


(b) Settling time

Figure 14: System damping, ξ , and settling time, t_s , vs flow velocity for $r=1$.



(a) System damping



(b) Settling time

Figure 15: System damping, ξ , and settling time, t_s , vs flow velocity for $r=0$.

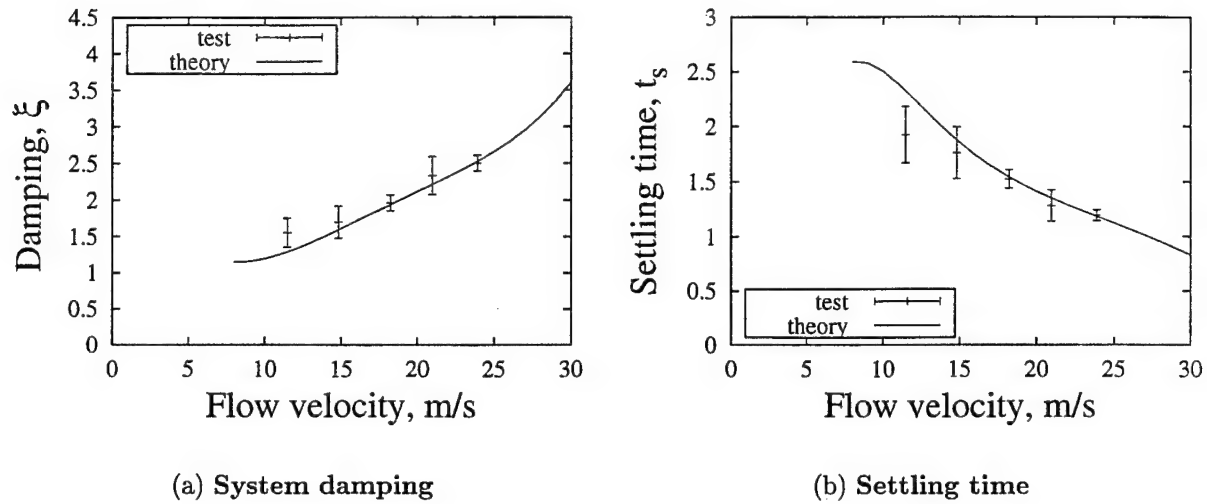


Figure 16: System damping, ξ , and settling time, t_s , vs flow velocity for the rigid case and $r=1$.

lastic wing with leading and trailing edge control surfaces has been carried out. Good correlation between theory and experiment is shown. The transient behavior shows no unusual or unexpected anomalies suggesting that state-of-the-art theoretical methods may be used with confidence for analysis and design.

Acknowledgments

This work was supported by DARPA through AFOSR Grant F49620-99-1-00253, "Aeroelastic Leveraging and Control Through Adaptive Structures", under the direction of Dr. Ephraim Garcia and Dr. Dan Segalman. Dr. Robert Clark is the Duke University Principal Investigator. All numerical calculations were done on a supercomputer, T916, in the North Carolina Supercomputing Center (NCSC).

References

1. Noll, T. E. and Eastep, F. E., "Active Flexible Wing Program", *Journal of Aircraft*, Vol. 32, No. 1, January-February, 1995, pg. 9.
2. Andersen, G., Forster, E., Kolonay, R. and Eastep, F., "Multiple Control Surface Utilization in Active Aeroelastic Wing Technology", *Journal of Aircraft*, Vol. 34, No. 4, July-

August, 1997, pp.552-557.

3. Zink, P. S., Mavis, D.N., Love, M. H. and Karpel, M., "Robust Design for Aeroelastically Tailored /Active Aeroelastic Wing", 7th AIAA/USAF/NASA/SSMO Symposium on Multidisciplinary Analysis and Optimization, St. Louis, MO, September 2-4, 1998. AIAA Paper 98-4781.
4. Weisshaar, T.A., Duke, D.K. and Dobbins, A., "Active Aeroelastic Tailoring With Adaptive Continuous Control Surfaces", AIAA Paper 2000-1619.
5. Flick, P.M and Love, M. H., "The Impact of Active Aeroelastic Wing Technology on Conceptual Aircraft Design", Paper Presented at the RTO AVT Specialists Meeting on "Structural Aspects of Flexible Aircraft Control", Ottawa, Canada, October 18-20,1999. RTO MP-36.
6. Yurkovich, R. R., "Optimum Wing Shape for an Active Flexible Wing", Proceedings of the AIAA/ASME/ASCE/ARS 36th Structures, Structural Dynamics and Materials Conference, New Orleans, LA, 1995.
- ✓7. Dowell, E.H., Bliss D.B. and Clark, R.L., "An Adaptive Aeroelastic Wing with Leading and Trailing Edge Control Surfaces," submitted to *AIAA Journal* for publication, 2001.
- ✓8. Tang, D.M., Aiqin Li and Dowell, E.H., " Experimental and Theoretical Study on Rolling Effectiveness of Multiple Control Surfaces," submitted to *AIAA Journal* for publication, 2001.
9. Precht, E. F., and Hall, S. R. (1999). "Design of a High Efficiency, Large Stroke, Electromechanical Actuator," *Journal of Smart Materials and Structures*, 8(1), pp 13-30.
10. Ardilean, E., and Clark, R. L. (2001). "V-stack Piezoelectric Actuator", SPIE 8th Annual International Symposium on Smart Structures and Materials, 4-8 March, Newport Beach, CA.
11. Dowell, E.H. and Hall, K.C., " Modeling of Fluid-Structure Interaction," *Annual Review of Fluid Mechanics*, 2001, Vol.33, pp. 445-490.
12. Tang, D.M. and Dowell, E.H., "Effects of Angle of Attack on Nonlinear Flutter of A Delta Wing", *AIAA Journal*, Vol.39, No. 1, 2001, pp. 15-21.

V-Stack Piezoelectric Actuator

(Patent Pending, Duke University file # OST 1847)

Emil V. Ardelean and Robert L. Clark
*Pratt School of Engineering,
Mechanical Engineering and Material Science Department,
Duke University, Durham, NC 27708, USA*

ABSTRACT

Aeroelastic control of wings by means of a distributed, trailing-edge control surface is of interest with regards to maneuvers, gust alleviation, and flutter suppression. The use of high energy density, piezoelectric materials as motors provides an appealing solution to this problem. A comparative analysis of the state of the art actuators is currently being conducted. A new piezoelectric actuator design is presented. This actuator meets the requirements for trailing edge flap actuation in both stroke and force. It is compact, simple, sturdy, and leverages stroke geometrically with minimum force penalties while displaying linearity over a wide range of stroke. The "V-Stack Piezoelectric Actuator," consists of a base, a lever, two piezoelectric stacks, and a pre-tensioning element. The work is performed alternately by the two stacks, placed on both sides of the lever. Pre-tensioning can be readily applied using a torque wrench, obviating the need for elastic elements and this is for the benefit of the stiffness of the actuator. The characteristics of the actuator are easily modified by changing the base or the stacks. A prototype was constructed and tested experimentally to validate the theoretical model.

Keywords: actuator, stack, piezoelectric, stroke, leverage, aeroelastic

1. INTRODUCTION

Modern dynamic systems require actuation schemes that should be fast, precise, powerful and produce large displacements. The actuation of trailing edge control surfaces (flaps) for the control of High Aspect Ratio (HAR) wings of Uninhabited Aerial Vehicles (UAV), or helicopter rotors, fits into this category. Given the electro-mechanical nature of the piezoceramics, piezoelectric actuators can be easily included in mechanical structures, hence piezoceramics are candidates for transduction in these systems. Piezoceramics are active materials which exhibit remarkable high energy density, low hysteresis, high temperature stability and high bandwidth. Usually, they are capable of producing high forces but low displacement. Using piezoelectric benders, one can obtain “large” displacement, but the compliance of such devices is significant and this makes them useless for high bandwidth actuation schemes. Given the mentioned characteristics, the need for stroke amplification devices arises. Lately, quite a bit of effort was put into designing and constructing such devices (Prechtel and Hall, 1998, 1999; Hal and Spangler, 1995; Chandra and Chopra, 1998; Koratkar and Chopra, 2000; etc.) Very good results were obtained with the *X-frame actuator* (Prechtel and Hall, 1998, 1999).

The goal of our current research at Duke University, is to develop an adaptive HAR wing. One problem for this kind of wing is flutter, which occurs at relatively low flow speed (approx. 32 m/s), limiting performance of UAVs. The flutter frequency is lower than 25 Hz. Here, we present the early development of a new actuator, that will be suited

for flutter alleviation of the HAR wings by actuating discrete trailing edge flaps, distributed along the span of the wing.

Considering the data obtained by Tang and Dowel (Tang and Dowell 2001), the requirements for this actuator are: Bandwidth of the actuator-flap system exceeding 25 Hz. The maximum moment on the flap hinge (worse case scenario) is 2.1 Nm, which means a maximum force of 300 N at the actuator output. It should be light and compact, to fit inside the structure of the wing without significantly affecting it. It should be capable of $\pm 6^\circ$ deflection of the flap. The functional principle is simple and is based on geometrical amplification of stroke (stroke leveraging), using two piezostacks that work complimentary (while one expands, producing useful force/work, the other shortens and allows displacement).

2. ACTUATOR CONSTRUCTION AND FUNCTIONALITY

2.1 Actuator design

A CAD (Solid Works) model of the prototype, which was built, is presented in Figure 1.

As can be seen, the concept is quite simple.

Base, 1, is an ideally rigid part, and is meant to support the whole mechanism, and to serve for attachment of the actuator to the housing structure. The base material should be light, for good mass efficiency, should have a high Young's modulus and should be wear

resistant. The wear problem could be alleviated by using low friction material sleeves on the surfaces in contact with the ends of the stacks. Titanium is an appealing solution, but for the prototyping phase it is too expensive. Another choice is a hybrid composite reinforced with S-2 Glass[®] (produced by Owens Corning Corp.) and carbon fibers. Naturally, this part could be easily manufactured out of steel, and for applications where weight is not critical it is a reasonable choice. To avoid complications for this phase of actuator development, we have chosen to build the base out of bronze, even though this adds some undesirable compliance to the actuator.

This component has a geometrically simple construction and the only “special” requirements are related to the cylindrical surfaces that serve as pivoting surfaces for the stacks, and a good “snug” or even tight fit with tensioning element 6.

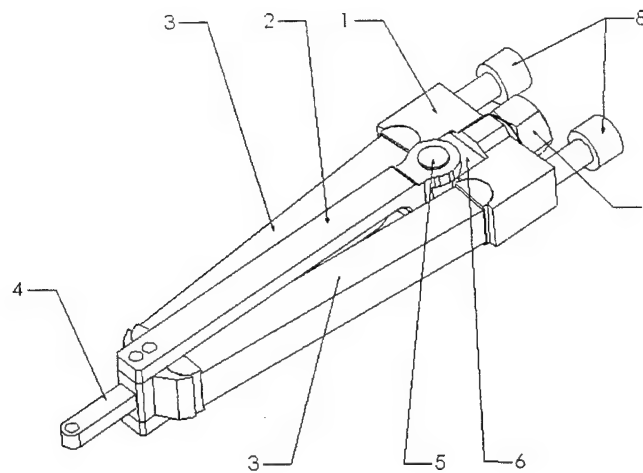


Figure 1. Actuator construction: 1-base, 2-lever, 3 – piezoelectric stacks, 4 – actuator tip, 5 – pivoting pin, 6 – pre-loading element, 7 – nut, 8 – mounting bolts.

Lever, 2, is the part that transfers the amplified motion to the structure that has to be actuated and it is also like a “backbone” of the actuator. The lever pivots about the axis of the pin 5 (Figure1) and transfers the useful work to the structure. It is also the part that transmits the “pre-load” to the stacks. The cross section is to be designed such that the lever will have a mass moment of inertia as small as possible with respect to axis of pivoting but have a high Young’s modulus (ideally infinite), in order to maximize the stiffness of the actuator. In order to obtain the geometric maximum stroke amplification, lever 2, should be perfectly rigid. Of course this is not practically possible, but choosing a material with high Young’s modulus, by proper design of the part and by pre-loading the mechanism, a high rigidity could be obtained. Because of dynamic considerations and mass efficiency, the mass of the lever should be as low as possible, so an optimization approach should be used to design this part.

Piezo-stacks, 3, are of a “classic” PZT multi-layer construction. After a market study on the manufacturers of piezoelectric materials, the choice was Noliac A/S, Denmark. The stacks are 80 mm long, have a square (10mm x 10mm) cross sectional area and are made of 39 layers of Pz27.

This is a high performance piezoelectric material, operating at relatively low voltage, and generating large displacements (0.175% at maximum positive voltage). The maximum operating voltage is $-50/+300\text{V}$. Displacement at V_{\max} is $-23/+140\text{ }\mu\text{m}$. The cross sectional area of the stacks is to be calculated as a function of the load. In section 2.2, the relationships between various constructive parameters of the actuator, load, and stroke are analyzed. As a general rule, in order to avoid buckling of piezo-stacks, their length is

recommended to be less than ten times the characteristic dimension of the cross-section (diameter in case of circular cross-section or the shorter side length in case of rectangular cross-section). The special feature of the construction is the end-cap, which has to be such that it will hold the piezo-stack and will make the mechanical connection between the stacks and the other elements (base and lever), possible.

Pivoting pin 5, tensioning element 6 and nut 7, form a sort of sub-assembly. Lever 2, rotates about the axis of pin 5. This sub-assembly also serves for pre-loading the mechanism. By simply tightening or loosening nut 7, a certain pre-loading force is created, such that the actuator will operate along the “impedance matched load characteristic”. The prescribed pre-loading force can be easily applied by using a torque-wrench or a regular wrench.

All the parts were machined in the Engineering Department Instrument Shop with conventional tooling. There is no need for very high precision machining.

2.2 Actuator Operation

The useful work is produced by displacement of the tip of the actuator as lever 2 pivots about the axis of pin 5. Oscillation of 2, about 5 is produced by making one stack expand and the other contract at the same time. The stroke amplification is obtained due to the geometry of the actuator, presented in section 2.3. Because the two stacks work complimentary (one expands, while the other contracts), there is a need to apply a bias

voltage such that the negative AC voltage peak will not go below -50 V. The voltage/displacement characteristic of the material is linear, such that the signals on the two stacks have to be in opposition of phase and symmetric with respect to the bias voltage. The actuator operates at full potential when the bias voltage is $+125$ V, and AC signal is $+175/-175$ V.

2.3 Actuator Geometry

Due to the fact that piezoelectric materials exhibit very small displacements, but are capable of withstanding high forces, an actuator that uses such materials as motors is required to amplify the active material motion. The present actuator is based on a simple idea of leveraging the stroke geometrically.

In Figure 2, the geometrical scheme of the actuator is presented.

Notations:

B – horizontal offset distance of the pivoting point of the stack, at the base of the actuator;

L_b – distance between the pivoting point of the lever and the pivoting point of the stack, at the base of the actuator;

e – eccentricity, which is the vertical offset distance between the pivoting point of the lever and the stack pivoting point at the base of the actuator;

b – horizontal offset of the pivoting point of the stack at the tip of the actuator;

R - distance between the pivoting point of the lever and the point of actuation;
 t - vertical offset distance between the pivoting point of the stack (at the tip) and the point of actuation;
 T - point of actuation (where the load is to be connected)
 s - stroke;
 L - distance between the pivoting point of the lever and the "line that connects the pivoting points of the stacks at the "tip" of the actuator;
 L_s - length of the stack (actual length of the piezostack);
 ε - linear strain of the stack;
 ξ - total elongation of the stack;
 L_{sp} - distance between the pivoting points of the stack (characteristic of the stack);
 L_{st} - theoretical length of the stack (between base pivoting point and theoretical point of intersection of the axis of the stack with the axis of the lever);
 L_{set} - theoretical length of the stack after expansion (due to the applied voltage);
 L_{set} - theoretical length of the stack after contraction (due to the applied voltage);
 L_t - theoretical length of the lever (distance between the pivoting point of the lever and the intersection of the lever axis with the axis of the stack);
 ψ - angle between the axis of the stack and axis of the lever at "zero" voltage;
 $\psi_{e,c}$ - angle between the axis of the stack and axis of the lever at a certain applied voltage (e stands for elongated and c stands for compressed);
 ϕ - actuation angle (angle between the axis of the lever at "zero" and the final position of the axis);
 k_s - amplification ratio (ratio between the stroke - s and the elongation of the stack - ξ)

The geometrical characteristic of interest is the stroke, s . The “exact” stroke is given by:

$$s = R \left[\arccos \frac{B^2 + (L - L_{sp})^2 + \left(L + \frac{b}{B-b} L_{sp} \right)^2 - \left(\frac{B}{B-b} L_{sp} + \xi \right)^2}{2\sqrt{B^2 + (L - L_{sp})^2} \left(L + \frac{b}{B-b} L_{sp} \right)} + \right. \\ \left. \arccos \frac{B^2 + (L - L_{sp})^2 + \left(L + \frac{b}{B-b} L_{sp} \right)^2 - \left(\frac{B}{B-b} L_{sp} \right)^2}{2\sqrt{B^2 + (L - L_{sp})^2} \left(L + \frac{b}{B-b} L_{sp} \right)} \right] \quad (1)$$

A linear expression for s is:

$$s = k_s \xi = k_s \epsilon L_s \quad (2)$$

where:

$$k_s = R \left(\frac{\frac{BL_{sp}}{B-b}}{\sqrt{B^2 + (L - L_{sp})^2} \left(L + \frac{b}{B-b} L_{sp} \right)} \right) \quad (3)$$

Amplification ratio, k_s is obtained by taking the derivative of the stroke with respect to the elongation. Equation (3) is obtained by neglecting small terms (higher order).

From (3), it can be seen that k_s is a function only of the actuator characteristics, B , b , L , L_{sp} .

The position angle Φ , between the axis of the lever in the “neutral” or “non-displaced” position and the axis of the lever in “displaced” position is to be determined using the following equations:

$$\Phi = k_{\Phi} \xi = k_{\Phi} \varepsilon L_s \quad (4)$$

where k_{Φ} is:

$$k_{\Phi} = \frac{\frac{BL_{sp}}{B-b}}{\sqrt{B^2 + (L - L_{sp})^2} \left(L + \frac{b}{B-b} L_{sp} \right)} \quad (5)$$

Similarly, one obtain linear equations for the angle between the “elongated” stack and the “neutral” axis, and the “shortened” stack and “neutral” axis respectively. Angle Θ is calculated as:

$$\sin \Theta \cong \Theta = \frac{B-b}{L_{sp}} \quad (6)$$

Then:

$$\Theta_e = \Theta + k_{\Phi} \xi \quad (7)$$

$$\Theta_c = \Theta - k_{\Phi} \xi \quad (8)$$

A comparative graph is presented in Figure 3. There is a nearly perfect match between the “exact” and “linearized” results. The dimensions are as follows: $B=12\text{mm}$, $b=5.5\text{mm}$, $L_{sp}=80\text{mm}$, $L_p=80\text{mm}$.

For this particular construction, the stroke amplification is 9.1667. Given the piezoelectric stacks peak-to-peak free displacement ($163\mu\text{m}$ of the piezoelectric stacks), the maximum theoretical peak-to-peak stroke is 1.49mm .

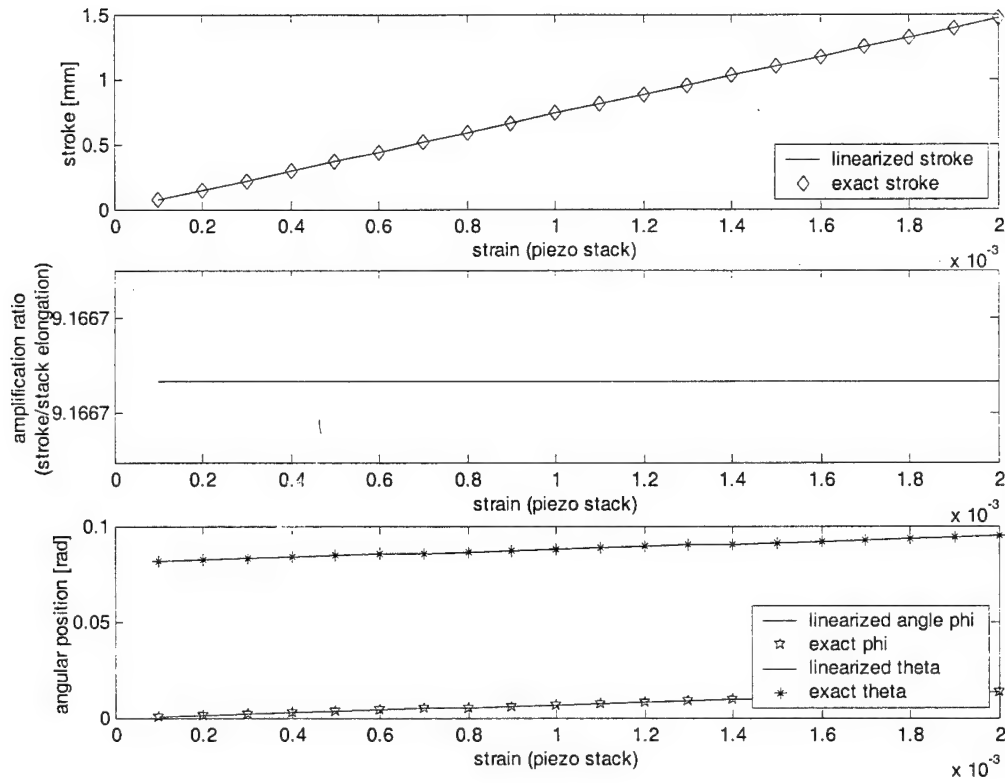


Figure 3. Comparison between the exact and linearized results for stroke, s , amplification ratio k_s and angles ϕ and θ

3. STATIC CHARACTERISTICS

The construction of the actuator is such that the piezostacks are theoretically subjected only to axial forces. The axial force produced by the piezostacks (d_{33} mode) is function of the applied voltage and the mechanical stiffness of the stacks (Giurgiutiu and Craig, 1997; Prechtel and Hall, 1999) and writes as:

$$F = \frac{E_s A_s}{L_s} d_{33} V - \frac{E_s A_s}{L_s} \xi \quad (9)$$

In (9), E_s is the Young's modulus of the piezostack, A_s is the cross section area of the piezo-stack, d_{33} is the piezoelectric constant, in m/V or C/N and V is the applied voltage and ξ is the elongation of the stack.

For the output force at the tip of the actuator, a similar formula can be written:

$$F_{out} = F_b - K_{out} s \quad (10)$$

and

$$F_b = K_{out} s_f \quad (11)$$

F_b is the “blocked” force and s_f is the free displacement at the tip, calculated with (12):

$$s_f = k_s \xi_f = k_s d_{33} V \quad (12)$$

where ξ_f is the free displacement of the piezostack.

A linear model of the actuator (force balance at the tip, considering the lever perfectly rigid), leads to the following formula for the output stiffness:

$$K_{out} = \frac{E_s A_s}{L_s} \frac{\Theta}{k_s} \quad (13)$$

From (9) and (10), is obvious that if there is little displacement, the output force is large, and if the stroke is large, the output force decreases to zero as the stroke tends to s_f .

4. ACTUATOR EFFICIENCY

Speaking about actuator efficiency, there are two issues to be addressed: mechanical efficiency and mass efficiency (especially important in applications where mass is critical, like HAR wings). Giurgiutiu and Craig (1997) and Prechtel and Hall (1999), have outlined, that the maximum mechanical energy it can be extracted from a piezoelectric actuator under optimum operating conditions (impedance match) is 25% of that of the active material.

Mechanical efficiency is defined as the ratio between mechanical energy output of the actuator and the electrical energy input, (14).

$$\eta_{mech} = \frac{E_{out}}{E_{in}} \quad (14)$$

The mechanical energy output is calculated with (15),

$$E_{out} = \frac{1}{2} K_{out} s_f^2 \quad (15)$$

where K_{out} is calculated with (13) and s_f is calculated with (12).

$$E_{in} = \frac{1}{2} E_s V_s \varepsilon^2 \quad (16)$$

where E_s is the Young's modulus of the stack, V_s is the volume of the stack and ε is the induced strain of the piezostack.

For mechanical efficiency, by introducing the geometrical relationships between different characteristics of the actuator, one obtains:

$$\eta_{mech} = \Theta k_s \quad (17)$$

Using the piezoelectric stacks characteristics, given in section 2.1, and the calculated mass of the actuator (prototype) one obtains the values:

- $\eta_{mech} = 74.25\%$

- $\eta_{mass} = 15.70\%$

The somewhat small value for the mass efficiency is due to the fact that “low performance” materials (steel and bronze) were used for base and lever. An actuator with the base and lever made out of composites or low density/high strength alloys (like titanium) would have a better mass efficiency – one should use a design optimization approach for maximizing the mass efficiency for a given material).

5. EXPERIMENTAL RESULTS

The experiments were performed using SigLab software, Krohn Hite wideband power amplifiers Model 7500 and, Brüel&Kjær accelerometer (Type 4374) and a Brüel&Kjær charge amplifier (Type 2635).

5.1 Static Characteristics

Experiments were carried out using low frequency signals (1.5 Hz). The parameter of interest is the tip deflection of the actuator. The displacement at the tip of the actuator was measured for voltages ranging from 0 to 240 V (peak to peak) for three cases: free (no load), 125 N and 93 N spring loads at the tip. Precision die springs were used for loading of the actuator. The spring constants were 13.3 N/mm and 18.9 N/mm respectively. There was a +75 V DC offset on both stacks.

The results are presented in Figure 4. For comparison, the theoretical curves are shown. The experimental results exhibit a slight non-linearity and a shift from the theoretical curves. These are a result of the hysteretic behavior of the piezoelectric materials and of the friction in the bearings (end caps of the stacks). Lubrication of the bearings or materials with lower friction coefficients might help reduce the shift, while non-linearity is an inherent property of the piezoceramics.

When the load was applied at the tip of the actuator, the displacement was zero for voltages below those required to reach the load level, in other words the blocked force at that particular voltage.

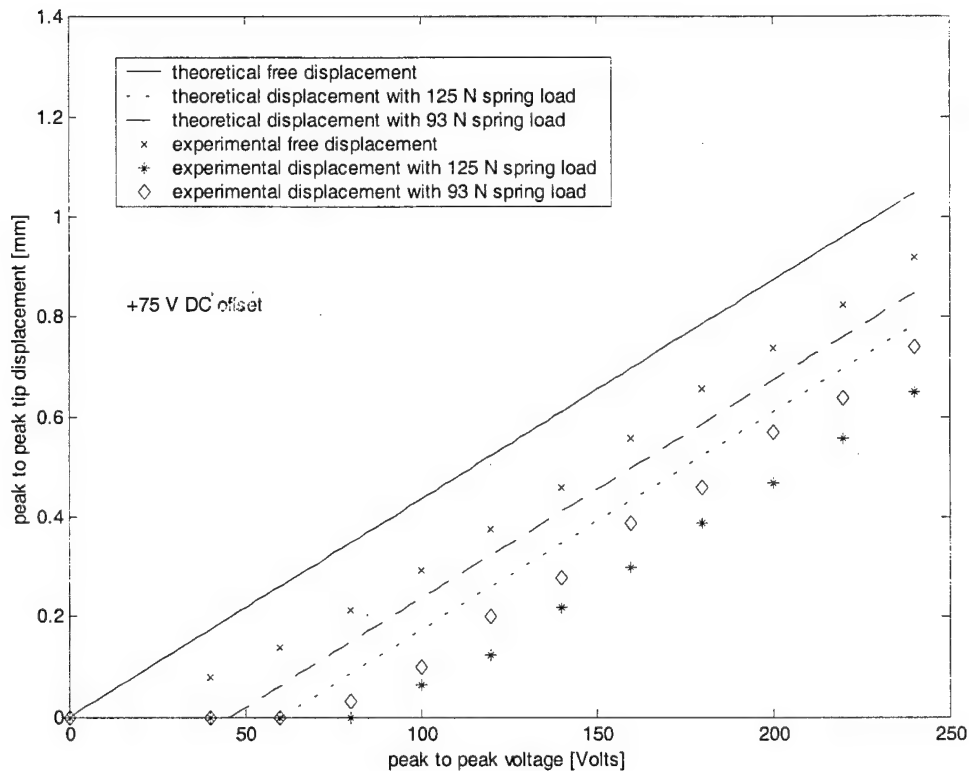


Figure 4. Peak to peak displacement at the tip of the actuator as a function of the applied voltage

5.2 Dynamic Response of V-Stack Actuator

When an actuator is to be integrated in linear control schemes of dynamic systems, that actuator it is supposed to be used at a frequency below to that of its first natural mode (sufficient bandwidth/control authority).

In Figure 5 is presented the frequency response of the actuator. The test was performed with no load at the tip of the actuator. The signal used for powering the stacks was white noise (2.0 V rms) over 1000 Hz bandwidth. At low frequencies (below 20 Hz) the power of the input signal was very low and that affected somewhat the shape of the transfer function plot. Neglecting this aspect, the response is “flat” up to about 350 – 400 Hz with small phase lag of the displacement with respect to the applied voltage.

The first natural frequency of the actuator is at 575 Hz, which gives confidence in the control authority of the actuator.

6. CONCLUSIONS

The early development of a new piezoelectric actuator was presented. The tests performed in the Adaptive Systems and Structures Laboratory at Duke University, indicated that V-Stack Actuator meets the requirements for actuating the trailing edge flap of a HAR wing.

Given the special construction of the actuator (built-in preloading mechanism, the symmetry, compactness, simplicity) the integration into a wing (or any other structure), requires minimal modifications of the internal structure of the wing.

The results provided by a dynamic model developed for early design purposes do not match with the experimental data, but the shape of the frequency response curve is similar. Because of that, the immediate objective is to develop a dynamic model, which will accurately describe the behavior of the actuator.

The prototype will be incorporated into a typical section and is going to be tested in order to fully characterize the actuator. In the meantime we are looking for other possible applications of the V-Stack Actuator.

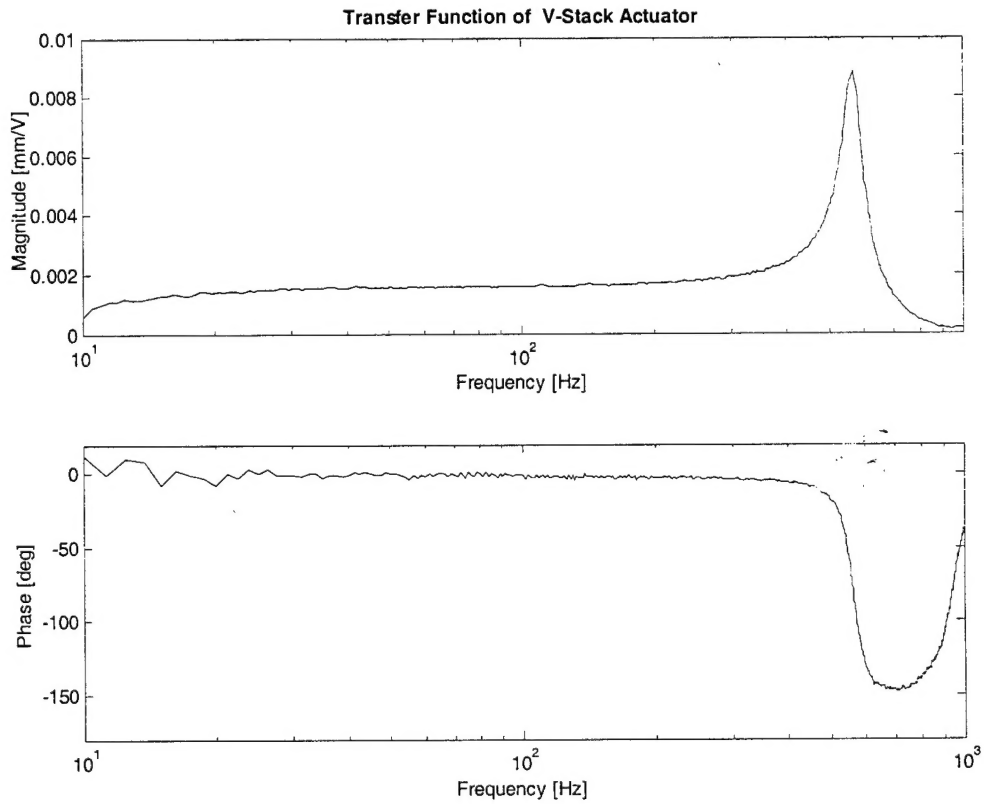


Figure 5. Transfer Function of V-Stack Actuator Prototype

ACKNOWLEDGEMENTS

This work was supported by DARPA through AFSOR Grant F49620-99-1-00253, *Aeroelastic Leveraging and Control Through Adaptive Structures*, under the direction of Dr. Ephraim Garcia and Dr. Dan Segalman. We would also like to thank Dr. Earl Dowell and Dr. Deman Tang, for the data we have used in setting the requirements for the actuator. Thanks to senior machinist John Goodfellow for his effort and commitment in machining the parts. Thanks to our colleagues in the Adaptive Systems and Structures Laboratory: Dr. Mayuresh Patil and graduate students Robert Richard, Jonathan Kemp, Min Moon, Mark McEver and Matt Kozlowsky, for useful discussions and assistance.

References:

- Chandra, R. and Chopra, I., 1998. "Actuation of Trailing Edge Flap in Wing Model Using Piezostack Device, *Journal of Intelligent Materials Systems and Structures*, Vol. 9, October, pp. 847-853.
- Clark, R. L., Saunders, W. R. and Gibbs, G. P., 1998. *Adaptive Structures, Dynamics and Control*, John Wiley & Sons Inc., New York, 1998.

- Dogan, A., 2001. "Solid-State Ceramic Actuator Designs", *AIAA Journal*, Vol. 39, No.7, July, pp. 1354-1362.
- Giurgiutiu, V. and Rogers, C. A., 1997. "Power and Energy Characteristics of Solid-State Induced-Strain Actuators for Static and Dynamic Actuations", *Journal of Intelligent Materials Systems and Structures*, Vol. 8, September, pp. 738-750.
- Hal, S.R., Spangler, R.L., 1993, "Piezoelectric Helicopter Blade Flap Actuator". US Patent # 5,224,826, issued July 6, 1993.
- Koratkar, N. A. and Chopra, I., 2000. "Analysis and Testing of Mach-Scaled Rotor with Trailing-Edge Flaps", *AIAA Journal*, Vol. 38, No. 7, July, pp. 1113-1124.
- Lyung, L., 1999. System Identification, Theory for the User, Second Edition, Prentice Hall, Upper Saddle River, NJ, 1999.
- Meirovitch L., 1997. Principles and Techniques of Vibrations, Prentice Hall, Upper Saddle River, NJ, 1997.
- Physik Instrumente, 1995. Products for Micropositioning, Catalog US-Edition, Auburn, MA, 1995.
- Prechtel, E. F. and Hall, S. R., 1998. "An X-Frame actuator servo-flap actuation system for rotor control", *Proceedings, SPIE Smart Structures and Integrated Systems*, San Diego, CA, Mar 1998.
- Prechtel, E. F. and Hall, S. R., 1999. "Design of a high efficiency, large stroke, electromechanical actuator", *Smart Materials and Structures*, 8(1999), pp. 13-30.
- Tang, D. and Dowell, E. H., 2001. "Experimental and Theoretical Study on Flutter and Limit Cycle Oscillations of High Aspect Ratio Wings", *AIAA Journal*, 2001.
- Thomson, W. T., 1972. Theory of Vibration with Applications, Prentice Hall, Englewood Cliffs, New Jersey, 1972.